UC San Diego
UC San Diego Electronic Theses and Dissertations

Title

Advancing in situ observations of physical and biological processes with underwater imaging systems

Permalink

Author

Lertvilai, Pichaya

Publication Date

2021

Peer reviewed|Thesis/dissertation

UNIVERSITY OF CALIFORNIA SAN DIEGO

Advancing in situ observations of physical and biological processes with underwater imaging systems

A dissertation submitted in partial satisfaction of the requirements for the degree Doctor of Philosophy

in

Oceanography

by

Pichaya Lertvilai

Committee in Charge:

      Jules S. Jaffe, Chair
      Peter J.S. Franks
      Dariusz Stramski
      Mohan M. Trivedi

2022

The Dissertation of Pichaya Lertvilai is approved, and it is acceptable in quality and form for publication on microfilm and electronically.

University of California San Diego

2022

iii

DEDICATION

I dedicate this dissertation to my parents, Chantana Panyadilok and Pisuth Lertvilai, for their

unconditional love and spiritual support throughout my life. My success would not have been

possible without them.

EPIGRAPH

"Born too late to explore earth, born too early to explore space,

but just in time to explore the ocean."

— anonymous

TABLE OF CONTENTS

LIST OF FIGURES

LIST OF TABLES

ACKNOWLEDGEMENTS

I would like to thank my PhD advisor, Dr. Jules Jaffe for introducing me to the world of underwater imaging and giving me an opportunity to do research in his lab. I am grateful for support, guidance, knowledge, encouragement, inspiration and motivation throughout my PhD journey. I am sincerely grateful for his time, patience and contributions to my development as a scientist.

I would also like to thank my thesis committee members, Profs. Peter Franks, Dariusz Stramski, Farooq Azam and Mohan Trivedi, for the support, valuable discussions, and insightful comments to my research. Additionally, I am grateful to Prof Stuart Humphries. Dr. Oscar Guadayol roig, Dr. Ed Parnell, Dr. Lanna Cheng and Dr. Christian Briseno-Avena for their productive collaborations and their valuable advice with the projects.

I also thank current and former engineering staff, Paul Roberts and Devin Ratelle, for their engineering supports, and thank the dive program staff, Christian McDonald, Richard Walsh and Phil Zerosfki, and my dive buddy, Mohammad Sedarat, for their supports in the field operations. I am also grateful to all members of Jaffe Lab and Franks Lab for their valuable comments and for allowing me to bounce ideas that help improve my work.

Chapter 1, in full, is a reprint of the material as it appears in *Journal of Atmospheric and Oceanic Technology*. Lertvilai, Pichaya; Roberts, Paul; Jaffe, Jules, 20121 The dissertation author was the primary investigator and author of this paper.

Chapter 2, in full, is a reprint of the material as it appears in *Methods in Ecology and Evolution*. Lertvilai, Pichaya, 2020.

Chapter 3, in part, is currently under review in *Methods in Ecology and Evolution*. Lertvilai, Pichaya; Jaffe, Jules. The dissertation author was the primary investigator and author of this paper.

Chapter 4, in part, is currently being prepared for submission for publication of the material. Lertvilai, Pichaya; Jaffe, Jules. The dissertation author was the primary investigator and author of this paper.

VITA

2016   B.Sc., Engineering
Harvey Mudd College

2021   M.Sc., Oceanography
Scripps Institution of Oceanography
University of California San Diego

2022   Ph.D., Oceanography
Scripps Institution of Oceanography
University of California San Diego

PUBLICATIONS

Lertvilai, P and Jaffe, J.S. Label-free underwater single-cell and fluorescence imaging of aquatic microorganisms with laser-pulsed darkfield microscopy. *In prep.*

Lertvilai, P and Jaffe, J.S. In situ size and motility measurement of aquatic invertebrates with an underwater stereoscopic camera system using tilted lenses. *Methods in Ecology and Evolution*, *under review*.

Lertvilai, P., Roberts, P.L. and Jaffe, J.S., 2021. In Situ Underwater Average Flow Velocity Estimation Using a Low-Cost Video Velocimeter. *Journal of Atmospheric and Oceanic Technology*, 38(6), pp.1143-1156.

Lertvilai, P., 2020. The in situ plankton assemblage eXplorer (IPAX): an inexpensive underwater imaging system for zooplankton study. *Methods in Ecology and Evolution*, 11(9), pp.1042-1048.

ABSTRACT OF THE DISSERTATION

Advancing in situ observations of physical and biological processes with underwater imaging
systems

by

Pichaya Lertvilai

Doctor of Philosophy in Oceanography

University of California San Diego, 2022

Jules S. Jaffe, Chair

The ocean is a complex and dynamic environment with physical and biological processes
that span across all scales. Though scientific studies in laboratory setting can provide insights
into these complicated processes, it is difficult to fully replicate the natural environment in the
lab. As a result, studies of processes in the natural environment, or *in situ* studies, can help
bridge information from laboratory experiments to their actual implication in the nature. Recent
technological advances have enabled the ocean to become more accessible for scientific research
and exploration. Particularly, breakthroughs in imaging technology have enabled new imaging
techniques to be accessible at smaller form factors and lower costs, such that they are suitable for
oceanic deployments.

Here I developed four underwater imaging systems and demonstrated their capability as tools for studying both physical and biological processes in the ocean. The first system is a particle imaging system that can be used to resolve average flow velocity by applying a modified particle image velocimetry algorithm. The formulated algorithm allows the system to be constructed with low-cost components that permits the whole system to be more affordable. The second system is an underwater microscope for zooplankton study that is based on open-sourced hardware and software. The system was used to investigate the emergence pattern and the spectral response of demersal zooplankton in the Kaneohe Bay, Hawaii. The third system is a stereoscopic imaging system that implements a tilted lens approach to increase the shared field of view between the two cameras. The method allows the stereoscopic system to perform *in situ* trait measurements of aquatic invertebrates. The system was deployed in Kendall-Frost saltmarsh, San Diego, to determine the relationship between the swimming speed and the body length of aquatic insects, *Trichocorixa californica*. Finally, the fourth system is an underwater microscope that has sufficient resolution and contrast perform label-free imaging of marine microorganisms. The instrument utilizes a laser-pulsed darkfield microscopy technique to image individual cells of marine microorganisms and to detect fluorescence signals from natural pigments. The system was used in an *in situ* observational study on biofilm formation on a man-made substrate.

Chapter 1: In situ underwater average flow velocity estimation using a low-cost video velocimeter

In Situ Underwater Average Flow Velocity Estimation Using a Low-Cost Video Velocimeter

PICHAYA LERTVILAI,[a] PAUL L.D. ROBERTS,[b] AND JULES S. JAFFE[a]

[a] *Scripps Institution of Oceanography, University of California, San Diego, La Jolla, California*
[b] *Monterey Bay Aquarium Research Institute, Moss Landing, California*

ABSTRACT: The development of a low-cost Video Velocimeter (VIV) to estimate underwater bulk flow velocity is described. The instrument utilizes a simplified particle image correlation technique to reconstruct an average flow velocity vector from video recordings of ambient particles. The VIV uses a single camera with a set of mirrors that splits the view into two stereoscopic views, allowing estimation of the flow velocity vector. The VIV was validated in a controlled flume using ambient seawater, and subsequently field tested together with an acoustic Doppler velocimeter with both mounted close to the coastal seafloor. When used in nonturbulent flow, the instrument can estimate mean flow velocity parallel to the front face of the instrument with root-mean-squared errors of the main flow within 10% of the $\pm 20\,\mathrm{cm\,s}^{-1}$ measurement range when compared to an acoustic Doppler velocimeter (ADV). The predominant feature of the VIV is that it is a cost-effective method to estimate flow velocity in complex benthic habitats where velocity parallel to the sea floor is of interest.

KEYWORDS: In situ oceanic observations; Instrumentation/sensors; Measurements

1. Introduction

Since the beginnings of oceanography, the utility of instruments to measure ocean currents has been an important aspect of studying the ocean. The ocean currents determine the fate of both inanimate particles and many living organisms in marine environments. Nutrients from rivers, groundwater and atmosphere are distributed and transported offshore by coastal currents (Jickells 1998) and can eventually be carried back to the coasts by upwelling currents (Martin and Richards 2001). The survival of many organisms, especially suspension feeders, depend on ocean currents to provide nutrients (Hill et al. 1992) and to support larval transport to suitable settlement areas (Pineda et al. 2011). Even small-scale turbulence can have profound effects on marine organisms by determining predator–prey contact rates (Rothschild and Osborn 1988) and by forming nutrient patches for foraging (Davis et al. 1991). As a result, the advancement of instruments to measure ocean currents has been an active development area throughout the history of oceanography.

The earliest marine current velocity sensors were based on the rotation of a propeller-like device around a shaft, such as the Ekman current meter (Ekman 1932), the Roberts current meter (Knauss 1959), and the Savonius current meter (Weller and Davis 1980). Electromagnetic current meters (ECMs),

which utilize magnetic-induced electrical current by ions in seawater passing through a known magnetic field (Jones 1980), became popular in the 1950s and 1960s, but their popularity has been declining due to intrusive nature of the measurement (MacVicar et al. 2007). Drag force current meters are relatively inexpensive current sensors that measure drag force on known objects to calculate current velocity. These meters are widely used in ecological studies where instrument cost is the driving factor (e.g., Johansen 2014; Mach et al. 2011; Madin and Connolly 2006). Currently, acoustic current meters are the most popular way to measure currents where precise scientific data are desired. These current sensors measure either the Doppler shift or the travel time of transmitted acoustic signals that are backscattered from ambient particles, which allows the instruments to resolve flow velocity in two or three dimensions. There are two main popular variations of acoustic current meters, the acoustic Doppler current profiler (ADCP), which resolves a velocity profile of the water column, and the acoustic Doppler velocimeter (ADV), which measure a point velocity. Although these acoustic current sensors are widely used and can provide accurate velocity measurement (Lohrmann et al. 1994), these systems are often relatively expensive to use in high risk environments or swarm operations (Fuentes-Perez et al. 2018). They also have a large form factor and high energy consumption, which are not suitable for small platforms (Jaffe et al. 2017) or long-term deployment (Rudnick et al. 2004). As a result, development of new underwater current meters is still an active area of research.

A standard technology in velocity measurement uses optical systems to track movement of particles to measure currents, which are known as particle image velocimetry (PIV) and particle tracking velocimetry (PTV) (Prasad 2007; Raffel et al. 1989). In the case of aquatic systems, there are several systems that can perform in situ PIV or PTV measurements (e.g., Katija and Dabiri 2008; Liao et al. 2009; Tritico et al. 2007;

FIG. 1. Schematic of optics of the VIV. (a) The mirror setting that splits the view of the camera into two separate stereo views. (b) The position of the illumination LED with respect to the camera and the mirror setup. The secondary optics focuses the beam with full width at half maximum intensity of 14.3°. The mirror dimensions are from manufacturer's specifications, and the dimensions of the field of view are from calibration. The schematic is not drawn to scale.

Smith 2008). An in situ system for measuring turbulence using the PIV method has also been fabricated and tested (Steinbuck et al. 2010). There also are attempts to lower the complexity of PIV measurements by using LED illumination instead of a laser sheet, which resulted in more compact and more affordable PIV systems (Chételat et al. 2001; Hagsäter et al. 2008; Estevadeordal and Goss 2005). However, to date, these systems are not designed to be deployable in field environments.

Despite the utility of the in situ systems to resolve complex flow fields in multiple dimensions, there are many applications that only need a point measurement of velocity, similar to an ADV, and do not need the complexity of robust PIV or PTV techniques. Additionally, the emerging maker practice has enabled many electrical components and software packages that were traditionally costly or difficult to obtain, such as controllable cameras and single-board computers, to become widely accessible at low cost through collaborations between developers with open-source hardware and software (Tanenbaum et al. 2013). As a result, in this article, we explore the advantage of the maker practice to develop a less expensive and more compact system for point measurement of flow velocity in situ.

To achieve our goal, we constructed and calibrated a stereoscopic optical current meter based on a low-cost computer and camera system. A simplified particle image cross-correlation algorithm was then implemented to facilitate

computation on the low-cost computer. The instrument was calibrated in a flume with controllable flow rate and then deployed in the field to capture in situ particle movements, which were then used to reconstruct the bulk flow velocity vector. The measurement was validated with an ADV, a standard velocity measurement technique. Here, we demonstrate that our system, which we refer to as the Video Velocimeter (VIV), is capable of estimating bulk flow velocity in situ with good agreement with an ADV using only ambient natural particles without additional particle seeding.

2. Materials and methods

a. Instrument description

The VIV utilizes a Raspberry Pi Camera V2 [Sony IMX219 sensor as detailed in Pagnutti et al. (2017)] with the stock lens as the imager and a Raspberry Pi single-board computer (Raspberry Pi Foundation, United Kingdom) as the main processing unit. To keep the hardware simple and to avoid problems of synchronization, a split field of view using one imaging sensor was employed as described in Yu and Pan (2016). The system consisted of a set of two planar mirrors and one right angle prism mirror to split the field of view into two views (Fig. 1). The mirrors and the prism were rated for 4–6λ flatness with protected aluminum coating (Edmunds Optics, United States). The size of the mirrors and the configuration (a, b, c,
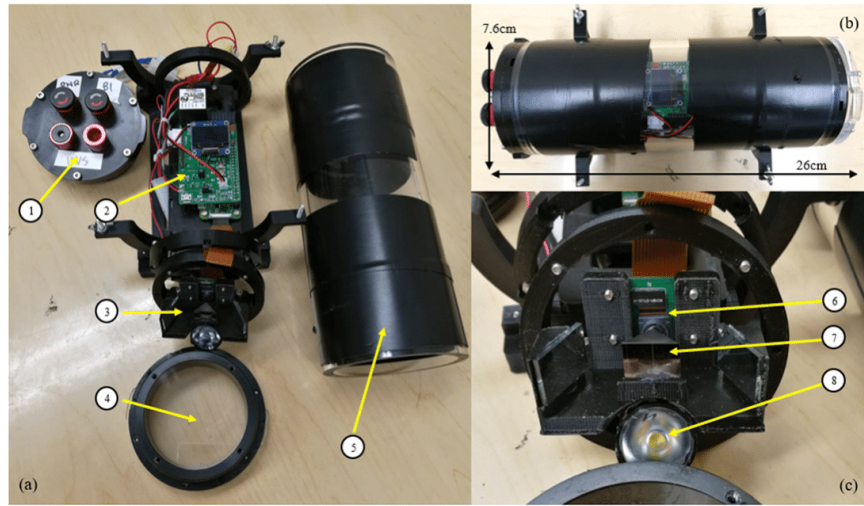
FIG. 2. The Video Velocimeter. (a) Overview of the entire instrument: 1) aluminum back plate with switches, pressure sensor and vent hole, 2) control board, 3) camera and optics, 4) acrylic view port, and 5) acrylic tube housing. (b) Assembled unit with dimensions. (c) Optical components: 6) Raspberry Pi camera, 7) mirror system, and 8) LED with lens.

and α) were chosen to maximize the overlapping of the field of view and the illumination while allowing the setup to fit inside a commercially available waterproof housing. This method allowed inverting for a bulk 3D flow vector from the set of linearly independent views. The setup also reduced the computational overhead needed to control multiple cameras, which was significant for a small single-board computer.

To further minimize the complexity and the cost of the system, an LED illumination is chosen as the light source instead of a typical laser sheet illumination. LEDs produce incoherent light that suppresses speckles while costing much less than laser diodes and requiring simpler driver circuits (Chételat and Kim 2002). Due to space limitation inside the housing, a single CREE XT-E white LED was used as the light source. The LED utilized a Carclo frosted narrow spot lens as a secondary optics and is driven by a LuxDrive 500mA BuckPuck DC LED driver (all illumination components were obtained from LEDsupply, United States).

For this ocean-going instrument, the Raspberry Pi Zero W model was chosen as the main computer because it was, at the time, the most power-efficient and the least expensive single-board computer model. However, it should be noted that any Raspberry Pi model, including model 3A+ and 4B, could be interchanged for this instrument. The models with more computational power had the tradeoffs of costing more and consuming more power. In addition to the main computer, a custom-made control board was designed and fabricated that regulated power, communicated with a pressure sensor, and provided feedback through an OLED display (Fig. 2). The system was powered by a 24 Wh lithium battery pack (Anker, Shenzhen, China), which allowed the instrument to run continuously for

approximately 8 h. The entire system was housed in an acrylic cylinder housing with an aluminum backplate and a flat acrylic viewport rated for 100 m depth (Bluerobotics, United States). The camera lens was adjusted so that the focal plane was 5 cm away from the front of the viewport. In 2019 dollars, the entire bill of materials for the instrument cost 480 U.S. dollars (Table 1).

It should be noted that the custom-made control board can be replaced with off-the-shelf boards that can perform power management for Raspberry Pi such as Sleepy Pi 2 (Spell Foundry, United Kingdom). Using off-the-shelf boards will help reduce lead time to fabricate the system. However, connections to other components, such as the LED driver and the environmental sensors, have to be manually wired and secured inside the housing. Caution should be exercised to make sure that connections are correct, and components are properly secured.

The VIV was programmed with Python code embedded on the Raspberry Pi using the default Raspberry Pi Camera

TABLE 1. Instrument cost breakdown materials. Note that the pressure sensor is not crucial for the function of the instrument as a velocity sensor but is included to obtain environmental information.

Items	Cost (U.S. dollars)
Housing	130
Pressure sensor	90
Optics	135
Camera	30
Computer	10
Control board	60
Battery	25
Total	480
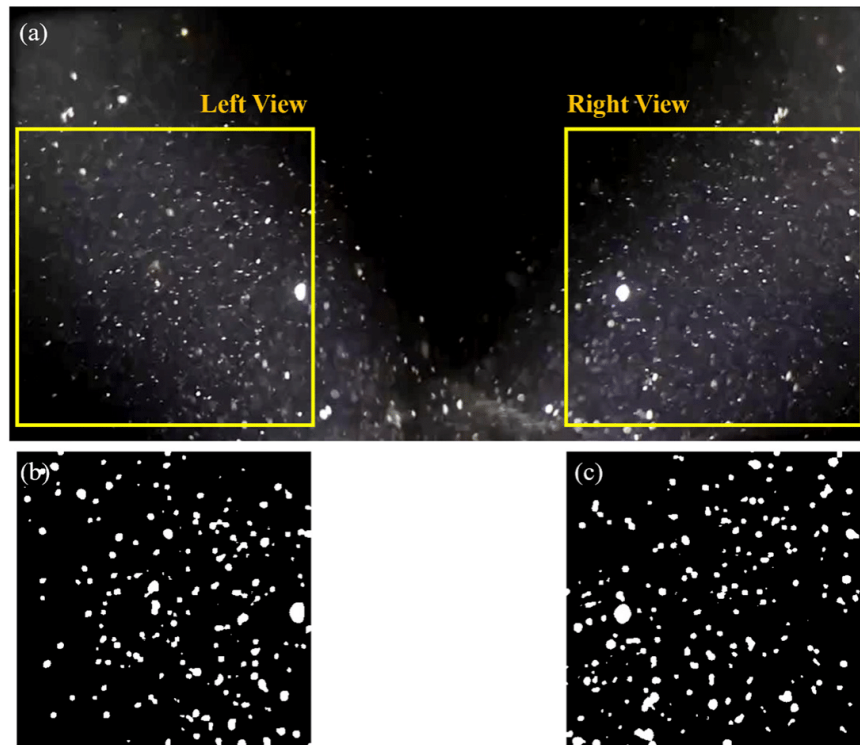
FIG. 3. An example image of ambient particles recorded by the VIV. (a) The full field of view of the camera, which is split into two linearly independent views. The yellow boxes indicate the regions that are extracted to perform velocity measurement. (b),(c) The images of particles used in velocity measurements of the simplified correlation method. The images are preprocessed with adaptive thresholding to enhance particles and to equalize their intensity within particles.

package provided by the Raspberry Pi Foundation. The camera software allowed the computer to adjust setting of the camera and also provided a flash synchronization feature. This feature enabled the LED to be hardware triggered by a control pin to synchronize the flash with the frame acquisition. This flash synchronization allowed the power consumption of the LED to be half of what it would be if the LED were constantly on.

This implementation, together with the volume illumination, allowed the entire setup to fit inside a small cylindrical housing of 7.6 cm diameter $\times$ 26 cm long. The trade-off was that the usable field of view (FOV) of each stereo view was reduced to half of the original camera FOV. Given the mirror setup, the usable FOV was also smaller than the sensor of the Raspberry Pi Camera V2, so each view was obtained by extracting a 400×400 pixel region, which was then used to estimate velocity (Fig. 3a).

b. Velocity reconstruction with simplified correlation

The LED illumination in the VIV resulted in volume illumination. In a typical microPIV system, the imaged particles are constrained by the narrow depth of field of the imaging systems (Bourdon et al. 2003; Olsen and Adrian 2000). However, the low-cost Raspberry Pi Camera provided a much broader depth of field, in the centimeter range, when the focal plane was set to 5 cm distance from the front of the viewport of the VIV. With only two views provided by the mirror setup and the low computing power of the Raspberry Pi computer, it was not feasible to accurately implement velocity field reconstruction. However, in this study, we only seek to compute the averaged velocity of all particles in the field of view in contrast to the detailed flow field. As a result, we will only implement a simplified correlation algorithm as formulated below.

First, even though the optical setup was designed such that the LED illuminates all particles in the overlapping FOV of the two views, the nonuniform illumination of the LED causes particles in the middle of the FOV to be brighter than those on the edges (Fig. 3a). To correct for this nonuniformity, raw images from the camera were preprocessed by Wellner's adaptive thresholding method (Wellner 1993) to create binary images of particles (Figs. 3b,c). This process allows all particles

that are brighter than the immediate surrounding background to be detected regardless of the absolute intensity of both background and particles. This process also detects particles in the overlapping FOV that are out of focus in each view and treat them the same as in-focus particles. With this processing step, the raw images become binary images such that all detected particles have the same uniform intensity and are approximately spherical.

With a large depth of field, the location of the peak of the correlation function is the weighted sum of the individual correlation functions at each range z from the imager (Bourdon et al. 2003):

$$C_v(x, y) = \alpha \sum_{z=z_{\min}}^{z_{\max}} c(x, y, z), \qquad (1)$$

where C_v is the overall correlation of the entire volume, $c(x, y, z)$ is the individual correlation at range z, α is a proportional constant, and $z_{\min}$ and $z_{\max}$ are the boundaries in range of the illuminated particle field. Typically, the volumetric correlation is accomplished by decomposing the image with regards to point spread function of seed particles with known size (Fouras et al. 2009). However, the VIV is intended to use natural particles, so the particle sizes cannot be known a priori.

Opportunistically, medium-scale oceanographic currents, such as internal waves and wind-driven waves, are often periodic and unidirectional in short periods of measurement time (Garwood et al. 2020; Johansen 2014). As a result, we can make simplifying assumptions that all particles in the illuminating volume are moving at the same velocity and are uniformly distributed in the volume. We further assume that particle size distribution is constant within the volume such that the average size of the imaged particles at every range is the same. Since we use binary images from the adaptive thresholding step, we can model these particles as approximately spherical with a projection of uniform circles of average radius r. The correlation peak of each depth would be located at $-f\Delta(X, Y)/z$, where f is the focal length of the imager and $\Delta(X, Y)$ is the particle displacement. These assumptions simplify the correlation function at each range to

$$c(x, y, z) = \alpha I_0(z) \left[1 - \frac{\left| (x, y) - \dfrac{f(\Delta X, \Delta Y)}{z} \right|}{r} \right], \qquad (2)$$

when $f(\Delta X, \Delta Y)/z - r \le (x, y) \le f(\Delta X, \Delta Y)/z + r$, and $c(x, y, z) = 0$ otherwise. The intensity of particles $I_0(z)$ is proportional to $1/z^2$ (Olsen and Adrian 2000). We can then substitute (2) into (1) and take the integral form of the Riemann sum as

$$C_v(x, y) = \beta \int_{z_{\min}}^{z_{\max}} \frac{1}{z^2} \left[1 - \frac{\left| (x, y) - \dfrac{f(\Delta X, \Delta Y)}{z} \right|}{r} \right] dz, \qquad (3)$$

where β is a constant. Solving the integral yields the peak location at

$$(\hat{x}, \hat{y}) = \frac{f}{\left(\dfrac{z_{\min}^3 + z_{\max}^3}{2} \right)^{1/3}} (\Delta X, \Delta Y) = M(\Delta X, \Delta Y). \qquad (4)$$

As a result, the measured displacement $(\hat{x}, \hat{y})$ from this simplifying correlation is proportional to the real displacement $(\Delta X, \Delta Y)$.

The proportional constant M only depends on the system parameters, so it can be obtained from laboratory calibration. However, even though this proportional constant does not depend on the particle size distribution, the size distribution still affects the shape of the cross correlation as seen in (3). In real implementation, there will be out-of-focus particles and occasional large particles that can cause the cross-correlation map to be noisy. This noise can reduce the accuracy of the peak detection in the algorithm, resulting in a less reliable velocity estimation. As a result, it is important to track the signal-to-noise ratio (SNR) of the correlation, which represents the measurement uncertainty in velocity estimation. In this study, we will use the primary peak ratio method (Xue et al. 2014),

$$\text{SNR} = \frac{P_1}{P_2}, \qquad (5)$$

where P_1 is the magnitude of the primary peak of the cross-correlation map, and P_2 is the magnitude of the second-tallest peak.

For the VIV, 400×400 pixels regions from both views of the camera are processed with adaptive thresholding method to generate binary images. These binary images are then cross correlated to compute the projected velocities from left view and right view, designated as $v_1 = (v_{x1}, v_{y1})$ and $v_2 = (v_{x2}, v_{y2})$, respectively. We implemented this cross correlation and peak detection using the OpenPIV Python package (Liberzon et al. 2016). Next, the apparent velocities from both views, V_1 and V_2, are obtained by multiplying the projected velocities with the multiplicative constant M obtained from laboratory calibration. Finally, both V_1 and V_2 are used to perform stereo reconstruction with the extrinsic parameters of the two views to compute the true velocity in three dimensions $V = V_x, V_y, V_z$ (Prasad 2000). This process is outlined in Fig. 4.

c. Laboratory validation

All optical calibrations of the instrument were done by submersing the instrument in a glass tank filled with filtered seawater and covered by black electrical tape on the inside to reduce reflection. The stereo view was calibrated with a checkerboard pattern with 6×4 inner corners using the photogrammetric algorithm (Zhang 1999) provided by OpenCV package. The angle between the two views was thereby calibrated to be $72°$ (θ in Fig. 1). The overlapping FOV of the two views are obtained by tracing the edge of the FOV of each stereo view on a paper; the dimensions are shown in Fig. 1.

To optimize the exposure and gain of the VIV an experiment was formulated that was designed to simulate a distribution of natural particles that would be encountered in the field, however, with known reflectors of known sizes. Here, we used polystyrene beads (Polyscience Inc., United States) of sizes 5–90μm diameter at concentrations of 8–150 beads per milliliter. The camera recorded video at 65 fps with 1280×720 resolution. The exposure and gain were optimized by using the particle detection algorithm based on using the adaptive thresholding method to discern whether the camera could

5

Left View

Raw images $\longrightarrow$ Binary images of particles $\longrightarrow$ $v_1 = (v_{x1}, v_{y1})$ $\longrightarrow$ $V_1 = M(v_{x1}, v_{y1})$

Adaptive thresholding   *Cross-correlation*   *M from calibration*   *Stereo –reconstruction using extrinsic parameters from calibration* $\longrightarrow$ $V = (V_x, V_y, V_z)$

Right View

Raw images $\longrightarrow$ Binary images of particles $\longrightarrow$ $v_2 = (v_{x2}, v_{y2})$ $\longrightarrow$ $V_2 = M(v_{x2}, v_{y2})$
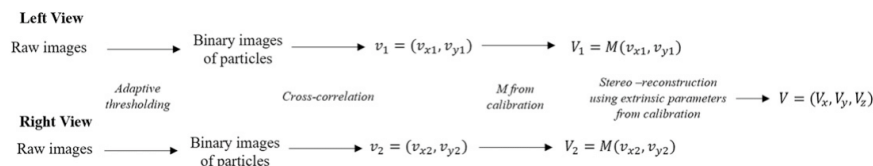
FIG. 4. Outline of the algorithm used in the VIV to reconstruct the 3D flow velocity from the images obtained from both views of the system. Here lowercase v indicates projected velocities, and uppercase V indicates real velocities.

detect the beads. Based on these experiments, it was concluded that a camera exposure of 2.5 ms with ISO320 was optimal. With this setting, the instrument could reliably detect polystyrene beads of 50 μm diameter or larger.

To test the system in uniform flow, an experimental Vogel flume (Lacoursière and Craig 1990) was constructed from clear acrylic sheets with the dimension 120 cm × 15 cm × 20 cm. The camera was attached to the outside wall such that the flow was parallel to the horizontal axis of the image, and it was positioned 60 cm away from the flume inlet and 8 cm above the bottom. The flume was filled with unfiltered natural seawater collected from the end of Scripps Pier, La Jolla, California.

Furthermore, in order to compare the method with a more traditional sensor as well as getting a correct estimate of velocity, a 10 MHz Sontek ADV was used concurrently to measure the 3D flow speed. The sampling volume of the ADV was located 8 cm above the bottom and as close to the imaging volume as possible without obstructing the LED illumination or disturbing the nature of the unidirectional flow. Flow speed inside the flume was controlled by a recirculating pump and was varied from 5 cm s^{-1} to a limit of 30 cm s^{-1}. At each flow speed, the ADV was used to measure the velocity for 60 s, and the average speed over this period was used to compute the displacement in the object plane ΔX of the particles by multiplying the speed by the time interval between consecutive

frames captured by the VIV. The VIV took a sequence of 30 images, and the simplified correlation method was used to reconstruct velocity. The ensemble average over the 30 frames was then calculated to validate the linearity in (4) in both the uniform flow and more turbulent conditions. The two-component velocities from each view of the VIV were then used to triangulate the three-dimensional flow. Results were then compared to the ADV measurements.

d. Field experiment

For field measurements, the VIV was mounted on a speed rail rig with its cylindrical axis parallel to the seafloor. An Argonaut ADV and an FT2ADV probe (Sontek, United States) were also mounted on the same rig (Fig. 5). However, only the data from the FT2ADV were used in this comparative experiment. The systems were configured so that the sampling volume of the ADV was inside the sampling volume of the VIV (Fig. 5b). The FT2ADV sampling frequency was set to 2 Hz. The rig was deployed by divers approximately 75 m west of Scripps Pier, La Jolla, at 13 m depth with the sampling volume located approximately 1 m above the seafloor. The instruments were positioned such that V_x measures alongshore velocity, V_y vertical velocity and V_z across shore velocity (Fig. 5b). The instruments were set to continuously collect data after positioning.
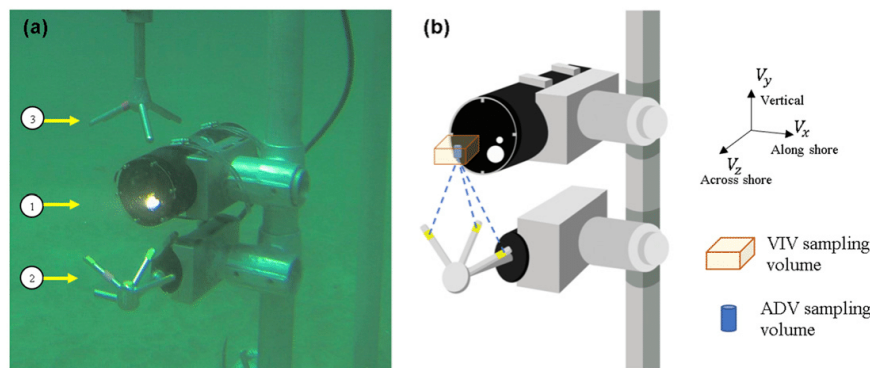
FIG. 5. (a) Field deployment of 1) the VIV with 2) an Argonaut ADV and 3) an FT2ADV. The site is 75 m west of Scripps Pier, La Jolla, at approximately 13 m depth. The VIV is positioned 1 m above the seafloor. (b) Schematic of the deployment configuration showing the sampling volume of the ADV inside the sampling volume of the VIV and the flow direction with respect to the shore.
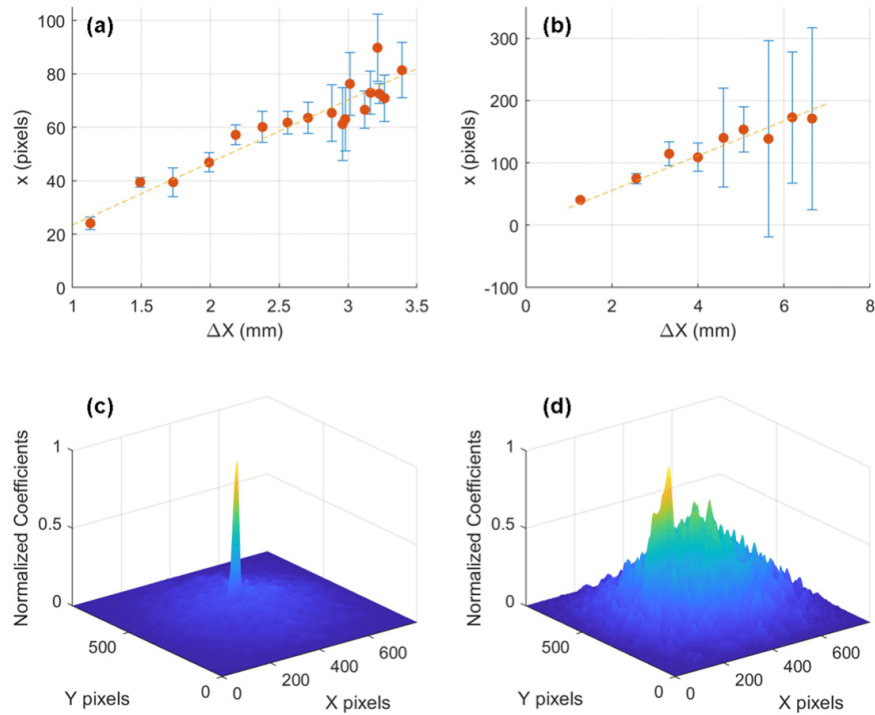
FIG. 6. Laboratory validation of linearity between the averaged displacement measured by the ADV ΔX and the averaged projected displacement X evaluated by the simplified correlation method (a) in slow unidirectional flow conditions and (b) in faster and more turbulent flow. (c) The cross-correlation map in a slow flow condition at $\Delta X = 1.5$ mm shows a very distinct and narrow peak. (d) The cross-correlation map in more turbulent condition at $\Delta X = 6.5$ mm shows a noisy map with less distinct peak.

The video record from the VIV was analyzed on each of the two fields of view of the camera system to obtain an estimate of the velocities in the camera coordinate system. The pair of vector velocity values, in the coordinate of the camera fields of view, were then used to estimate a velocity vector. Next, the result of nine velocity values that were obtained from the 10 pairs of consecutive frames were averaged to achieve one ensemble velocity vector (Meinhart et al. 2000). Given the systems frame rate of 65 fps and the fact that 10 frames were used to obtain each velocity, the time interval between the successive velocity estimates was 154 ms. As the FT2ADV and the VIV were not hardware synchronized, data from the two instruments were synchronized by cross correlating the time series of both instruments to find the time offset. The time offset was then used to realign the velocity measurement from the VIV and the FT2ADV. To compare the velocity measurement at a given time, the velocity data from the FT2ADV were interpolated to match the sampling frequency of the VIV.

The SNR values calculated by the primary peak ratio method as described in section 2b were also recorded to determine the reliability of each velocity estimate. The number of particles detected in each frame and their size range after the adaptive thresholding step were also reported.

e. Real-time processing

In many remote applications, such as long-term mooring and autonomous platforms, the VIV might be deployed for a long period of time, and the recorded videos might not be readily accessible to perform the velocity measurement until after the deployment. As a result, it is desirable for the VIV to perform real-time processing with the internal computer. The real-time velocity measurement would allow the VIV to use significantly less data storage and also allow the velocity measurement to be sent remotely as a small data packet to inform a remote vehicle about its relative velocity.

To explore the ability of the VIV to perform real-time velocity measurement, data from the field deployment were used to benchmark the processing speed of several candidate internal computers. For this study, three models of Raspberry Pi: model Zero W, 3A+ and 4B (2 GB RAM) were evaluated. The power consumption of the computers during the analysis was also recorded by measuring the current draw of the computers.
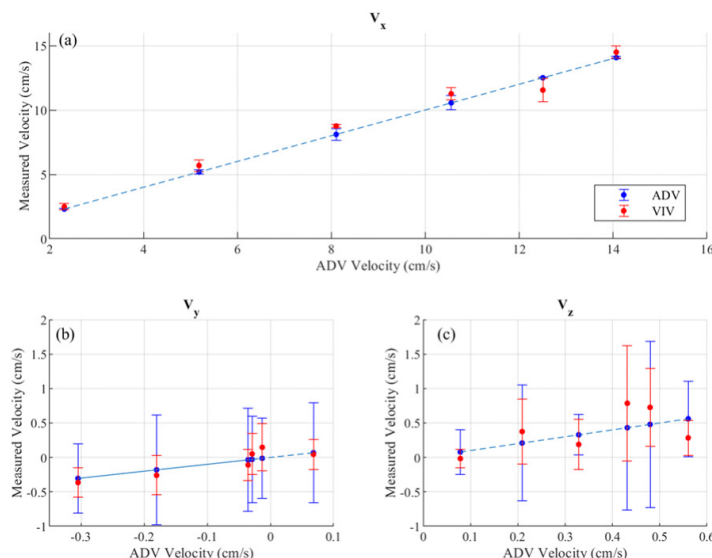
FIG. 7. The flow velocity as measured by the FT2ADV and the VIV. Each data point of the ADV is the average velocity value over 60 s, and the error bar indicates the standard deviation. Each data point of the VIV is the ensemble average over 30 consecutive frames, and the error bar indicate the standard deviation of the velocity within the ensemble average.

Additionally, a Jetson Nano developer kit (Nvidia), another low-cost single-board computer, was used because it represents a family of single-board computer with a more powerful graphical processing unit that enables accelerated image processing. It should be noted that Jetson Nano consumes more power than Raspberry Pi computers and also has a larger footprint that does not fit inside the current VIV housing. As such, the result from the Jetson Nano is used to demonstrate the potential for future improvement of the VIV. The detail of testing conditions can be found in the online supplementary material section S1.

3. Results

a. Laboratory validation

In the laboratory experiment, at slower flow speed, the flow in the flume exhibits minimal fluctuation as measured by the ADV (Fig. S1). The results from these slower and unidirectional flows (Fig. 6a) indicate linearity between the displacement in the object plane (ΔX, ΔY) and the calculated displacement in the image plane ($\hat{x}$, $\hat{y}$) as predicted by (4). The cross-correlation map of two consecutive frames (Fig. 6c) shows a very distinct and narrow peak, which indicates high SNR of the velocity measurement.

However, as the flow became faster and more turbulent as shown by the ADV measurement (Fig. S1b), the cross-correlation map between two frames becomes very noisy, and the primary peak is less distinct from the rest of the map (Fig. 6d). Even though the velocity estimation of the ensemble average over 30 frames still produces linear relationship, the

high standard deviations and noisy correlation maps indicate that the estimations in this regime are unreliable (Fig. 6b). This result emphasizes the limitation of the simplified correlation method that requires uniform flow.

The measurements using the stereo mirror setup in the slow flow regime are shown in Fig. 7 to compare the velocity measurement of the ADV to that of the VIV. As measured by the ADV over 60 s, the unidirectional flow in the flume (V_x) was varied from 2 to 14 cm s^{-1}. The velocity in the other two directions (V_y and V_z) fluctuates around 0 cm s^{-1}. The comparison between the two instruments shows that the velocity measured by the VIV falls within the value measured by the ADV within one standard deviation of each instrument, indicating good agreement between the two instruments.

b. Field experiment

Figures 8 and 9 show the comparison of the velocity measured by the VIV and the FT2ADV over 150 s from the field deployment. The raw data of the VIV are color-coded by the SNR values as calculated by the primary peak ratio method. As shown, the raw velocity estimation of the VIV has good agreement with the ADV in V_x and V_y when the SNR values are above 10dB, but the estimation fluctuates rapidly and becomes less reliable as the SNR drops below 10dB. However, the VIV consistently underestimates the velocity in the z direction regardless of the SNR.

For V_x and V_y, a velocity estimation with SNR > 10 dB has a cross-correlation map similar to Fig. 10b where the narrow primary peak can be reliably detected. If smaller interrogation
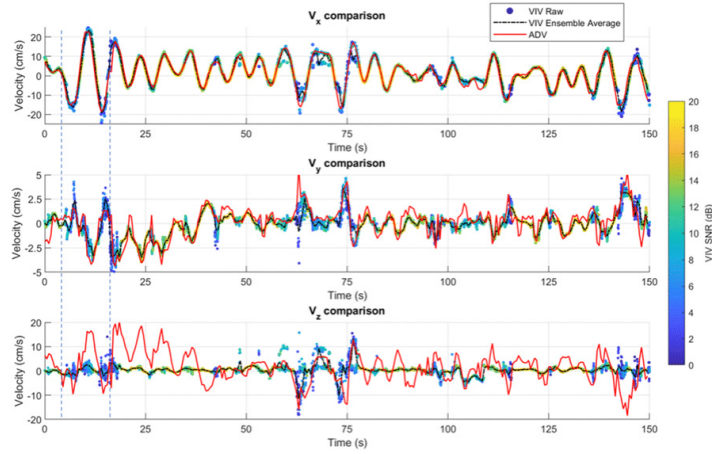
FIG. 8. The time series comparison of the data from the VIV and from the FT2ADV probe the field deployment. VIV raw is the instantaneous velocity estimate from the VIV between every consecutive frame recorded at 65 fps. The color of VIV raw represents the signal-to-noise ratio (SNR) calculated from the primary peak ratio of cross-correlation maps. VIV ensemble average is the ensemble average of VIV raw over 10 velocity estimates. The two vertical dashed lines indicate the time points at 4.8 and 16.4 s, which are reviewed in detail in Fig. 10.

windows of 100×100 pixels with 50% overlap are used to perform cross correlation, the result in Fig. 10c shows that particles in each region are moving in the same general direction, validating the uniform flow assumptions of the simplified correlation method. However, the SNR of each small interrogation window can be different from the overall cross correlation. In particular, the regions with out-of-focus particles, which corresponds to larger binary mask, such as regions on the left edge of Fig. 10a, the cross-correlation maps can be noisy and yields lower SNR values. On the other hand, the correlation map of a velocity estimation with SNR < 10 dB (Figs. 10d–e) shows a noisy map with a broader primary peak. The correlation of smaller integration windows show that particles are moving in different directions throughout the field of view of the camera (Fig. 10d). This behavior violates the assumptions of the simplified correlation method, rendering the data point to become less reliable. In this periodic flow, the SNR of the VIV is typically high when the main flow is accelerating, but the SNR drops when the acceleration slows down to change direction at peaks and troughs of the velocity oscillation.

Even though the velocity estimation with low SNR values causes the raw data to fluctuate, this issue can be alleviated with the ensemble average of 10 consecutive frames. This time-averaged method improves the root-mean-square errors of V_x and V_y by 42% and 47%, respectively, as shown in Fig. 9. The ensemble average data show a good agreement in V_x and V_y with low root-mean-squared errors of 1.43 and $0.5\,\mathrm{cm\,s^{-1}}$ within the velocity range of 20 and $5\,\mathrm{cm\,s^{-1}}$, respectively. As shown, the VIV can measure the flow speed up to $20\,\mathrm{cm\,s^{-1}}$ with a good agreement with the ADV.

c. Real-time performance

Table 2 summarizes the results from all tested single-board computers. The Raspberry Pi Zero W, which was used in the presented ocean-going VIV, has a relatively slow processing rate of five seconds per velocity estimate. The more powerful Raspberry Pi models 3A+ and 4B can approximately estimate one velocity per second but consumes more power, which can limit the amount of time the instrument can be deployed autonomously with the same amount of battery power. The Jetson Nano can perform at a much faster rate of 3.76 estimations per second, but the power consumption of this powerful processing unit is triple the rate of the Raspberry Pi Zero.

4. Discussion

a. Velocity estimation

The results from the laboratory and the field experiment demonstrate that the VIV and its processing algorithm can estimate the flow parallel to the face of the viewport well when the flow is approximately uniform in the sampling volume. When the flow becomes more turbulent, an individual velocity estimation is less reliable with low SNR value, but the unreliability can be alleviated by performing ensemble average over a short period of time. However, the VIV consistently underestimates the axial velocity component that is perpendicular to the viewport.

This discrepancy in V_z is a result of larger sampling volume of the VIV compared to the ADV. The FT2ADV has a small cylindrical sampling volume with 6 mm diameter and 9 mm height, while the VIV has a sampling of volume of
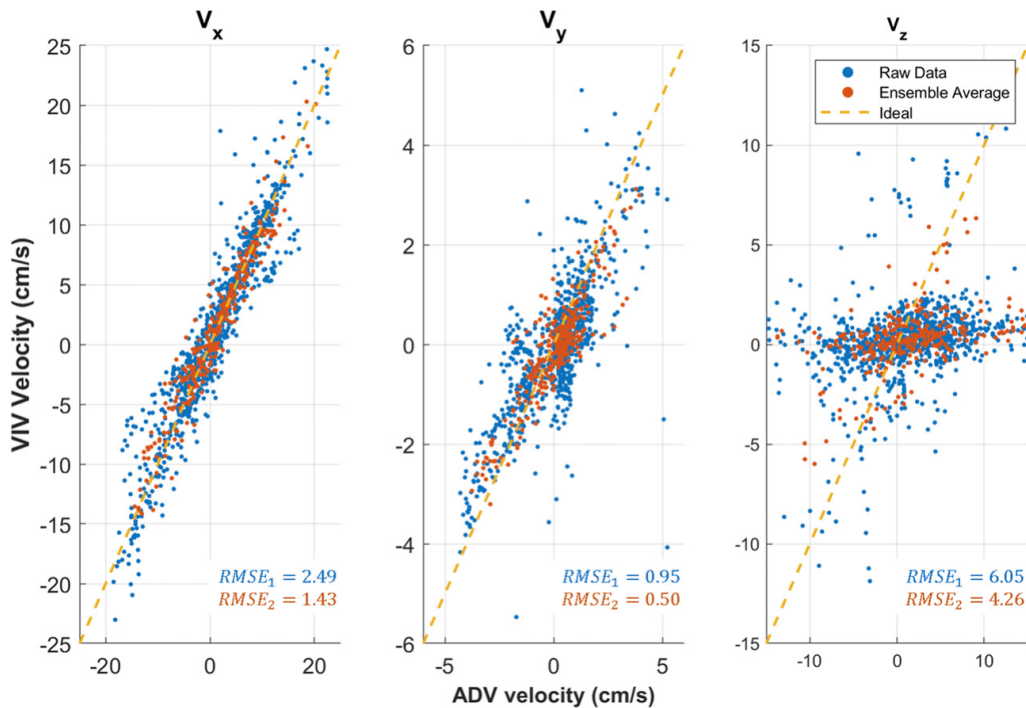
FIG. 9. The scattered plots of the data from the raw VIV measurement (blue) and from the ensemble average (red) compared to the measurement from the FT2ADV probe. The dashed lines indicate ideal match between the two instruments. $RMSE_1$ is the root-mean-squared error calculated from the raw VIV measurement, while $RMSE_2$ is calculated from the ensemble average.

approximately $20\,mm \times 20\,mm \times 20\,mm$. The experiment was setup such that the sampling volume of the ADV was in the middle of the sampling volume of the VIV. When averaging over the entire sampling volume, the VIV sampled more particles that were closer to the viewport of the instrument. The speed of these particles in z direction was reduced due to the blocking from the cylindrical, which is 7.6 cm in diameter. As a result, when averaging over the entire sampling volume, the slower speed of these closer particles resulted in underestimation of the V_z component.

This limitation in the axial flow estimation is circumstantial based on the constraints of the housing diameter. If all three velocity components are needed, the VIV can be scaled up to larger housing that allows the mirrors to be tilted more and moves the overlapping field of view farther away. The illumination can also be moved outside of the housing to accommodate the new configuration. This adjustment would allow more accurate 3D studies with the trade-off of the compact size of the instrument.

With the current iteration of the VIV, the instrument is mainly suitable for estimating nonturbulent slow flow and is not a perfect replacement of an ADV, which can be used in more complex flow regimes. We note, that in order to address the issue of reliability we caution users to carefully observe the SNR of each velocity estimation, and when the SNR values become low, the system's estimate of the mean velocity is likely to be unreliable. Additionally, the VIV is limited to estimating flow parallel to the face of the viewport, so the orientation of the instrument is critical in an actual flow study. Accordingly, the instrument should be oriented such that the main flow is parallel to the face of the viewport, so the main velocity components can be estimated.

Despite this limitation, the VIV has potential for many practical uses. Many ecological studies do not need to resolve all three velocity components to understand the ecological implications of the ocean current (Madin and Connolly 2006; Mach et al. 2011; Johansen 2014). Moreover, the low cost of the system permits increased feasibility so that multiple units could be used to cover a larger spatial area in a single deployment. The deployment of multiple units will be particularly effective in recording and understanding the flow over a complex benthic structure with relatively low flow rate, such as coral reefs. Presently, this type of study is currently being done with multiple ADVs (Hench and Rosman 2013; Huang et al. 2012) or ADCPs (Gaylord et al. 2007; Rogers et al. 2018). Since the spatial variability in flow is of importance, increased spatial sampling density for the same price is definitely of advantage.
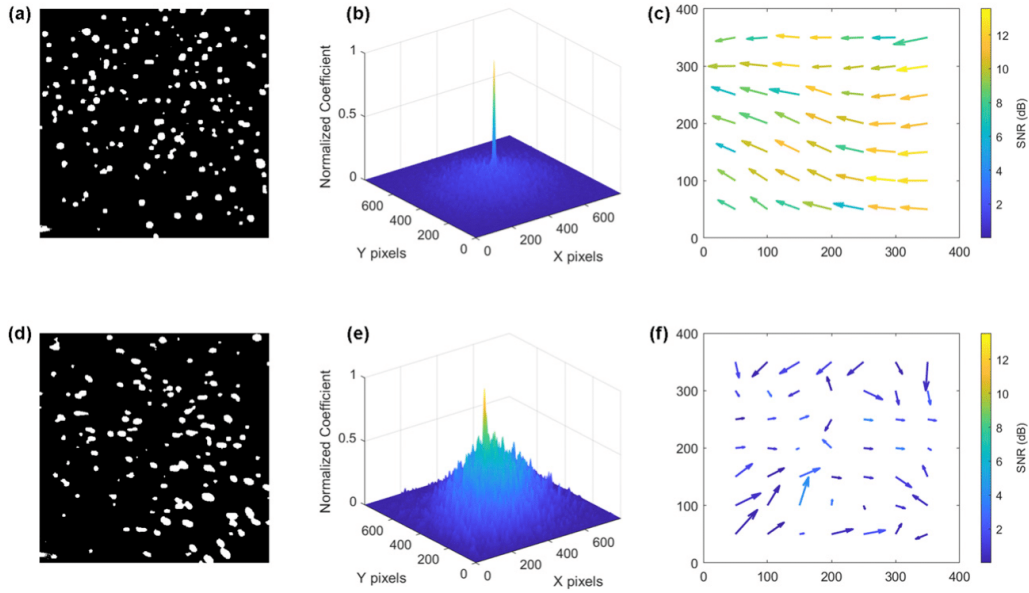
FIG. 10. Examples of cross-correlation maps from two velocity estimates with high and low SNR from the field deployment. The time points are marked by dashed lines in Fig. 8. The cross-correlation maps are obtained from cross correlating the entire 400×400 pixel fields of view of the VIV. At $t = 4.8$ s, (a) the binary image of particles in the region of interest corresponds to (b) a velocity estimate with a high SNR of 15 dB. (c) The corresponding velocity field, obtained from smaller 100×100 pixel interrogation windows with 50% overlap, shows flow of particles in similar direction. The color of the arrows represents the SNR field of each smaller interrogation windows. At $t = 16.4$ s, (d) the binary image of particles corresponds to (e) a velocity estimate with a low SNR of 5 dB. (f) The corresponding velocity field shows particles moving in different directions. Both correlation maps yield similar velocity estimate in the main flow of approximately 1.5 cm s^{-1}.

b. Ambient particles

During the field deployment, the particles that were detected by the adaptive thresholding method in each frame, have the mean equivalent radii between 4 and 6 pixels (Fig. 11a) with overall average standard deviation of 2.8 pixels. This narrow range of particle size within each frame and also between frames indicates that the assumption of uniform size distribution was valid in this deployment. The instrument also experiences particle counts in the range of 5–20 particles per milliliter (Fig. 11b), which is a typical particle concentration in benthic environment as reported by other studies (Reynolds et al. 2010; Bertuccioli et al. 1999). The VIV relies on natural particles without the need for particle seeding, so it is susceptible to ambient conditions. With the current optical setup, the instrument can only image particles of $50 \mu m$ or larger, so it needs to operate in environments with sufficient number of particles in this size range, such as coastal areas. To operate in environments with very clear water, such as open ocean (O'Dowd et al. 2010), the instrument will need a more advanced camera system that can image smaller particles.

As an additional constraint, the VIV might not work as well when particle concentrations are particularly high. At higher particle counts per image frame, crowding can cause the adaptive thresholding preprocessing step to group several particles in the same clump, reducing the amount of signal. This would result in a source of the noise in each particle movement, even though all particles might be flowing in the same direction. This noise accumulates in the cross-correlation map, causing the cross-correlation values to be noisy. A more rigorous study of the performance of the algorithm and the VIV with various particle concentrations and sizes would be a valuable adjunct to this work. Nevertheless, the VIV can perform well in typical particle concentrations in coastal environments as shown in the field experiment.

c. Real-time processing

The current iteration of the VIV utilizes a Raspberry Pi Zero W because of its low cost and low power consumption,

TABLE 2. Sampling rate and power consumption of single-board computers performing velocity measurement.

Computer	Sampling rate (Hz)	Power consumption (W)
Raspberry Pi Zero W	0.21 ± 0.2	1.0 ± 0.1
Raspberry Pi 3A+	0.99 ± 0.2	1.5 ± 0.2
Raspberry Pi 4B	1.31 ± 0.1	2.8 ± 0.1
Jetson Nano	3.76 ± 0.4	3.1 ± 0.1
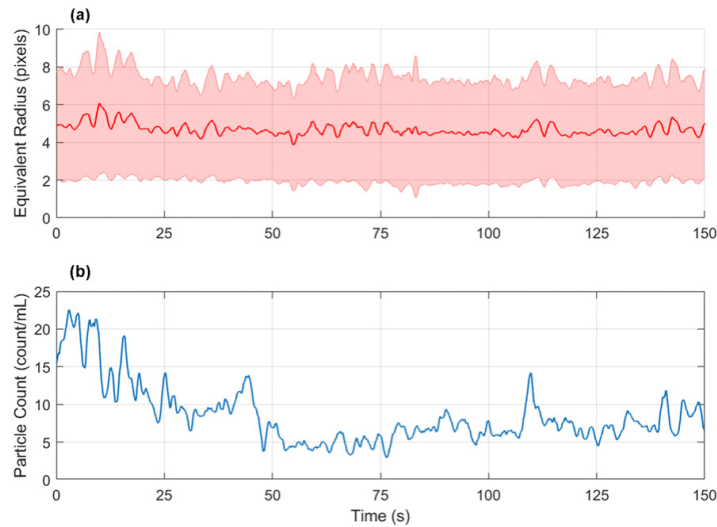
FIG. 11. (a) The time series of equivalent radius of particles detected by the adaptive thresholding process from the field deployment. The line indicates the mean radius in each frame, and the shaded error bar indicates the standard error of the radius. (b) The time series of the particle concentrations from the field deployment.

so it is not suitable for real-time velocity estimation. However, the VIV is designed such that the system is compatible with other more powerful Raspberry Pi computing units, such as Raspberry Pi model 3A+ and 4B, that can perform the velocity measurement at approximately 1 sample per second. Even though this sampling rate is not sufficient for small-scale flow that changes rapidly, such as turbulence, it still suits many oceanographic applications that measure medium-scale flow, such as the periodic wave shown in Fig. 8, which has a period of approximately 9 s. These more powerful computing units can readily fit inside the waterproof housing and only require minimal change in the internal mounting.

With more a powerful computer, such as the Jetson Nano, the algorithm can be performed very rapidly and achieve a higher sampling. This high real-time sampling rate indicates that the VIV can be improved with more sophisticated hardware and can be deployed to study flows that change more rapidly.

d. Future improvements

With the current setup, there are only two views of the sampling volume available to the VIV. In considering further development and application of a more advanced system, future improvement might involve adding more views either by using more complex mirror optics or more cameras. More complex optics and additional views will result in imaging more particles that are in-focus, resulting in cleaner cross-correlation maps. As envisioned, these improvements will also allow the instrument to perform more precise particle correspondence that enables the reconstruction of velocity fields as opposed

to a single vector. More powerful computer can also be used to enhance processing such that more complex algorithms, such as tomographic PIV, can be implemented.

Additionally, the VIV is designed to be modular and is based of components that are easily accessible through maker practice. With the rapid advancement in the maker technology, there will be new electronic components, such as cameras and illumination modules, that can improve the performance of the VIV while only require minimal redesign of the system. In addition to being low cost, the VIV is also designed to have low complexity and can be programmed through simple platforms including both Python and Arduino programming. These two platforms are accessible to researchers that do not have extensive electrical engineering training, allowing the VIV to be readily customized based on the specific need of each research study. These advantages will allow the instrument to be used by researchers from many disciplines in oceanography and limnology.

5. Conclusions

In this study, we designed, fabricated, and tested an optical system for measuring currents using the ambient distribution of imaged particles to track the flow. The Video Velocimeter (VIV) was developed, calibrated in the laboratory, and then deployed in the field to reconstruct oceanographic currents. As demonstrated, when used in nonturbulent flow, the VIV can estimate mean flow velocity with root-mean-squared errors of the main flow within 10% of the $\pm 20 \, \mathrm{cm \, s^{-1}}$ measurement range when compared to an ADV.

The key to understand many biological and physical features of the ocean lies in the understanding of the ocean currents that determine the fate of those features. There are still many challenges in measuring the small-scale flow of these currents around complex benthic structure that cannot be accomplished by a single instrument like an ADCP or ADV. The resulting science that is facilitated by having multiple sensors at different locations will surely be enhanced. By developing a new tool that is inexpensive and easy to use by researchers across many disciplines, we hope that the VIV will be a platform that facilitates new discoveries in the underwater environment.

REFERENCES

Bertuccioli, L., G. I. Roth, J. Katz, and T. R. Osborn, 1999: A submersible particle image velocimetry system for turbulence measurements in the bottom boundary layer. *J. Atmos. Oceanic Technol.*, **16**, 1635–1646, https://doi.org/10.1175/1520-0426(1999)016<1635:ASPIVS>2.0.CO;2.

Bourdon, C. J., M. G. Olsen, and A. D. Gorby, 2003: Validation of an analytical solution for depth of correlation in microscopic particle image velocimetry. *Meas. Sci. Technol.*, **15**, 318–327, https://doi.org/10.1088/0957-0233/15/2/002.

Chételat, O., and K. C. Kim, 2002: Miniature particle image velocimetry system with LED in-line illumination. *Meas. Sci. Technol.*, **13**, 1006, https://doi.org/10.1088/0957-0233/13/7/306.

——, S. Y. Yoon, and K. C. Kim, 2001: Design and construction of a miniature PIV (MPIV) system. *KSME Int. J.*, **15**, 1775–1783, https://doi.org/10.1007/BF03185134.

Davis, C. S., G. R. Flierl, P. H. Wiebe, and P. J. S. Franks, 1991: Micropatchiness, turbulence and recruitment in plankton. *J. Mar. Res.*, **49**, 109–151, https://doi.org/10.1357/002224091784968602.

Ekman, V. W., 1932: An improved type of current-meter. *ICES J. Mar. Sci.*, **7**, 3–10, https://doi.org/10.1093/icesjms/7.1.3.

Estevadeordal, J., and L. Goss, 2005: PIV with LED: Particle shadow velocimetry (PSV). *43rd AIAA Aerospace Science Meeting and Exhibit*, Reno, NV, AIAA, https://doi.org/10.2514/6.2005-37.

Fouras, A., D. Lo Jacono, C. V. Nguyen, and K. Hourigan, 2009: Volumetric correlation PIV: A new technique for 3D velocity vector field measurement. *Experiments in Fluids*, Vol. 47, Springer, 569–577.

Fuentes-Perez, J. F., C. Meurer, J. A. Tuhtan, and M. Kruusmaa, 2018: Differential pressure sensors for underwater speedometry in variable velocity and acceleration conditions. *IEEE J. Ocean. Eng.*, **43**, 418–426, https://doi.org/10.1109/JOE.2017.2767786.

Garwood, J. C., A. J. Lucas, P. Naughton, M. H. Alford, P. L. D. Roberts, J. S. Jaffe, L. deGelleke, and P. J. S. Franks, 2020: A novel cross-shore transport mechanism revealed by subsurface, robotic larval mimics: Internal wave deformation of the background velocity field. *Limnol. Oceanogr.*, **65**, 1456–1470, https://doi.org/10.1002/lno.11400.

Gaylord, B., and Coauthors, 2007: Spatial patterns of flow and their modification within and around a giant kelp forest. *Limnol. Oceanogr.*, **52**, 1838–1852, https://doi.org/10.4319/lo.2007.52.5.1838.

Hagsäter, S. M., C. H. Westergaard, H. Bruus, and J. P. Kutter, 2008: Investigations on LED illumination for micro-PIV including a novel front-lit configuration. *Exp. Fluids*, **44**, 211–219, https://doi.org/10.1007/s00348-007-0394-z.

Hench, J. L., and J. H. Rosman, 2013: Observations of spatial flow patterns at the coral colony scale on a shallow reef flat. *J. Geophys. Res. Oceans*, **118**, 1142–1156, https://doi.org/10.1002/jgrc.20105.

Hill, P., A. R. Nowell, and P. Jumars, 1992: Encounter rate by turbulent shear of particles similar in diameter to the Kolmogorov scale. *J. Mar. Res.*, **50**, 643–668, https://doi.org/10.1357/002224092784797539.

Huang, Z.-C., L. Lenain, W. K. Melville, J. H. Middleton, B. Reineman, N. Statom, and R. M. McCabe, 2012: Dissipation of wave energy and turbulence in a shallow coral reef lagoon. *J. Geophys. Res.*, **117**, C03015, https://doi.org/10.1029/2011JC007202.

Jaffe, J. S., P. J. S. Franks, P. L. D. Roberts, D. Mirza, C. Schurgers, R. Kastner, and A. Boch, 2017: A swarm of autonomous miniature underwater robot drifters for exploring submesoscale ocean dynamics. *Nat. Commun.*, **8**, 14189, https://doi.org/10.1038/ncomms14189.

Jickells, T. D., 1998: Nutrient biogeochemistry of the coastal zone. *Science*, **281**, 217–222, https://doi.org/10.1126/science.281.5374.217.

Johansen, J. L., 2014: Quantifying water flow within aquatic ecosystems using load cell sensors: A profile of currents experienced by coral reef organisms around Lizard Island, Great Barrier Reef, Australia. *PLOS ONE*, **9**, e83240, https://doi.org/10.1371/journal.pone.0083240.

Jones, I. S. F., 1980: Electromagnetic current meters. *Air-Sea Interaction*, Springer, 219–229.

Katija, K., and J. O. Dabiri, 2008: In situ field measurements of aquatic animal-fluid interactions using a self-contained underwater velocimetry apparatus (SCUVA). *Limnol. Oceanogr. Methods*, **6**, 162–171, https://doi.org/10.4319/lom.2008.6.162.

Knauss, J. A., 1959: Measurements of the Cromwell Current. *Deep-Sea Res.*, **6**, 265–274, https://doi.org/10.1016/0146-6313(59)90086-3.

Lacoursière, J. O., and D. A. Craig, 1990: A small flume for studying the influence of hydrodynamic factors on benthic invertebrate behaviour. *J. North Amer. Benthological Soc.*, **9**, 358–367, https://doi.org/10.2307/1467903.

Liao, Q., H. A. Bootsma, J. Xiao, J. V. Klump, A. Hume, M. H. Long, and P. Berg, 2009: Development of an in situ underwater particle image velocimetry (UWPIV) system. *Limnol. Oceanogr. Methods*, **7**, 169–184, https://doi.org/10.4319/lom.2009.7.169.

Liberzon, A., D. Lasagna, M. Aubert, P. Bachant, and J. Borg, 2016: Openpiv/Openpiv-Python: Updated Pyprocess with extended area search method. ePrints Soton, accessed 19 May 2020, https://eprints.soton.ac.uk/434472/.

Lohrmann, A., R. Cabrera, and N. C. Kraus, 1994: Acoustic-Doppler velocimeter (ADV) for laboratory use. *Proc. Symp. on Hydraulic Measurements and Experimentation*, Buffalo, NY, ASCE, 351–365.

Mach, K. J., S. K. Tepler, A. V. Staaf, J. C. Bohnhoff, and M. W. Denny, 2011: Failure by fatigue in the field: A model of fatigue breakage for the macroalga *Mazzaella*, with validation. *J. Exp. Biol.*, **214**, 1571–1585, https://doi.org/10.1242/jeb.051623.

MacVicar, B. J., E. Beaulieu, V. Champagne, and A. G. Roy, 2007: Measuring water velocity in highly turbulent flows: Field tests of an electromagnetic current meter (ECM) and an acoustic Doppler velocimeter (ADV). *Earth Surf. Processes Landforms*, **32**, 1412–1432, https://doi.org/10.1002/esp.1497.

Madin, J. S., and S. R. Connolly, 2006: Ecological consequences of major hydrodynamic disturbances on coral reefs. *Nature*, **444**, 477–480, https://doi.org/10.1038/nature05328.

Martin, A. P., and K. J. Richards, 2001: Mechanisms for vertical nutrient transport within a North Atlantic mesoscale eddy. *Deep-Sea Res. II*, **48**, 757–773, https://doi.org/10.1016/S0967-0645(00)00096-5.

Meinhart, C. D., S. T. Wereley, and J. G. Santiago, 2000: A PIV algorithm for estimating time-averaged velocity fields. *J. Fluids Eng.*, **122**, 285–289, https://doi.org/10.1115/1.483256.

O'Dowd, C., C. Monahan, and M. Dall'Osto, 2010: On the occurrence of open ocean particle production and growth events. *Geophys. Res. Lett.*, **37**, L19805, https://doi.org/10.1029/2010GL044679.

Olsen, M. G., and R. J. Adrian, 2000: Out-of-focus effects on particle image visibility and correlation in microscopic particle image velocimetry. *Experiments in Fluids*, Vol. 29, Springer, S166–S174.

Pagnutti, M. A., R. E. Ryan, G. J. Cazenavette, M. J. Gold, R. Harlan, E. Leggett, and J. F. Pagnutti, 2017: Laying the foundation to use Raspberry Pi 3 V2 camera module imagery for scientific and engineering purposes. *J. Electron. Imaging*, **26**, 013014, https://doi.org/10.1117/1.JEI.26.1.013014.

Pineda, J., J. Hare, and S. Sponaugle, 2011: Larval transport and dispersal in the coastal ocean and consequences for population connectivity. *Oceanography*, **20** (3), 22–39, https://doi.org/10.5670/oceanog.2007.27.

Prasad, A. K., 2000: Stereoscopic particle image velocimetry. *Exp. Fluids*, **29**, 103–116, https://doi.org/10.1007/s003480000143.

——, 2007: Particle image velocimetry. *Curr. Sci.*, **79**, 51–60.

Raffel, M., C. E. Willert, S. T. Wereley, and J. Kompenhans, 1989: *Particle Image Velocimetry: A Practical Guide*. Springer, 30 pp.

Reynolds, R. A., D. Stramski, V. M. Wright, and S. B. Woźniak, 2010: Measurements and characterization of particle size distributions in coastal waters. *J. Geophys. Res.*, **115**, C08024, https://doi.org/10.1029/2009JC005930.

Rogers, J. S., S. A. Maticka, V. Chirayath, C. B. Woodson, J. J. Alonso, and S. G. Monismith, 2018: Connecting flow over complex terrain to hydrodynamic roughness on a coral reef. *J. Phys. Oceanogr.*, **48**, 1567–1587, https://doi.org/10.1175/JPO-D-18-0013.1.

Rothschild, B. J., and T. R. Osborn, 1988: Small-scale turbulence and plankton contact rates. *J. Plankton Res.*, **10**, 465–474, https://doi.org/10.1093/plankt/10.3.465.

Rudnick, D. L., R. E. Davis, C. C. Eriksen, D. M. Fratantoni, and M. J. Perry, 2004: Underwater gliders for ocean research. *Mar. Technol. Soc. J.*, **38**, 73–84, https://doi.org/10.4031/002533204787522703.

Smith, W. A. M. N., 2008: A submersible three-dimensional particle tracking velocimetry system for flow visualization in the coastal ocean. *Limnol. Oceanogr. Methods*, **6**, 96–104, https://doi.org/10.4319/lom.2008.6.96.

Steinbuck, J. V., and Coauthors, 2010: An autonomous open-ocean stereoscopic PIV profiler. *J. Atmos. Oceanic Technol.*, **27**, 1362–1380, https://doi.org/10.1175/2010JTECHO694.1.

Tanenbaum, J. G., A. M. Williams, A. Desjardins, and K. Tanenbaum, 2013: Democratizing technology: Pleasure, utility and expressiveness in DIY and maker practice. *Proc. Conf. on Human Factors in Computing Systems*, New York, NY, ACM, 2603–2612.

Tritico, H. M., A. J. Cotel, and J. N. Clarke, 2007: Development, testing and demonstration of a portable submersible miniature particle imaging velocimetry device. *Meas. Sci. Technol.*, **18**, 2555–2562, https://doi.org/10.1088/0957-0233/18/8/031.

Weller, R. A., and R. E. Davis, 1980: A vector measuring current meter. *Deep-Sea Res.*, **27A**, 565–581, https://doi.org/10.1016/0198-0149(80)90041-2.

Wellner, P. D., 1993: Adaptive thresholding for the DigitalDesk. EuroPARC Tech. Rep. EPC-93-110, 14 pp.

Xue, Z., J. J. Charonko, and P. P. Vlachos, 2014: Particle image velocimetry correlation signal-to-noise ratio metrics and measurement uncertainty quantification. *Meas. Sci. Technol.*, **25**, 115301, https://doi.org/10.1088/0957-0233/25/11/115301.

Yu, L., and B. Pan, 2016: Structure parameter analysis and uncertainty evaluation for single-camera stereo-digital image correlation with a four-mirror adapter. *Appl. Opt.*, **55**, 6936, https://doi.org/10.1364/AO.55.006936.

Zhang, Z., 1999: Flexible camera calibration by viewing a plane from unknown orientations. *Proc. Seventh IEEE Int. Conf. on Computer Vision*, Kerkyra, Greece, IEEE, 666–673, https://doi.org/10.1109/ICCV.1999.791289.
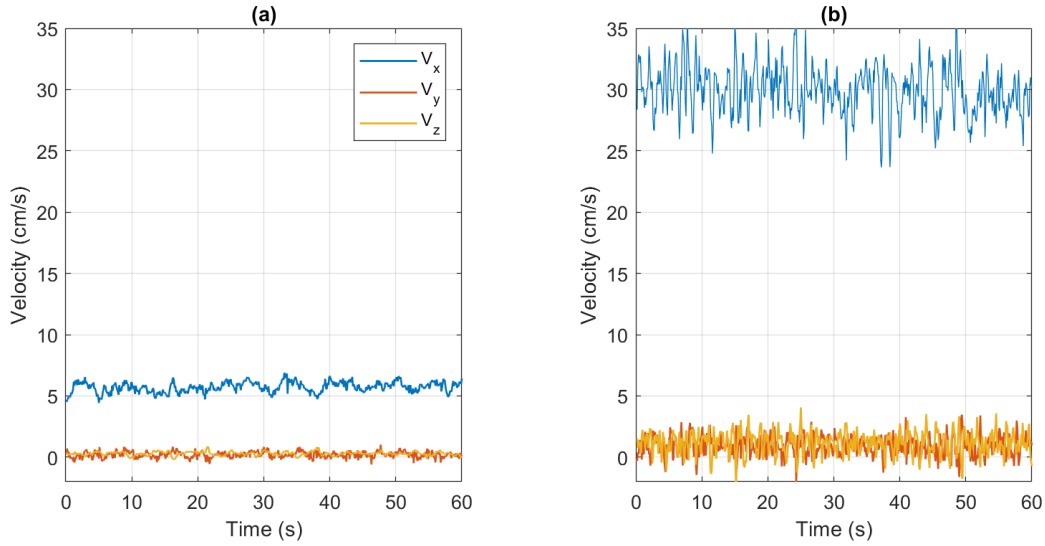
Figure S1 The behaviors of flow in the experimental flume as measured by an ADV. (a) The flow at lowest velocity setting where the main flow velocity is 5.7±0.4 cm/s. (b) The flow at highest velocity setting where the main flow velocity is 29.9±2.0 cm/s.

S1. Real-time Processing Detailed Method

To explore the ability of the VIV to perform real-time velocity measurement, data from the field deployment was used to benchmark the processing speed of several candidate internal computers. For this study, three models of Raspberry Pi: model Zero W, 3A+ and 4B (2GB RAM) were evaluated. All three boards ran on 32GB Class 10 microSD Card (SanDisk, California) flashed with Rasbperry Pi Operating System. Each unit was powered by a benchtop power supply (Eventek) that supplied 5V. The current draw of the computers was measured by connecting a multimeter (Extech Instruments, Massachusetts) from the positive end of the power supply to the positive input of the computer board.

The video from the deployment shown in Fig. 5 was read by each computer, which was programmed to obtain two consecutive frames from the video ports and then run the full processing algorithm to estimate the velocity components before obtaining the next pair of frames. All programming was done in Python 3.7. The video decoding and image processing were handled by OpenCV package, and the image cross correlation and peak detection were handled by OpenPIV package. The analysis time for each pair of images as measured in the Python code was recorded for 1000 velocity estimations. The data presented in Table 2 represent the mean and the standard deviation from the set of 100 measurements.

Additionally, a Jetson Nano developer kit (Nvidia) with 4GB RAM, another low-cost single board computer, was also tested. It represents a family of single board computer with a more powerful graphical processing unit that enables accelerated image processing. The developer kit was chosen for this test because it worked natively with Raspberry Pi Camera V2, which was used in the VIV, without any need for additional software installation. The experimental setup for the Nano developer kit was the same as for the Raspberry Pi boards, but the SD card was instead flashed with Ubuntu 18.04 operating system.

15

Chapter 1, in full, is a reprint of the material as it appears in Journal of Atmospheric and Oceanic Technology. Lertvilai, Pichaya; Roberts, Paul, L.D.; Jaffe, Jules, S. 2021. The dissertation author was the primary investigator and author of this paper.

Chapter 2: The in situ plankton assemblage eXplorer (IPAX): an inexpensive underwater imaging system for zooplankton study

Methods in Ecology and Evolution — BRITISH ECOLOGICAL SOCIETY

The In situ Plankton Assemblage eXplorer (IPAX): An inexpensive underwater imaging system for zooplankton study

Pichaya Lertvilai [ID]

Scripps Institution of Oceanography, University of California, San Diego, La Jolla, CA, USA

Correspondence
Pichaya Lertvilai
Email: plertvil@ucsd.edu

Funding information
Scripps Institution of Oceanography; Mia J. Tegner Fellowship

Handling Editor: Pierre Durand

Abstract

1. Zooplankton play vital ecological roles that maintain aquatic ecosystems. Imaging instruments have enabled in situ observations of these organisms that can be automated and are less invasive than traditional sampling methods. However, these instruments are often costly and require sophisticated engineering expertise to operate.

2. The In situ Plankton Assemblage eXplorer (IPAX) is an open-source low-cost imaging platform for zooplankton studies. The IPAX is a programmable instrument that has powerful LED illumination and a high-resolution camera that can image zooplankton in situ, while material costs are less than USD $450. The optical performance of the instrument was calibrated in the laboratory using a calibration target and preserved zooplankton. The IPAX was then deployed in the field to observe diversity, emergent patterns and phototactic behaviour of demersal zooplankton at night to demonstrate its practicality.

3. Laboratory calibration indicated that the IPAX can resolve 100 μm features with 70% contrast at the focal plane with 5 cm × 3 cm field of view and 5 mm depth of field. The instrument also resolved fine morphological details of preserved zooplankton when in focus. The field deployment demonstrated capability to resolve the myriad of zooplankton present in addition to the different phototactic behaviour that was elicited and observed from the different colour LEDs.

4. The IPAX enables economical and autonomous surveys of zooplankton in various aquatic habitats. Its low cost facilitates construction and deployment of multiple units that can cover large spatial areas, while its versatility also allows adaptations to many experimental needs for aquatic ecology.

KEYWORDS
in situ sensor, open-source hardware, underwater imaging, zooplankton

1 | INTRODUCTION

Zooplankton play many vital ecological roles ranging from supporting aquatic productivity to linking aquatic food webs that maintain both freshwater and saltwater ecosystems (Santhanam, Pachiappan, & Begum, 2018). As a result, investigations of zooplankton are necessary to understand complex aquatic ecosystems. Studies of zooplankton are typically conducted by sampling these animals using

17

various methods, such as towed nets, pumps and traps, and then examining them in laboratory environments (Suthers & Rissik, 2009). However, these sampling methods can be labour-intensive and can also exclude certain types of zooplankton from the samples. For examples, fast swimming zooplankton can avoid net tows (Fleminger & Clutter, 1965), and sensitive organisms can be damaged during collection (Ney & Schumacher, 1978).

Advances in electronics, particularly in imaging platforms, have allowed the development of many imaging systems for zooplankton studies (e.g. Briseño-Avena, Roberts, Franks, & Jaffe, 2015; Cowen & Guigand, 2008; Lombard et al., 2019; Olson & Sosik, 2007). These imaging systems enable in situ observations that can be automated and are less invasive, allowing continuous sampling of zooplankton, including those that are rare and sensitive to traditional sampling methods (Brownlee, Olson, & Sosik, 2016; Cowen & Guigand, 2008). Even though these in situ imaging platforms provide valuable insights into the ecology of zooplankton, they are relatively expensive and require engineering expertise to operate. As a result, the development of a less-expensive imaging system that does not need specialized engineering expertise has potential to expand the user base and can lead to increased knowledge in observational ecology.

To take advantage of modern advances in hardware and software at reduced cost, the In situ Plankton Assemblage eXplorer (IPAX) was developed as an open-source and relatively inexpensive underwater imaging system for zooplankton study. The IPAX is capable of imaging zooplankton in their natural habitats with a high-resolution camera and a powerful LED illumination. This article presents the IPAX, a laboratory testing to validate its performance and a deployment to demonstrate its practicality in the field.

2 | MATERIALS AND METHODS

2.1 | Overview

The IPAX consists of six main subsystems: a core computer, a control board, a camera, an LED flash unit, a power regulator board and rechargeable lithium batteries (Figure 1). The core computer is based on a Raspberry Pi Zero W (Raspberry Pi Foundation), and it communicates with the camera and stores images on an on-board *SD* card. The control board is based on an ATMega328p (Microchip Technology) Arduino-compatible chip, and it performs time keeping with a real-time clock and handles power cycling of the Raspberry Pi to conserve power. The camera is a Raspberry Pi compatible camera based on Sony IMX219 chip with an interchangeable M12 lens (ArduCam). This camera sensor has been characterized in detail for scientific purposes (Ryan et al., 2017), and the M12 mount allows users to switch lenses according to their needs. The focal plane of the camera can also be adjusted manually by moving the lens closer or farther away from the camera sensor. For the following experiments, a 6.0-mm F2.0 lens (PT0620CW, M12 Lenses) was used, and the focal plane was set 50 mm away from the viewport of the IPAX in water.
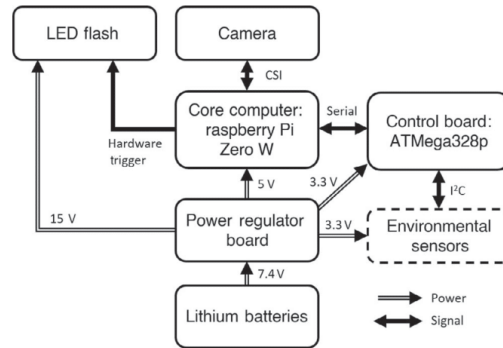
FIGURE 1 System diagram of the In situ Plankton Assemblage eXplorer showing the communication between subsystems and the voltage used by each subsystem. Optional environmental sensors, not required for zooplankton imaging, are shown in the dashed box

TABLE 1 Costs of each subsystem of the In situ Plankton Assemblage eXplorer for building one unit when parts are ordered as a batch for 10 units. The detailed cost breakdown and the bill of materials are available on the data repository (Lertvilai, 2020)

Subsystems	Cost (USD)
Control board	26
Power regulator board	32
Optics and camera	110
Housing	155
Batteries	25
Others (computer and mechanical screws)	85
Total	433

The LED flash unit consists of 10 CREE XPE2 LEDs (CREE Inc.) with focusing lenses (Carclo) and is triggered by signal from the Raspberry Pi to flash during imaging acquisition. The selected LED model has various colours available, and users can install the colours that fit their experimental designs. The 51.8 Wh lithium batteries (IMRBatteries) provide 7.4 V power input to the power regulator board, which then regulates the voltage to appropriate level for each subsystem as shown in Figure 1. The control board, the LED flash unit and the power regulator board are custom-made printed circuit boards, while the Raspberry Pi and the camera are commercially available. All components are packaged inside a cylindrical waterproof housing rated for 100 m (Bluerobotics). The components are securely attached to the interior of the housing by 3D-printed mechanical parts (Figure 2).

Material costs, for building 10 units, are <$450 each (Table 1), and construction of more units, by ordering parts in larger batches, can substantially lower the individual cost. Additional sensors, including depth and temperature sensors from Bluerobotics, can be readily integrated to the waterproof housing and can provide environmental information during each deployment. However,
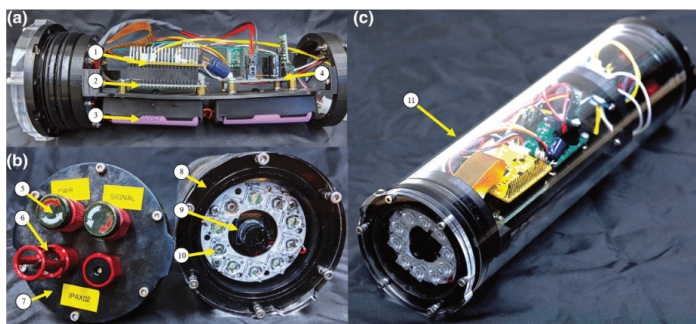
FIGURE 2 Components of the In situ Plankton Assemblage eXplorer. (a) Electronics parts: (1) control board, (2) Raspberry Pi Zero W, (3) lithium batteries, (4) power regulator board. (b) End caps and camera: (5) switches, (6) environmental sensors, (7) aluminium end cap, (8) acrylic viewport, (9) camera and lens, (10) LEDs and lenses. (c) Fully assembled unit: (11) acrylic cylindrical housing. The housing is 9 cm in diameter and 33 cm in length

the incorporation of these sensors will add significant costs to the system.

2.2 | Laboratory calibration

The imaging system of the IPAX was calibrated by arranging the camera and optics attached on a side of a clear acrylic tank filled with saltwater. To facilitate the imaging and reduce stray light, all sides of the tank, except the side with the camera attached, were painted with matte black spray paint. A USAF1951 resolution test chart was then used as a calibration target to evaluate the modulation transfer function (MTF) of the system by calculating the contrast transmittance as a function of the spacing between black bars on white background (Wood et al., 2008). The resolution target was also moved along the camera axis using a translation stage to evaluate the effective depth of field (DOF) of the imaging system.

Additionally, various types of preserved zooplankton were used to evaluate the optical performance of the IPAX. Zooplankton samples of representative taxa preserved in 70% ethanol were mounted on clear glass slides with clear glass cover slips. The slides were immersed in the acrylic tank at the focal plane of the IPAX to optimize the camera setting. Then, the slides were moved along the camera axis to evaluate the effects of DOF on each type of organisms.

2.3 | Field deployment

Two IPAX units were built and deployed in various habitats around Coconut Island in Kaneohe Bay, Hawaii, in August 2019. Both units were identical except for the LEDs used for illumination. One unit had far-red LEDs, with a centre wavelength at 730 nm, and the other unit had 6,500 K white LEDs. The unit with red light was used to record baseline abundance and behaviour of zooplankton as red light above 700 nm reduces observational bias (Cohen & Forward, 2016; Sweatt & Forward, 1985). Comparatively, the unit with white light was used to observe the differences in animal presence that included both natural abundance and phototactic response.

Both IPAX units were deployed simultaneously in protected mangrove lagoons, open lagoons and fringing reefs around the island.

The instruments were secured on the seafloor by weighting them with 2 kg lead blocks. The two units were placed approximately 1-m apart and were positioned with the viewports perpendicular to minimize mutual interference. The camera was set to record videos at 30 frames per second and 1,640 × 1,232 pixels resolution with the exposure time of 500 μs and ISO 200. The LED illumination strobed with 50% duty cycle during image acquisition. Each IPAX produced a beam of light in front of the camera during video recording and minimal light from a small green indicator LED on the Raspberry Pi.

Video recordings were repeated over five nights in the same shallow protected lagoon to investigate the emergent pattern and the phototactic behaviour of demersal zooplankton. The IPAX units were programmed to record a 30-s video every 10 min from 6 p.m. to 7 a.m. every night. This deployment time covered the entire night and also an hour before sunset and an hour after sunrise. For each 30-s video, the last 5 s were extracted and manually analysed to obtain cumulative counts of each group of zooplankton that were identified to taxonomic class level. This cumulative count was then used to obtain the frequency of occurrence of zooplankton over different time of the night.

3 | RESULTS

3.1 | Optical performance

As configured, the IPAX had a field of view of 5 cm × 3 cm at the focal plane located 5-cm away from the acrylic viewport in water. At this distance, the exposure time between 500 and 1,500 μs was sufficient to obtain details of zooplankton without saturating parts of the images. An estimate of system resolution using the contrast transmittance as a function of line spacing (Figure 3) indicated that the instrument resolves a 100-μm feature with 70% contrast at the focal plane. At 20% contrast, the IPAX resolves 20 μm. Results also indicated that for a 100-μm feature, the depth of field was 5 mm with 50% contrast, which yields an effective sampling volume of 7.5 cm^3.

Observation of the images of the preserved zooplankton indicated that the IPAX was able to resolve fine details that can be used for identification. For a smaller zooplankter, such as a Brachyuran

zoea (Figure 4a), the IPAX resolves morphological details well when the object is in focus. The eye spot, the carapace dorsal spine and the abdomen were clearly visible within ±2 mm from the focal plane. The morphological details deteriorated as the zoea moved farther away with the carapace dorsal spine becoming obscure at ±4-mm away. Larger zooplankton, such as a chaetognath (Figure 4b), on the other hand, could be identified within ±10 mm of the focal plane. When within ±5 mm, the fine details, such as the fangs of the chaetognath, were visible.

3.2 | Field results

The IPAX was successfully deployed in the habitats around the island. With fully charged batteries, the instrument lasted for two full nights, equivalent to 26 hr of night-time operation with 80 min of video recording. As observed, although species-level identification

FIGURE 3 The modulation transfer function of the In situ Plankton Assemblage eXplorer with 6-mm F2.0 lens adjusted such that the focal plane is 5-cm away from the viewport

was not possible, the video provided sufficient resolution for identification down to major taxonomic groups (Figure 5). For habitats with low currents, such as protected lagoons (Videos S1–S3), zooplankton could stay in the field of view of the camera for longer periods of time, possibly allowing behavioural observations. For example, sinusoidal movements of polychaetes can be easily observed from the videos (Video S1), while this behaviour was reported to be difficult to stimulate in the laboratory (Clark & Hermans, 2009).

In more energetic habitats, such as fringing reefs and open lagoons (Video S4), the flow moved zooplankton out of the field of view very rapidly. Although this precluded behavioural observations of weak swimmers, the relatively short exposure time of the camera provided sharp images of zooplankton that were suitable for identification and enumeration. With the exposure time of 500 μs, a 100-μm feature can still be resolved even with an ambient flow of 20 cm/s. If shorter exposure times are needed when deployed in energetic habitats, the camera can be set to lower exposure time and higher gain to handle higher flow velocity.

Since the IPAX captured images of open space using backscatter illumination, each image also contained many zooplankton that were out of focus. When plankton density is high, such as in a swarming event, out-of-focus organisms reduced the contrast of the in-focus plankton. Fortunately, the typical abundance was not high enough to cause problems in this field deployment.

The frequency of occurrence of each type of zooplankton over the extracted last 5 s of videos were averaged over five nights, and the 6-point moving average of the counts is shown in Figure 6. This enumeration reveals emergent patterns of zooplankton from the in situ observation. Overall zooplankton were present throughout the deployment time, though the counts were much higher from 8 p.m. to 4 a.m. (Figure 6a). Copepods were present with relatively constant density. Brachyuran zoea were more abundant towards dusk, while chaetognaths were more abundant towards dawn, and polychaetes showed two distinct peaks at dusk and dawn (Figure 6b–e). These emergent patterns were similar to previous reports (Alldredge & King, 1980; Yahel, Yahel, Berman, Jaffe, & Genin, 2005). The comparison between the IPAX units with white light and with red light shows

FIGURE 4 Images of preserved zooplankton [(a) a Brachyuran zoea and (b) a chaetognath] taken in the laboratory at different location relative to the focal plane of the In situ Plankton Assemblage eXplorer. Positive distances indicate that the objects are further away from the viewport than the focal plane, and negative distances closer to the viewport. The scale bars indicate 500 μm

FIGURE 5 Examples of zooplankton images taken from the video recordings. (a) The full field of view from a video recorded by the In situ Plankton Assemblage eXplorer with white light during the deployment in Hawaii. (b) a Stomatopod pseudozoea (c) a Brachyuran zoea, (d) a Stomatopod antizoea, (e) a chaetognath, (f) a polychaete carrying egg mass and (g) a copepod. The scale bar indicates 5 mm in (a) and 1 mm in (b–g)
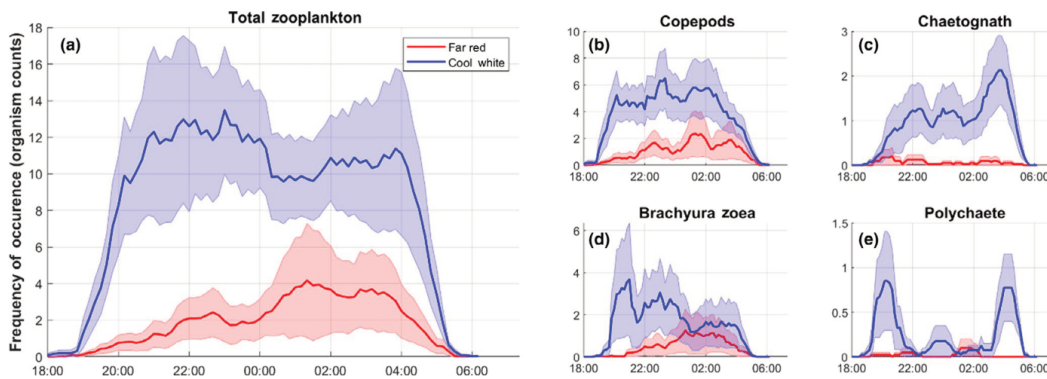
FIGURE 6 The 6-point moving average of frequency of occurrence of zooplankton over five nights from the same shallow lagoon habitat from two In situ Plankton Assemblage eXplorer units with different colour LEDs. The sampling period was 10 min, and each point is the cumulative organism count over extracted 5 s of recordings. The solid lines indicate the average over five nights, and the shaded error bars indicate the standard errors. (a) The total count of all zooplankton. (b–e) The count of each major taxonomic group

an overall strong positive phototactic behaviour of zooplankton in this shallow habitat similar to the report by Tranter et al. (1981). The phototaxis is particularly strong in chaetognath and polychaetes compared to copepods and brachyuran zoea.

4 | DISCUSSION

The laboratory calibrations and the field deployment demonstrate that the IPAX is an imaging platform suitable for in situ observation of zooplankton. It is designed to be autonomous and fully self-contained within one compact waterproof housing with internal batteries and data storage. The simplicity and versatility of the IPAX allow it to be incorporated into many platforms in shallow waters, such as moorings and autonomous vehicles or simply secured on the seafloor. However, for a long-term deployment, bio-fouling might reduce the image quality overtime, so additional anti-fouling capability would then be needed.

Even though this study only used the IPAX to observe photobehaviour of zooplankton, the instrument can potentially be adapted to accommodate various in situ experiments. For instance, deploying two units to observe the same sampling volume will allow three-dimensional tracking within the sampling volume to observe swimming behaviours. With some modifications to the illumination, the IPAX can also be used for studies in benthic habitats, such as examining larval settlement and investigating macroalgae growth. However, caution should be exercised in environments with extremely high flow rate, such as streams and rivers, because the minimum exposure time might not be sufficient to obtain high quality images. Additionally, the system may not work well in very turbid water because high concentration of ambient particles can significantly reduce the contrast of zooplankton, causing unusable images and videos.

The IPAX is also low cost and is designed to be accessible to research laboratories with minimal engineering expertise. Most components, except the main circuit boards, are commercially available, which simplifies fabrication. The main computer is a Raspberry Pi, which can be easily programmed with Python code to set the routine and set camera parameters. The control board can be programmed with an Arduino platform, which bypasses the complexity of low-level programming on the microcontroller. Each subsystem in the IPAX is also designed to be modular, so that users can easily adapt one subsystem to fit their experimental designs without the need to redesign the whole instrument. This modularity is particularly advantageous because technology is rapidly advancing, and better components can become available one at a time.

The affordability of the IPAX also allows multiple units to be built, and the bulk construction will also further reduce manufacturing cost of each unit. Multiple IPAX units will allow an experiment to cover larger spatial area in a single deployment, which can expand our knowledge of gradients and patchiness in zooplankton distribution across multiple habitats. IPAX units can potentially be deployed on mobile platforms, such as the autonomous explorers by Jaffe et al. (2017), to create a swarm of instruments that can track zooplankton distribution in a semi-Lagrangian fashion. Even though multiple units of IPAX can produce large amount of data that can overwhelm manual analyses, there are multiple image processing techniques and machine learning tools for zooplankton classification, such as Ecotaxa (Picheral, Colin, & Irisson, 2017), that can facilitate analyses of the data from IPAX to produce scientifically quantitative data (Benfield et al., 2007).

5 | CONCLUSIONS

In summary, the IPAX is a low-cost underwater imaging system that is capable of observing zooplankton in their natural habitat. The laboratory calibration and the field testing have proven that the IPAX is a suitable tool for in situ zooplankton studies. This autonomous instrument will enable researchers to investigate zooplankton in various aquatic habitats without the need for intensive field labour and specialized engineering expertise. These benefits will facilitate advances in knowledge of zooplankton and ultimately, their role in aquatic ecosystems.

PEER REVIEW

The peer review history for this article is available at https://publons.com/publon/10.1111/2041-210X.13441.

DATA AVAILABILITY STATEMENT

The design of the IPAX is publicly available on https://github.com/plertvilai/IPAX (http://doi.org/10.5281/zenodo.3735054).

ORCID

Pichaya Lertvilai https://orcid.org/0000-0002-5903-1798

REFERENCES

Alldredge, A. L., & King, J. M. (1980). Effects of moonlight on the vertical migration patterns of demersal zooplankton. *Journal of Experimental Marine Biology and Ecology, 44*(2), 133–156. https://doi.org/10.1016/0022-0981(80)90150-1

Benfield, M. C., Grosjean, P., Culverhouse, P. F., Irigoien, X., Sieracki, M. E., Lopez-Urrutia, A., & Gorsky, G. (2007). RAPID: Research on automated plankton identification. *Oceanography, 20*(2), 172–187. https://doi.org/10.5670/oceanog.2007.63

Briseño-Avena, C., Roberts, P. L. D., Franks, P. J. S., & Jaffe, J. S. (2015). ZOOPS- O2: A broadband echosounder with coordinated stereo optical imaging for observing plankton in situ. *Methods in Oceanography, 12*, 36–54. https://doi.org/10.1016/j.mio.2015.07.001

Brownlee, E., Olson, R., & Sosik, H. (2016). Microzooplankton community structure investigated with imaging flow cytometry and automated

live-cell staining. *Marine Ecology Progress Series*, *550*, 65–81. https://doi.org/10.3354/meps11687

Clark, R. B., & Hermans, C. O. (2009). Kinetics of smimming in some smooth-bodied polychaetes. *Journal of Zoology*, *178*(2), 147–159. https://doi.org/10.1111/j.1469-7998.1976.tb06004.x

Cohen, J. H., & Forward, R. B. (2016). Zooplankton diel vertical migration – A review of proximate control. In *Oceanography and marine biology: An annual review* (Vol. 47, pp. 77–110). CRC Press. https://doi.org/10.1201/9781420094220-5

Cowen, R. K., & Guigand, C. M. (2008). In situ ichthyoplankton imaging system (ISIIS): System design and preliminary results. *Limnology and Oceanography: Methods*, *6*(2), 126–132. https://doi.org/10.4319/lom.2008.6.126

Fleminger, A., & Clutter, R. I. (1965). Avoidance of towed nets by zooplankton. *Limnology and Oceanography*, *10*(1), 96–104. https://doi.org/10.4319/lo.1965.10.1.0096

Jaffe, J. S., Franks, P. J. S., Roberts, P. L. D., Mirza, D., Schurgers, C., Kastner, R., & Boch, A. (2017). A swarm of autonomous miniature underwater robot drifters for exploring submesoscale ocean dynamics. *Nature Communications*, *8*, 14189. https://doi.org/10.1038/ncomms14189

Lertvilai, P. (2020). Data from: The In situ Plankton Assemblage eXplorer (IPAX): An inexpensive underwater imaging system for zooplankton study. *Zenodo Repository*, https://doi.org/10.5281/zenodo.3735054

Lombard, F., Boss, E., Waite, A. M., Vogt, M., Uitz, J., Stemmann, L., … Appeltans, W. (2019). Globally consistent quantitative observations of planktonic ecosystems. *Frontiers in Marine Science*, *6*, https://doi.org/10.3389/fmars.2019.00196

Ney, J. J., & Schumacher, P. D. (1978). Assessment of damage to fish larvae by entrainment sampling with submersible pumps. *Environmental Science and Technology*, *12*(6), 715–716. https://doi.org/10.1021/es60142a015

Olson, R. J., & Sosik, H. M. (2007). A submersible imaging-in-flow instrument to analyze nano-and microplankton: Imaging FlowCytobot. *Limnology and Oceanography: Methods*, *5*(6), 195–203. https://doi.org/10.4319/lom.2007.5.195

Picheral, M., Colin, S., & Irisson, J. (2017). *EcoTaxa, a tool for the taxonomic classification of images*. Retrieved from https://ecotaxa.obs-vlfr.fr/

Ryan, R. E., Gold, M., Leggett, E., Pagnutti, M., Harlan, R., Pagnutti, J., & Cazenavette, G. (2017). Laying the foundation to use Raspberry Pi 3 V2 camera module imagery for scientific and engineering purposes. *Journal of Electronic Imaging*, *26*(1). https://doi.org/10.1117/1.jei.26.1.013014

Santhanam, P., Pachiappan, P., & Begum, A. (2018). A method of collection, preservation and identification of Marine Zooplankton. *Basic and applied zooplankton biology* (pp. 1–44). Springer Singapore. https://doi.org/10.1007/978-981-10-7953-5_1

Suthers, I., & Rissik, D. (2009). Sampling methods for plankton. In I. Suthers, & D. Rissik (Eds.), *Plankton: A guide to their ecology and monitoring for water quality* (pp. 73–114). Collingwood, Australia: CSIRO Publishing.

Sweatt, A. J., & Forward, R. B. (1985). Spectral sensitivity of the Chaetognatha Sagitta Hispida Conant. *The Biological Bulletin*, *168*(1), 32–38. https://doi.org/10.2307/1541171

Tranter, D. J., Bulleid, N. C., Campbell, R., Higgins, H. W., Rowe, F., Tranter, H. A., & Smith, D. F. (1981). Nocturnal movements of phototactic zooplankton in shallow waters. *Marine Biology*, *61*(4), 317–326. https://doi.org/10.1007/BF00401571

Wood, M. C., Wang, X., Zheng, B., Li, S., Chen, W., & Liu, H. (2008). Using contrast transfer function to evaluate the effect of motion blur on microscope image quality. In W. R. Chen (Ed.), *Biophotonics and immune responses III* (Vol. 6857, p. 68570F). SPIE. https://doi.org/10.1117/12.759203

Yahel, R., Yahel, G., Berman, T., Jaffe, J. S., & Genin, A. (2005). Diel pattern with abrupt crepuscular changes of zooplankton over a coral reef. *Limnology and Oceanography*, *50*(3), 930–944. https://doi.org/10.4319/lo.2005.50.3.0930

Chapter 2, in full, is a reprint of the material as it appears in Methods in Ecology and Evolution. Lertvilai, Pichaya. 2020. The dissertation author was the primary investigator and author of this paper.

Chapter 3: In situ size and motility measurement of aquatic invertebrates with an underwater stereoscopic camera system using tilted lenses

Abstract

1. In situ observation of traits of aquatic organisms, including size and motility, requires three-dimensional measurements that are commonly done with a stereoscopic imaging system. However, to observe traits of small aquatic invertebrates, the imaging system requires relatively high magnification, which results in a small overlapping volume between the two cameras of a conventional stereoscopic system. The provision of a larger shared volume would therefore be of great advantage, especially, when the organism abundance is low.

2. We implement a stereoscopic system that utilizes a tilted lens approach, known as the Scheimpflug principle, to increase the common imaging volume of two cameras. The system was calibrated and tested in the lab and then deployed in a saltmarsh to observe water boatmen (*Trichocorixa californica*). Processing of the image data from the field deployments resulted in the simultaneous estimation of the traits of body length and swimming speed of the aquatic insects.

3. Our in situ data and subsequent processing reveal that the instrument can capture stereoscopic images that resolve both body length and swimming speed of the aquatic insects. Results indicate that, the relationship between the body length and the swimming speed of the water boatmen is linear in the log-log space with an exponent of 0.28 ± 0.07.

4. Our results demonstrated that the stereoscopic system with tilted lenses can be used to observe key traits of small aquatic organisms in an ecologically relevant context. This work expands the capability of underwater imaging systems to measure important traits of an individual aquatic invertebrate in its natural environment and aids in providing a trait-based approach to zooplankton ecology.

1. Introduction

Small aquatic invertebrates, including zooplankton and aquatic insects, are a group of abundant organisms that occupy a key trophic position in freshwater and marine ecosystems. They often serve as primary consumers that maintain the aquatic food webs by linking the primary producer, such as phytoplankton and algae, to larger predators, such as fish and large invertebrates (Santhanam, Pachiappan, & Begum, 2018; Kiørboe, 2019). As a result, investigations of the invertebrate communities can provide valuable insights to aquatic ecology of both freshwater and marine environments. A common approach to study ecological communities is to perform interspecific analyses between different species or key functional groups (Litchman & Klausmeier, 2008). However, due to their small size and high diversity, identifying the exact species of each individual organism in samples can be difficult and labor intensive. An alternative approach that is gaining interest in ecological studies is trait-based analyses, which focuses on key traits of organisms rather than taxonomy or functional groups (Litchman, Ohman, & Kiørboe, 2013; Kiørboe, Visser, Andersen, & Browman, 2018).

The importance of individual traits can vary, based on ecological functions of interest, but some traits can influence multiple functions and can disproportionately affect the overall ecology. One such trait is the body size. Since the body size directly relates to energy allocation, many other functional traits, such as feeding rate, prey size, growth rate and mortality, scale allometrically with the size of an organism (Litchman et al., 2013). As a result, size can be used to characterize many aspects of aquatic ecology, such as diel vertical migration in zooplankton (Ohman & Romagnan, 2016), vulnerability to climate change of aquatic insects (Conti, Schmidt-Kloiber, Grenouillet, & Graf, 2013) and interactions across trophic levels (Colina, Calliari, Carballo, & Kruk, 2016). Another trait that transcends multiple functions is the motility, such as swimming speed and pattern, which directly influences encounters with both prey and predators

(Visser, 2007). These two important traits together determine the Reynold's number the organisms experience, which ultimately shapes their behaviors and natural history (Dusenbery, 2009).

Measurement of traits is typically done by sampling these small aquatic organisms using towed nets, pumps and traps, and then examining the samples in the laboratory (Suthers & Rissik, 2009). Automated digital image analysis, such as the ZooScan system (Gorsky et al., 2010) and the video-based analysis system (Yu et al., 2019), has greatly facilitated the processing of field samples and enabled investigations of zooplankton traits in many studies (Marcolin, Schultes, Jackson, & Lopes, 2013; Ohman & Romagnan, 2016). However, traditional field sampling requires high financial cost and is labor-intensive, so it often suffers from low temporal resolution and limited spatial coverage (Orenstein et al., 2020). Field sampling also excludes certain types of organisms, such as strong swimmers (Fleminger & Clutter, 1965) and delicate zooplankton (Brownlee, Olson, & Sosik, 2016). Certain aquatic invertebrates can also be difficult to keep alive. In addition, the organisms can behave differently in the lab setting so that behaviors, such as swimming pattern, cannot be fully replicated, making laboratory studies of motility difficult or impossible (Clark & Hermans, 2009).

An emerging alternative is to use optical-based instruments that enable automated and less invasive *in situ* observations. Several underwater systems have been developed, including the Imaging FlowCytobot, the In Situ Ichthyoplankton Imaging System, the Underwater Vision Profiler, the ZOOPS-O^2, the Zooglider, the In situ Plankton Assemblage eXplorer, and the Scripps Plankton Cameras (Olson & Sosik, 2007; Cowen & Guigand, 2008; Picheral et al., 2010; Briseño-Avena, Roberts, Franks, & Jaffe, 2015; Ohman et al., 2019; Lertvilai, 2020; Orenstein et al., 2020). These underwater instruments have been deployed in various environments and have

produced high quality *in situ* data that provide many insights into the aquatic ecology (Lombard

et al., 2019). Despite their utilities, these optical instruments are not designed to directly estimate

traits and are often equipped with a camera that provides a single view of an organism.

Particularly, for free-space imaging, which is the least invasive observation technique, an

organism can orient in any arbitrary angle with respect to the image sensor, so the size on the

image can be biased from the 3D to 2D projection. This projection bias from the arbitrary

orientation is even more pronounced in aquatic invertebrates compared to smaller organisms,

such as phytoplankton, because they generally lack the spherical symmetry that reduces the bias

(Vandromme et al., 2012).

A combination of optical and acoustic systems can facilitate *in situ* trait measurements.

An acoustic system is capable of 3D localization, which can be used to observe natural

behaviors, such as the depth keeping in zooplankton (Genin, Jaffe, Reef, Richter, & Franks,

2005). When combining with an optical instrument that helps identify organisms, the system can

be used in trait-based approaches. For examples, the OASIS system (Robertis, Jaffe, & Ohman,

2000) could identify size-dependent timing of vertical migration in zooplankton, and the

ZOOPS-O2 (Briseño-Avena et al., 2015) could measure orientation and acoustic reflectivity of

individual zooplankter.

Another alternative for trait measurements is underwater holography, which can be used

to obtain 3D spatial information from the reconstruction of holograms. Several underwater

holographic systems have been developed for *in situ* studies of zooplankton (Katz, Donaghay,

Zhang, King, & Russell, 1999; Malkiel, Sheng, & Katz, 2006; H. Sun et al., 2008). However, the

holographic reconstruction process can be data-intensive and requires advanced processing

capability (Nayak, Malkiel, McFarland, Twardowski, & Sullivan, 2021). The use of coherent

light source also makes holographic systems more suitable for characterizing very small targets, such as particles and phytoplankton, compared to aquatic invertebrates, especially when identifications are required.

Despite the success of previous underwater systems, a simpler system that can also provide 3D measurements of small aquatic invertebrates would be a great advantage to aquatic research. To address this need, we have developed an underwater stereoscopic imaging system that can perform 3D measurements of aquatic invertebrates in the size range of 1-10mm by implementing a tilted lens approach. The system is capable of measuring important traits, including body lengths and swimming speed, of the organisms in this size range in an ecologically relevant context. This article presents the configuration of the instrument, laboratory testing to validate its performance, and a field study where we observed the body length and swimming speed of aquatic insects in a saltmarsh.

2. Materials and method

2.1 Stereoscopic system with the tilted lenses

Stereoscopic vision systems are utilized in many underwater ecological studies to perform 3D observations, such as fish sizing (Muñoz-Benavent et al., 2018) and seagrass survey (Díaz-Gil et al., 2017). These systems are often equipped with regular cameras that have focal planes parallel to both the lens planes and the camera sensors. This simple stereoscopic setup works well for applications where a low magnification is sufficient because the vision system will have a relatively large field of view (FOV) and also a thick depth of field (DOF) (see Steger, 2016 for a review of the relationship between the magnification, the FOV and the DOF of a camera). However, imaging small aquatic invertebrates in the millimeter range requires a high magnification that results in both a small FOV and a thin DOF. In this case, a typical

stereoscopic setup where two cameras are in parallel (Fig 3.1.a) will result in a small or even non overlapping FOV. If the two cameras are in a converging setup where they are pointing toward one another (Fig 3.1.b), then the thin DOFs will result in small shared DOF.
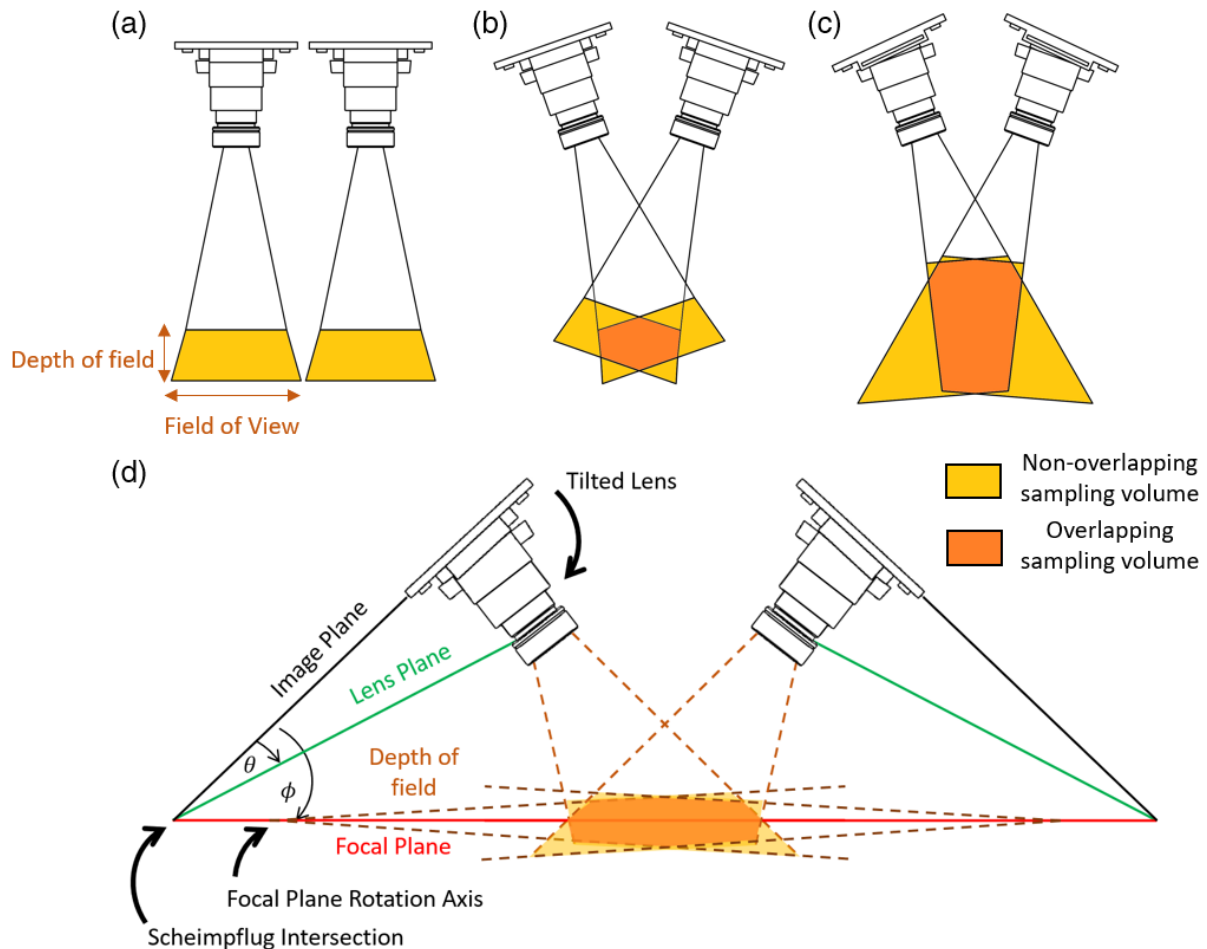
Figure 3.1: Configurations for stereo camera systems. (a) A typical stereo setup with two cameras in parallel. (b) A converging setup where two cameras are pointing toward one another. (c) A stereo setup that implements the Scheimpflug principle by tilting the lenses relative to the image sensors (d) A detailed view of the stereo setup with tilted lens outlining the location of important geometric parameters. Note that (a)-(c) are drawn to scale according to camera parameters and stereo extrinsic parameters shown in Section 2.2. (d) is not drawn to scale, and the tilt angles are exaggerated to emphasize geometry of the optics (see Fig S1.b for the Scheimpflug geometry that is drawn to scale).

For a system with high magnification, this limitation of small overlapping FOV and DOF can be alleviated by tilting the lens with respect to the camera sensor, a method often referred to as the Scheimpflug principle (Steger, 2016). When the lens is tilted, the focal plane of the system is also tilted such that the focal plane, the lens plane and the image plane are concurrent at a

point called the Scheimpflug intersection (Fig 3.1.d). Using a thin lens model, the object distance u, the image distance v and the focal length of the lens f follow the lens law:

$$\frac{1}{u} + \frac{1}{v} = \frac{1}{f} \qquad (1)$$

For a simple camera system that is focused close to the lens, the thickness of the DOF T on one side of the focal plane can be approximated as (Fig S1.a)

$$T = \frac{cN(1+m)}{m^2}, \qquad (2)$$

where N is the f-number of the lens, c is the diameter of the circle of confusion and $m = \frac{v}{u}$ is the magnification (Allen & Triantaphillidou, 2011).

When the lens is tilted at an angle of θ with respect to the image sensor, the object and the image distance along the line perpendicular to the image plane (Fig S3.1.b) become

$$u' = \frac{u}{\cos\theta} \qquad (3)$$

and

$$v' = \frac{v}{\cos\theta}, \qquad (4)$$

respectively. The angle between the image plane and the focal plane ϕ can then be calculated (Steger, 2016) as

$$\phi = \arctan\frac{v'}{v'\cos\theta - f}\sin\theta \qquad (5)$$

and, equivalently,

$$\phi = \arctan\frac{u'}{f}\sin\theta \qquad (6)$$

In this case, the DOF of each camera will no longer extend between parallel planes on both sides of the focal plane (Fig. 3.1.a and 3.1.b), but the DOF will become wedge shaped as shown in Fig

3.1.c and 3.1.d. The DOF is shallower at points closer to the focal plane rotation axis and expands at points that are further away. The depth of field on each side of the focal plane along the line perpendicular to the image plane (Fig S3.1) can be calculated as

$$T = \frac{Nc}{f}\left(\frac{1}{\tan\theta} - \frac{1}{\tan\phi}\right)u'.$$

(7)

When the tilted lens is positioned to image further away from the focal plane rotation axis, the method can result in a DOF that is larger than a traditional setup with the same lens setup.

When designing a stereoscopic system with tilted lenses, the lens and the object distance should be chosen first to provide appropriate FOV and magnification according to Equation 1. Then, Equations 3 to 6 can be used to calculate the tilt angle and the position of the two cameras according to other limitations of the system, such as housing size and illumination.

It should be noted that the main goal of tilting lenses is to maximize the shared sampling volume of the two cameras in the stereoscopic system with high magnification. This method does not affect the trade-offs between FOV, DOF and magnification, so the high magnification system will still have relatively small FOV and shallow DOF.

2.2 Instrument Description

The underwater camera system used in this study is based on the In Situ Plankton Assemblage eXplorer (IPAX) system (Lertvilai, 2020), which is a low-cost system operated on a Raspberry Pi environment (Fig 3.3.a). However, instead of having only one camera, this stereoscopic system is equipped with two cameras that implement the Scheimpflug principle. The stereo cameras are based on Sony IMX477 sensors and are synchronized by an off-the-shelf synchronization circuit (Arducam, China). Each camera is equipped with an M12 lens with a focal length of 12 mm and an f-number of f/2 (Edmund Optics, California), and the lens is positioned such that the focal plane is 80 mm away from the front of the lens, resulting in a field

of view of 35 mm x 20 mm. The lenses are tilted with respect to the image sensor by inserting a

3D-printed standoff with the tilt angle $\theta = 3.0°$ (Fig 3.3.b). This tilt results in the expected angle

between the image plane and the focal plane of $\phi = 19.3°$, according to Equation (5).

The system is illuminated by a ring light of 12 CREE XQE LEDs (Wolfspeed, North

Carolina). Each LED is individually collimated by a small lens, and the light from all LEDs is

then focused by an acrylic Fresnel lens onto the imaging volume, which is approximately 50 mm

away from the front acrylic viewport of the instrument (Fig 3.2). The focusing from the Fresnel

lens increases the light intensity inside the imaging volume while reducing the stray light outside

of the imaging volume. This configuration also increases the contrast of images because objects

outside the imaging volume are less likely to be illuminated. In contrast to a traditional glass

lens, the acrylic Fresnel lens can be drilled in the middle to allow the cameras to image without

obstruction (Fig 3.3.c), which allows the entire imaging system to fit inside a compact

waterproof housing.
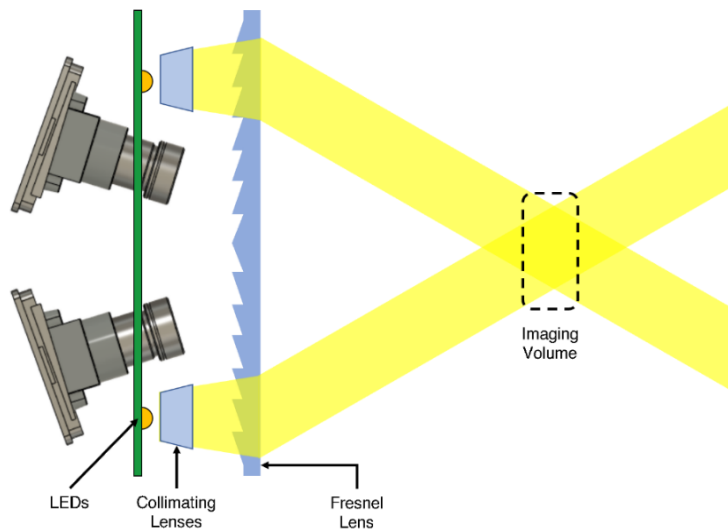
Figure 3.2: The schematic of the illumination system. The light from each LED is collimated by a small
collimating lens, and the light from all 12 LEDs on the ring is then focused by a Fresnel lens to the
imaging volume. See Fig S6 inset for the illumination pattern in the field experiment.

The main computer inside the instrument is a Raspberry Pi model 4B with 4GB RAM.

This powerful Raspberry Pi computer is needed to ensure that the instrument can utilize the cameras and the synchronization board properly. The instrument is equipped with a 195Wh lithium-ion battery pack, which can last up to approximately 26 hours of continuous image acquisition. All components are housed in an off-the-shelf pressure housing (Bluerobotics, California) that has a diameter of 100 mm and is 380 mm in length (Fig 3.3.a). The detailed specification of the instrument is provided in Supplementary Table S1, and the internal parts of the instrument are shown in Fig S3.2.
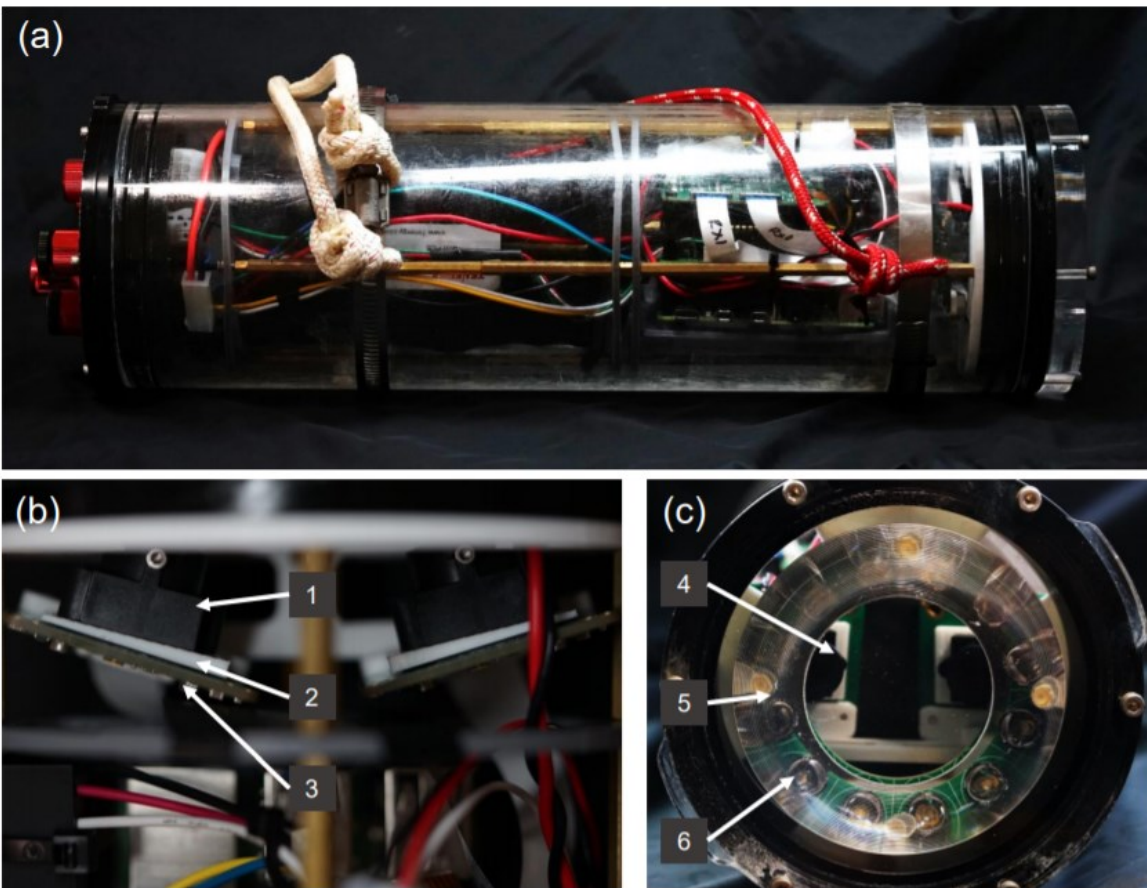
Figure 3.3: (a) The fully assembled instrument inside a waterproof housing. (b) The implementation of the Scheimpflug optics on the stereo cameras using 3D-printed standoffs. (1) The M12 lens. (2) The 3D-printed part that tilts the lens relative to the image sensor. (3) The image sensor. (c) The illumination. (4) Two cameras that form the stereoscopic setup. (5) The Fresnel lens that focuses the light from all LEDs into the imaging volume. (6) The LED ring with 12 LEDs that are individually collimated by small collimating lenses.

2.3 Instrument Calibration

The stereoscopic system was calibrated to determine the intrinsic parameters and distortion coefficients of each camera as well as the extrinsic parameters relating the position of the two cameras (Wehkamp & Fischer, 2014). The intrinsic parameters and the distortion coefficients are used to undistort the images that is due to any distortions from optics. The extrinsic parameters are used in the triangulation step to find 3D positions using corresponding points from both cameras (Bradski & Kaehler, 2008). A Scheimpflug camera typically requires a complex camera model that incorporates the tilt angles in the calibration (C. Sun, Liu, Jia, & Chen, 2018). However, when the tilt angle is small ($\leq 6°$), the calibration method of a regular camera can compensate for the lens tilting (Legarda, Izaguirre, Arana, & Iturrospe, 2013). Since the tilt angle of the system is $\theta = 3°$, the Zhang method (Zhang, 1999) for a regular stereo setup is used for this study.

A checkerboard pattern consisting of 2 mm x 2 mm squares with a total of 6 x 9 internal corners was used to calibrate the system (Fig S3.3). The instrument was fully submersed in a tank filled with saltwater, and the checkerboard pattern was placed at the bottom of the tank. This calibration was done entirely underwater to ensure that there was no bias from different media (Bianco, Ekvall, Bäckman, & Hansson, 2013). The instrument captured 28 images of the checkerboard pattern in various positions, which are used to perform the stereo calibration. This stereo calibration and all subsequent data analyses were done with programs written in MATLAB 2020b, and the calibration was performed with the MATLAB Stereo Calibration application (Fetić Azra, Jurić Davor, 2012).

After obtaining the extrinsic parameters for the stereo setup from the calibration, Equations (2) and (7) were used to calculate the depth of field of each camera with and without

the implementation of the Scheimpflug principle. A circle of confusion with a diameter of 0.1 mm was used in the DOF calculation. The overlapping sampling volumes of the two cameras were then calculated and compared between different stereo setups as shown in Fig 1.(a)-(c). The accuracy of the camera parameters was also validated by using them to perform 3D triangulation to measure the known widths of patterns on a USAF1951 target (Fig S3.4). With the target was placed at the bottom of the test tank the system captured 10 images of the target from various positions while keeping the target in focus. The widths of patterns in groups 0 and 1 were computed by triangulating the end points of each pattern and then compared to the known widths.

2.4 Field Deployment

The instrument was deployed in a water channel in the Kendall-Frost saltmarsh, San Diego, California in July 2021 to observe *Trichocorixa californica*, a species of aquatic insects commonly referred to as "water boatmen", which are the most abundant invertebrates in the water column at the study site (Fig S3.5). The system was mounted on a speed rail structure to position it approximately 30 cm above the bottom of the channel and 50 cm below the water surface. This elevation from the bottom was necessary to minimize imaging obstruction by mud particles. The imaging system was programmed to capture 60 s videos with a resolution of 1920 x 1080 pixels at 30 frames per second. A total of 14 videos were recorded with a 10 min interval between two consecutive videos. The entire deployment was done during a high tide extreme to minimize ambient flow in the channel as well as ensuring that the instrument was fully submerged at approximately the same depth throughout the duration.

2.5 Image Processing

An image processing routine was applied to raw images from the field deployment to

segment aquatic organisms and ambient particles. The images of organisms were used to track the movement and the size while the images of ambient particles were used to estimate the ambient flow velocity. The raw 8-bit color image from the stereoscopic system (Fig 3.4.a) was first separated into two views and converted to grayscale. The grayscale images were then undistorted using the camera parameters obtained from calibration (Fig 3.4.b).

To segment the aquatic insects, an edge detection algorithm similar to the process in the Scripps Plankton Camera system (Orenstein et al., 2020) was used. A Sobel edge detector was applied to the undistorted images to detect the outlines of all organisms, and these outlines were morphologically dilated by three structuring elements: a vertical line, a horizontal line and a circle. This dilation step ensured that detected edge of an organism is connected, forming only one binary blob. A region filling algorithm was then applied to fully close the contours, and the mask was further morphologically opened with a circle to remove appendages from organisms. Finally, a size filtering algorithm was applied such that only detected blobs with area larger than a threshold of 1000 pixels were kept. These steps resulted in a mask of the body of each organism without their appendages (Fig 3.4.c). For each organism, an ellipse was fitted to the binary mask to find the centroid and the end points of the major axis, which represented the body length of the organism (Fig 3.4.d) (Vandromme et al., 2012). Visual inspection was done on sample images to ensure that the algorithm works as intended. The pseudo-code for this image processing is provided in the supplementary material.

To segment particles from raw images, a global thresholding algorithm was applied to the undistorted images to generate a binary mask of all pixels that were brighter than a threshold of 1. Then, a size filtering algorithm was applied to all the binary blobs to only save blobs that have areas within the range of 5 to 50 pixels, which was an appropriate size of ambient particles that

were approximately larger than 100 μm in diameter.
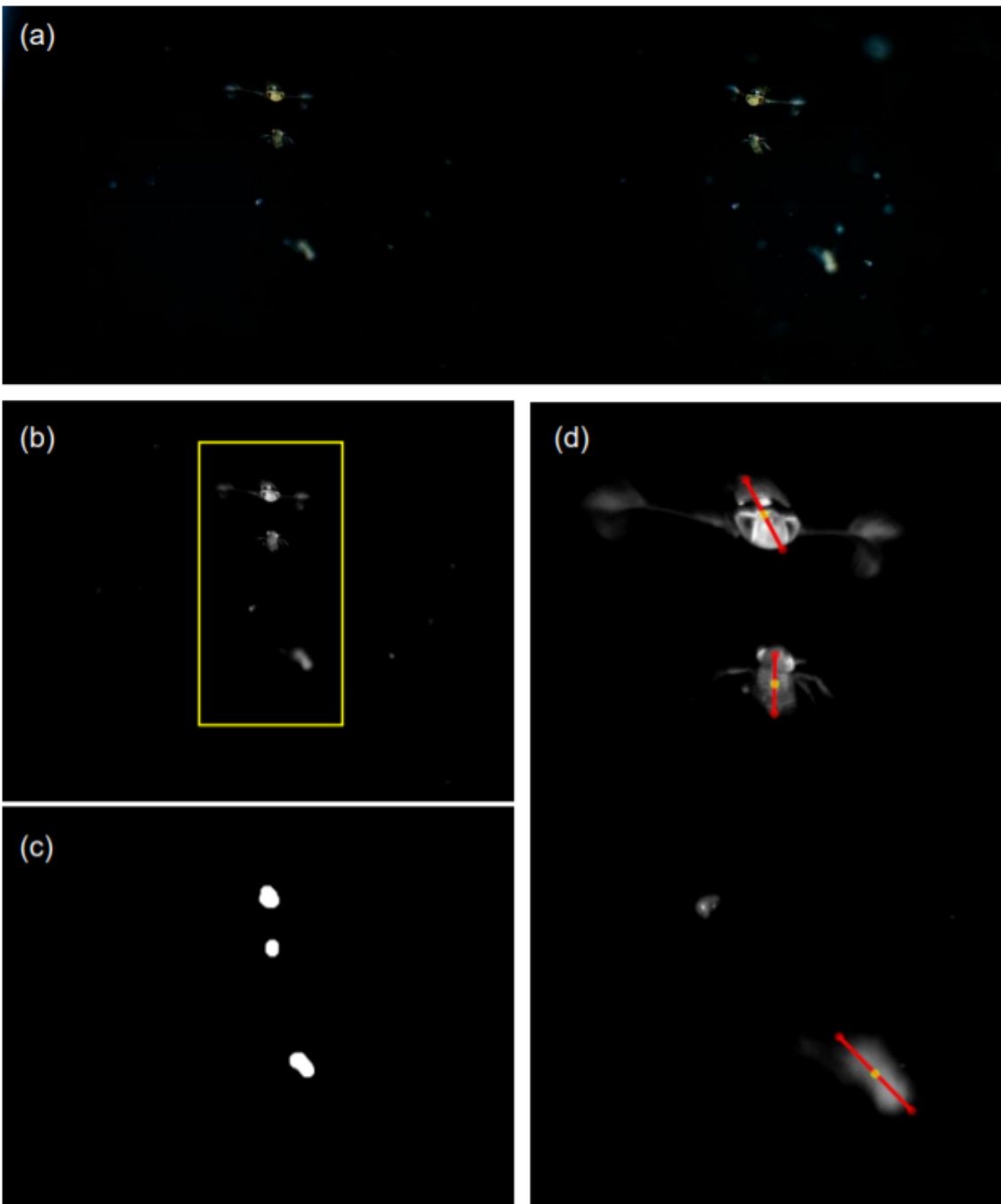
Figure 3.4: Image processing steps. (a) A raw color image from the stereo system containing views from both image sensors. (b) The image from the left view is converted to grayscale and undistorted using the camera parameters from the calibration. (c) The binary mask of organisms obtained by applying an edge detector and morphological processing to (b). (d) The final length measurement of each organism in (b) inside the yellow region. The red line indicates the major axis, and the yellow dot indicates the centroid of each organism.

2.6 3D Tracking

For each video frame, the centroids of all segmented organisms were used to perform stereo correspondence. Using the extrinsic camera parameters from the stereo calibration, a centroid from the left view was triangulated with all centroids in the right view to obtain a 3D position of each pair. The 3D positions were then reprojected back to both left and right views and the reprojection errors were calculated. The centroid on the right view with the smallest reprojection error that did not exceed 10 pixels was considered the correspondence to the centroid on the left view. If no centroid on the right yielded a reprojection error below the threshold, then the centroid on the left had no correspondence.

The correspondence algorithm was repeated on the next frame, and a global nearest neighbor algorithm (Reid, 1979) was used to track the 3D positions of organisms between two consecutive frames. A centroid in the current frame was matched with the centroid in the next frame that was closest to it and was not farther than a threshold of 8 mm in the object space. If no centroid in the next frame was found within the distance threshold, then the track was considered broken, and the track was considered ended when it was broken for more than 4 consecutive frames. The ambient particles were also tracked with the same algorithm to determine the ambient flow velocity, but the distance threshold was reduced to 3 mm.

2.7 Data Analysis

For each 60-second video, the instantaneous speed of an ambient particle was calculated by dividing the distance it traveled between two consecutive frames by the time between frames, which was 33.3 ms for the frame rate of 30 frames per second. During the time of the deployment, the ambient flow was slow and approximately unidirectional, so the mean flow velocity of all particles in the video was used to estimate the ambient flow velocity.

38

For the aquatic insects, each individual track was manually checked to ensure that the tracked object was indeed a water boatman, and only tracks that were longer than 5 frames were considered in further analyses. The instantaneous velocity of each insect was compensated by subtracting the estimated ambient flow velocity from particle tracking, and the mean value of all instantaneous speeds in a track was used for further analyses. The body length of each insect was also calculated by triangulating the end points of the major axis (Fig 3.4.d) to find the 3D positions of the end of its body and then computing the distance between the two end points. The mean value of the body length in every frame in the track was used as the mean body length of the individual insect.

The data from all tracked insects in the 14 videos were used to determine the relationship between the swimming speed and the body length of water boatmen. A linear regression was performed on the logarithmic scale of both swimming speed and body length to determine the relationship. Additionally, the Reynold's number (Re) of each insect was calculated using the equation:

$$Re = \frac{\rho u L}{\mu} \, , \tag{6}$$

where ρ is the density of saltwater, u is the mean speed of each insect, L is the body length of the insect, and μ is the dynamic viscosity of saltwater.

3. Results
3.1 Instrument calibration

The stereo calibration yields camera parameters that result in an overall mean reprojection error of the checkerboard corners of 0.64 pixels (Fig S3.6.a). The extrinsic parameters show that the view angle between the two cameras is 44°, and the baseline distance is 43.7 mm (Fig S3.6.b). The depth of field of the simple camera is calculated to be 15.1 mm, while

that of the camera with the Scheimpflug setup is 35.5 mm (Fig S3.1). This result means that the

parallel stereo setup (Fig 1.a) yields no overlapping sampling volume at all because the FOV is

smaller than the size of the camera board. Using the extrinsic parameters, the converging stereo

setup (Fig 3.1.b) results in an overlapping sampling volume of 57.5% of the sampling volume of

one camera, which is equivalent to 5.8 cm^3 total sampling volume. The tilted lens setup (Fig 1.c),

on the other hand, results in an overlapping volume of 67.8%, which is 18.2 cm^3 sampling

volume, an increase of 3.1 times compared to a converging setup.

The result from using the system to measure the width of Group 0 and 1 of a USAF1951

resolution target is shown in Fig 3.5. Within the range of 0.1 to 0.5 mm, the system can

accurately measure the length with a percent error of 6%.
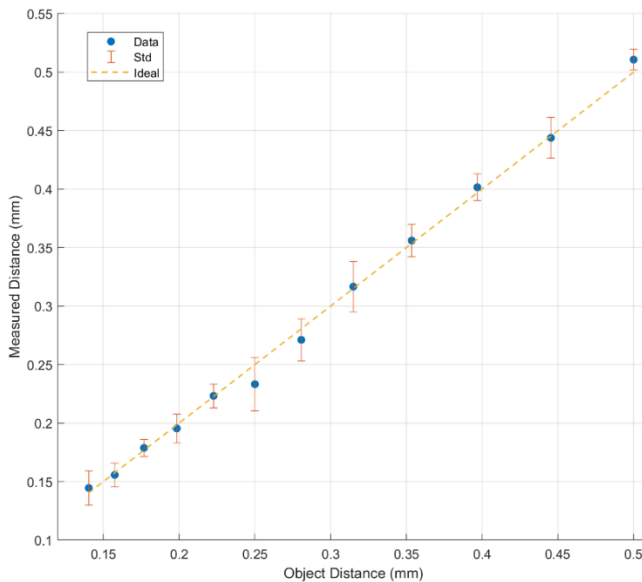
Figure 3.5: The comparison of the length of USAF1951 target Group 0 and 1 between the actual object distance and the length measured by the stereo system. The error bar indicates the standard deviations.

3.2 Field deployment and tracking

The system was deployed in the water channel and captured videos with suitable image

quality for further analyses (Supplementary Video S1). The density of water boatmen was 9.7

individuals per liter, which was sufficiently low such that the global nearest neighbor tracking worked well to track each individual insect that was clearly seen by both cameras (Fig. 3.6.a and Supplementary Video S2). From the 14 videos, a total of 482 water boatmen were tracked and verified with an average of 34.36 insects per 60-second video. The average track length was 0.53 seconds (15.87 frames), and the longest track was 6.6 seconds (198 frames).

For particles, the density of trackable particles was 0.36 particles per ml. An average of 214.36 particles were tracked in each video, which is equivalent to 2.35 tracked particles per frame. The average track length for the particles was 0.67 seconds (17.06 frames), and the longest track was 5.23 seconds (158 frames). The mean speed of tracked particles in each video ranges from 6.1 to 8.2 mm/s (Fig. S3.7). For each video, all particles are moving in approximately the same speed and direction at low speed, so the uniform flow condition can be assumed (Fig. 3.6.b and Fig. S3.8), and the mean velocity of all particles are used to compensate for the movement of insects.
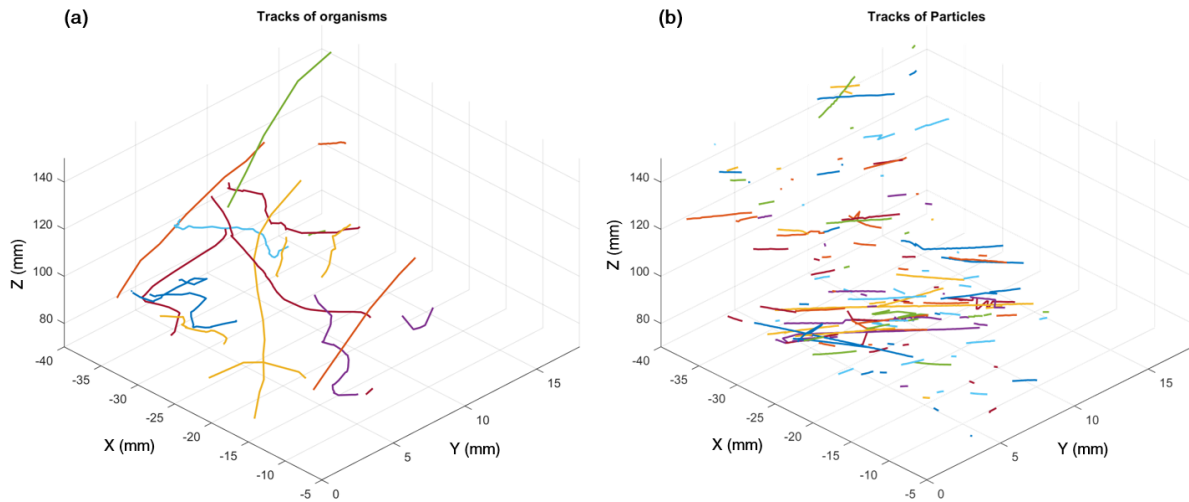
Figure 3.6: (a) The 3D tracks of 20 individual water boatman from a 60-second video. (b) The 3D tracks of ambient particles in the same video. The origin of the 3D coordinates (0,0,0) is located at the center of the left camera of the system.

3.3 Swimming speed and body length of water boatmen

The relationship between the swimming speed and the body length of the water boatmen (Fig. 3.7a) shows a linear relationship in the log-log scale with a slope of 1.64 ± 0.15 ($R^2 = 0.45, p < 0.001$). The fitted equation can be rewritten in the exponential form,

$$u = kL^\alpha , \qquad (6)$$

where u is the swimming speed, L the body length, and k and α are constants from the curve fitting. In this exponential form, the exponent is $\alpha = 0.81 \pm 0.07$. The relationship between Reynold's number and the body length of the aquatic insects is shown in Fig. 3.7b. The range of the Reynold's number spans three order of magnitudes from 10^0 to 10^3.
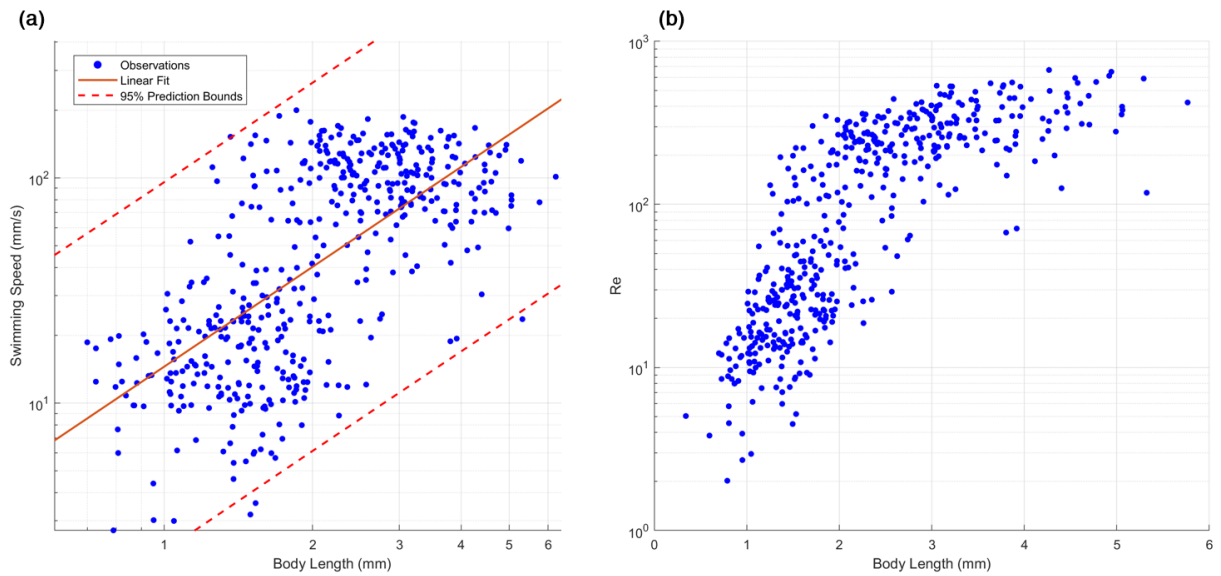
Figure 3.7: (a) The relationship between the body length and the mean swimming speed of water boatmen (N=482 tracks). The solid line indicates linear regression estimates ($R^2 = 0.45, p < 0.001$), and the dashed lines indicate 95% prediction intervals. (b) The relationship between the body length and the Reynold's number of water boatmen.

4.   Discussion

4.1 *In situ* three-dimensional measurements

The results from the laboratory calibration and validation indicate that the stereoscopic system is suitable for 3D measurement of small aquatic invertebrates in the size range of 1-10

mm. The implemented Scheimpflug setup increases the overall sampling volume of the stereoscopic system by 3.1 times compared to the setup with the same lens and sensors and the same extrinsic parameters without tilting the lenses. This increase in the sampling volume allows the system to image more organisms and to track them in 3D space for a longer period. Additionally, the camera parameters from the calibration enables the system to measure length of targets on the USAF1951 resolution chart within 6% error. However, this lab validation is done on an ideal target with known corresponding points at the edges of each line. In field applications, the end points and the centroid of an organism cannot be resolved with the same resolution, so the accuracy will be lower depending on the certainty of stereo correspondence.

Our field results demonstrate that the dual-view system is capable of resolving 3D traits of aquatic invertebrates *in situ*. With the implementation of the Scheimpflug principle, the system can image the same organisms from two different views that can then be used to perform triangulation to measure both the body length and the position in 3D space. For free space *in situ* imaging, even though the size measurement can be estimated with a single-view system given a calibration to correct for the bias, this measurement can only be corrected on the statistics of an entire group of organisms, such as the mean body length, and not on the individual basis (Merz et al., 2021). Using our stereoscopic system, the body length of each individual organism can be measured independently. As a result, the dual-view system offers a new capability to perform size measurement of small aquatic invertebrates *in situ* that cannot be done by other existing underwater systems.

For velocity measurements, the system can be used to track position of water boatmen to find their velocity between frames. Additionally, we isolate the velocity of the insects from the ambient flow by tracking particles to obtain the flow velocity. However, the system is not

designed to perform particle imaging and only a few particles can be imaged and tracked

between frames. As a result, we can only use the mean flow velocity for each video to perform

the ambient flow compensation. This approach works well in our field study because the

deployment was done during the tide extreme where ambient flow in the saltmarsh was

sufficiently slow and unidirectional. However, if the ambient flow is faster or turbulent, other

more sophisticated flow meters might be necessary. For instance, an acoustic doppler

velocimeter or a separate imaging platform that is designed to perform particle image

velocimetry or particle tracking velocimetry (Lertvilai, Roberts, & Jaffe, 2021) should be

deployed at the same time as the stereoscopic imaging system.

In this field deployment, we achieved good tracking results with a relatively simple

global nearest neighbor algorithm because the densities of both the insects and the particles that

could be imaged were sufficiently low such that the correspondence between two views and the

tracking between frames were straightforward. However, if the stereoscopic system is deployed

in an environment with higher density of organisms, then the simple algorithm might not be able

to correspond and track organisms, and a more sophisticated 3D tracking is needed (e.g. Fuchs,

Hain, & Kähler, 2017). Adding more cameras to the system will also improve the accuracy of

correspondence between views, but the trade-off is a more complicated optical setup and a larger

size of the overall instrument (e.g. Adhikari, Gemmell, Hallberg, Longmire, & Buskey, 2015).

4.2 Relationship of swimming speed and body size of water boatmen

For the water boatmen, our field result shows that the relationship between the body

length (L) and the mean swimming speed (u) exhibits a linear relationship in the log-log space as

$u \propto L^{0.68}$ (Fig. 3.7a). For swimming organisms, the mass (M) scales with the body length

according to the approximation $M \propto (2L)^3$ (Videler & Nolet, 1990), so our result can be

converted to the relationship between the mass and the swimming speed as $u \propto M^{0.23}$. This

relationship follows the trend of a wide range of motile organisms where the mass and the

movement speed exhibits a linear relationship in the log-log space (Bejan & Marden, 2006). The

optimal speed that allows the organisms to maximize travelled distance or minimize energy used

is scaled by $u \propto M^{\frac{1}{6}}$ (Heglund & Taylor, 1988; Bejan & Marden, 2006), while the maximum

sustainable speed is scaled by $u \propto M^{\frac{1}{3}}$ (Meyer-Vernet & Rospars, 2016). Our scaling exponent of

0.23 lies between these two values, signifying that the water boatmen are swimming with the

mean velocity between the optimal and the maximum speed.

Our result shows that the water boatmen experience the regime of intermediate Reynold's

numbers spanning the range of 10^0 to 10^3 (Fig. 3.7b), which agrees with previous laboratory

study of this family of aquatic insects (Ngo & McHenry, 2014). This intermediate regime

indicates that the insects utilize both viscous and inertial forces. They move by paddling their

metathoracic hindlegs, so their speed is periodic with a short burst at the start of paddling and

then slowing down as they coast. Due to the limitation of the frame rate of the system, our

instrument cannot resolve the dynamic of this movement, and our analysis only involves the

mean speed. As a result, it is possible that the insects might have a maximum instantaneous

speed at the beginning of each paddling cycle that has a scaling exponent that is closer to 1/3 as

predicted by Meyer-Vernet & Rospars, 2016.

4.3 Instrument potential and limitation

Our results demonstrate the potential of using a stereoscopic imaging system with tilted

lenses to provide ecological insights in the small scale that is relevant to many aquatic

organisms. The stereoscopic setup can help expand the utility of *in situ* imaging systems beyond

species identification and density estimation to include parameters, such as swimming speed and

size, that are important in the emerging trait-based analysis in ecology. The system is suitable for 3D tracking, which can be used to resolve movement speed of organisms, when the ambient flow is sufficiently low such that target organisms can stay in the field of view for an extended period of time, similar to our field study with the water boatmen. If a more sophisticated camera system is implemented such that higher frame rate can be achieved, then it is also possible to use the stereoscopic setup to resolve movement of main body parts, such as the hindlegs of aquatic insects, so that the dynamic of their locomotion can be understood. When the flow is high or the system is mounted on a moving platform, tracking might not be feasible, but the system is still suitable for size measurements. The stereoscopic setup can be implemented on a monitoring platform so that the size of individual organism can be measured.

The stereoscopic setup with the Scheimpflug principle is also relatively straightforward to implement. The setup only needs a stereo-calibration to obtain camera parameters that are used for undistortion and triangulation. When the tilt angle is small ($\leq 6°$), a regular calibration that is available through open-source software, such as OpenCV (Bradski & Kaehler, 2008), or readily available toolbox, such as the MATLAB Stereo Calibration application (Fetić Azra, Jurić Davor, 2012), can be used. Here we also demonstrated that the optical setup can be implemented on a low-cost platform that utilizes the Raspberry Pi ecosystem and off-the-shelf parts, including pressure housing, cameras and synchronization circuits. The system can be modified to suit many ecological studies by determining the required field of view and the resolution that are appropriate for the target organisms and, then, selecting suitable lenses, imaging sensor and lens tilt angle that can achieve these desired parameters. However, it should be noted that the imaging system is subject to the trade-off between resolution, field of view and depth of field where higher resolution requires smaller field of view and shallower depth of field, effectively smaller

sampling volume (Orenstein et al., 2020).

5.   Conclusion

The results reported here highlight the application of the Scheimpflug principle to construct a stereoscopic imaging system that is capable of resolving 3D measurements of aquatic invertebrates *in situ*. Our results demonstrate that the optical setup can be used to measure the body length and the swimming speed of small aquatic organisms in an ecologically relevant context. This work expands the capability of underwater imaging systems to measure important traits of individual aquatic invertebrate in its natural environment and offers an important step towards trait-based approach to aquatic ecology.

Chapter 3, in part, is currently under review in *Methods in Ecology and Evolution*. Lertvilai, Pichaya; Jaffe, Jules. The dissertation author was the primary investigator and author of this paper.

Reference

Adhikari, D., Gemmell, B. J., Hallberg, M. P., Longmire, E. K., & Buskey, E. J. (2015). Simultaneous measurement of 3D zooplankton trajectories and surrounding fluid velocity field in complex flows. *Journal of Experimental Biology*, *218*(22), 3534–3540. doi:10.1242/JEB.121707

Allen, E., & Triantaphillidou, S. (2011). The manual of photography, 585. Retrieved from http://books.google.com/books?hl=en&lr=&id=IfWivY3mIgAC&oi=fnd&pg=PP2&dq=Th e+Manual+of+Photography&ots=7jcp6608Pb&sig=G5Cl9-LOjRWAfHB-xpm3KgMLrzQ

Bejan, A., & Marden, J. H. (2006). Unifying constructal theory for scale effects in running, swimming and flying. *Journal of Experimental Biology*, *209*(2), 238–248. doi:10.1242/JEB.01974

Bianco, G., Ekvall, M. T., Bäckman, J., & Hansson, L.-A. (2013). Plankton 3D tracking: the importance of camera calibration in stereo computer vision systems. *Limnology and Oceanography: Methods*, *11*(5), 278–286. doi:10.4319/lom.2013.11.278

Bradski, G., & Kaehler, A. (2008). *Learning OpenCV: Computer Vision with the OpenCV Library*. O'Reilly.

Briseño-Avena, C., Roberts, P. L. D., Franks, P. J. S., & Jaffe, J. S. (2015). ZOOPS- O2: A broadband echosounder with coordinated stereo optical imaging for observing plankton in situ. *Methods in Oceanography*, *12*, 36–54. doi:10.1016/j.mio.2015.07.001

Brownlee, E., Olson, R., & Sosik, H. (2016). Microzooplankton community structure investigated with imaging flow cytometry and automated live-cell staining. *Marine Ecology Progress Series*, *550*, 65–81. doi:10.3354/meps11687

Clark, R. B., & Hermans, C. O. (2009). Kinetics of smimming in some smooth-bodied polychaetes. *Journal of Zoology*, *178*(2), 147–159. doi:10.1111/j.1469-7998.1976.tb06004.x

Colina, M., Calliari, D., Carballo, C., & Kruk, C. (2016). A trait-based approach to summarize zooplankton–phytoplankton interactions in freshwaters. *Hydrobiologia*, *767*(1), 221–233. doi:10.1007/s10750-015-2503-y

Conti, L., Schmidt-Kloiber, A., Grenouillet, G., & Graf, W. (2013). A trait-based approach to assess the vulnerability of European aquatic insects to climate change. *Hydrobiologia 2013 721:1*, *721*(1), 297–315. doi:10.1007/S10750-013-1690-7

Cowen, R. K., & Guigand, C. M. (2008). In situ ichthyoplankton imaging system (ISIIS): System design and preliminary results. *Limnology and Oceanography: Methods*, *6*(2), 126–132. doi:10.4319/lom.2008.6.126

Díaz-Gil, C., Smee, S. L., Cotgrove, L., Follana-Berná, G., Hinz, H., Marti-Puig, P., … Catalán, I. A. (2017). Using stereoscopic video cameras to evaluate seagrass meadows nursery function in the Mediterranean. *Marine Biology 2017 164:6*, *164*(6), 1–11.

doi:10.1007/S00227-017-3169-Y

Dusenbery, D. B. (2009). Living at micro scale : the unexpected physics of being small, 416.

Fetić Azra, Jurić Davor, O. D. (2012). The procedure of a camera calibration using Camera Calibration Toolbox for MATLAB | IEEE Conference Publication | IEEE Xplore. *The Procedure of a Camera Calibration Using Camera Calibration Toolbox for MATLAB*, 1752–1757. Retrieved from https://ieeexplore.ieee.org/abstract/document/6240932

Fleminger, A., & Clutter, R. I. (1965). Avoidance of towed nets by zooplankton. *Limnology and Oceanography*, *10*(1), 96–104. doi:10.4319/lo.1965.10.1.0096

Fuchs, T., Hain, R., & Kähler, C. J. (2017). Non-iterative double-frame 2D/3D particle tracking velocimetry. *Experiments in Fluids*, *58*(9), 119. doi:10.1007/s00348-017-2404-0

Genin, A., Jaffe, J. S., Reef, R., Richter, C., & Franks, P. J. S. (2005). Swimming Against the Flow: A Mechanism of Zooplankton Aggregation. *Science*, *308*(5723), 860–862. doi:10.1126/SCIENCE.1107834

Gorsky, G., Ohman, M. D., Picheral, M., Gasparini, S., Stemmann, L., Romagnan, J.-B., … Prejger, F. (2010). Digital zooplankton image analysis using the ZooScan integrated system. *Journal of Plankton Research*, *32*(3), 285–303. doi:10.1093/plankt/fbp124

Heglund, N. C., & Taylor, C. R. (1988). Speed, stride frequency and energy cost per stride: how do they change with body size and gait? *Journal of Experimental Biology*, *138*(1), 301–318. doi:10.1242/JEB.138.1.301

Katz, J., Donaghay, P. L., Zhang, J., King, S., & Russell, K. (1999). Submersible holocamera for detection of particle characteristics and motions in the ocean. *Deep-Sea Research Part I: Oceanographic Research Papers*, *46*(8), 1455–1481. doi:10.1016/S0967-0637(99)00011-4

Kiørboe, T. (2019). *A Mechanistic Approach to Plankton Ecology. A Mechanistic Approach to Plankton Ecology*. Princeton University Press. doi:10.1515/9780691190310

Kiørboe, T., Visser, A., Andersen, K. H., & Browman, H. (2018). A trait-based approach to ocean ecology. *ICES Journal of Marine Science*, *75*(6), 1849–1863. doi:10.1093/icesjms/fsy090

Legarda, A., Izaguirre, A., Arana, N., & Iturrospe, A. (2013). Comparison and error analysis of the standard pin-hole and Scheimpflug camera calibration models. *Informal Proceedings of the 11th International Workshop of Electronics, Control, Measurement, Signals and Their Application to Mechatronics, ECMSM 2013*. doi:10.1109/ECMSM.2013.6648945

Lertvilai, P. (2020). The In situ Plankton Assemblage eXplorer (IPAX): An inexpensive underwater imaging system for zooplankton study. *Methods in Ecology and Evolution*, *11*(9), 1042–1048. doi:10.1111/2041-210X.13441

Lertvilai, P., Roberts, P. L. D., & Jaffe, J. S. (2021). In Situ Underwater Average Flow Velocity

Estimation Using a Low-Cost Video Velocimeter. *Journal of Atmospheric and Oceanic Technology*, *38*(6), 1143–1156. doi:10.1175/JTECH-D-20-0115.1

Litchman, E., & Klausmeier, C. A. (2008). Trait-Based Community Ecology of Phytoplankton. *Annual Review of Ecology, Evolution, and Systematics*, *39*(1), 615–639. doi:10.1146/annurev.ecolsys.39.110707.173549

Litchman, E., Ohman, M. D., & Kiørboe, T. (2013). Trait-based approaches to zooplankton communities. *Journal of Plankton Research*, *35*(3), 473–484. doi:10.1093/plankt/fbt019

Lombard, F., Boss, E., Waite, A. M., Uitz, J., Stemmann, L., Sosik, H. M., … Appeltans, W. (2019, April 25). Globally consistent quantitative observations of planktonic ecosystems. *Frontiers in Marine Science*. Frontiers Media S.A. doi:10.3389/fmars.2019.00196

Malkiel, E., Sheng, J., & Katz, J. (2006). Digital holographic microscope for measuring three-dimensional particle distributions and motions. *Applied Optics, Vol. 45, Issue 16, Pp. 3893-3901*, *45*(16), 3893–3901. doi:10.1364/AO.45.003893

Marcolin, C. da R., Schultes, S., Jackson, G. A., & Lopes, R. M. (2013). Plankton and seston size spectra estimated by the LOPC and ZooScan in the Abrolhos Bank ecosystem (SE Atlantic). *Continental Shelf Research*, *70*, 74–87. doi:10.1016/j.csr.2013.09.022

Merz, E., Kozakiewicz, T., Reyes, M., Ebi, C., Isles, P., Baity-Jesi, M., … Pomati, F. (2021). Underwater dual-magnification imaging for automated lake plankton monitoring. *Water Research*, *203*, 117524. doi:10.1016/J.WATRES.2021.117524

Meyer-Vernet, N., & Rospars, J.-P. (2016). Maximum relative speeds of living organisms: Why do bacteria perform as fast as ostriches? *Physical Biology*, *13*(6), 066006. doi:10.1088/1478-3975/13/6/066006

Muñoz-Benavent, P., Andreu-García, G., Valiente-González, J. M., Atienza-Vanacloig, V., Puig-Pons, V., & Espinosa, V. (2018). Automatic Bluefin Tuna sizing using a stereoscopic vision system. *ICES Journal of Marine Science*, *75*(1), 390–401. doi:10.1093/ICESJMS/FSX151

Nayak, A. R., Malkiel, E., McFarland, M. N., Twardowski, M. S., & Sullivan, J. M. (2021). A Review of Holography in the Aquatic Sciences: In situ Characterization of Particles, Plankton, and Small Scale Biophysical Interactions. *Frontiers in Marine Science*, *0*, 1256. doi:10.3389/FMARS.2020.572147

Ngo, V., & McHenry, M. J. (2014). The hydrodynamics of swimming at intermediate Reynolds numbers in the water boatman (Corixidae). *Journal of Experimental Biology*, *217*(15), 2740–2751. doi:10.1242/JEB.103895

Ohman, M. D., Davis, R. E., Sherman, J. T., Grindley, K. R., Whitmore, B. M., Nickels, C. F., & Ellen, J. S. (2019). *Zooglider:* An autonomous vehicle for optical and acoustic sensing of zooplankton. *Limnology and Oceanography: Methods*, *17*(1), 69–86. doi:10.1002/lom3.10301

Ohman, M. D., & Romagnan, J. (2016). Nonlinear effects of body size and optical attenuation on Diel Vertical Migration by zooplankton. *Limnology and Oceanography*, *61*(2), 765–770. doi:10.1002/lno.10251

Olson, R. J., & Sosik, H. M. (2007). A submersible imaging-in-flow instrument to analyze nano- and microplankton: Imaging FlowCytobot. *Limnology and Oceanography: Methods*, *5*(6), 195–203. doi:10.4319/lom.2007.5.195

Orenstein, E. C., Ratelle, D., Briseño-Avena, C., Carter, M. L., Franks, P. J. S., Jaffe, J. S., & Roberts, P. L. D. (2020). The Scripps Plankton Camera system: A framework and platform for in situ microscopy. *Limnology and Oceanography: Methods*, *18*(11), 681–695. doi:10.1002/lom3.10394

Picheral, M., Guidi, L., Stemmann, L., Karl, D. M., Iddaoud, G., & Gorsky, G. (2010). The Underwater Vision Profiler 5: An advanced instrument for high spatial resolution studies of particle size spectra and zooplankton. *Limnology and Oceanography: Methods*, *8*(9), 462–473. doi:10.4319/lom.2010.8.462

Reid, D. B. (1979). An Algorithm for Tracking Multiple Targets. *IEEE Transactions on Automatic Control*, *24*(6), 843–854. doi:10.1109/TAC.1979.1102177

Robertis, A. De, Jaffe, J. S., & Ohman, M. D. (2000). Size-dependent visual predation risk and the timing of vertical migration in zooplankton. *Limnology and Oceanography*, *45*(8), 1838–1844. doi:10.4319/LO.2000.45.8.1838

Santhanam, P., Pachiappan, P., & Begum, A. (2018). A method of collection, preservation and identification of Marine Zooplankton. In *Basic and Applied Zooplankton Biology* (pp. 1–44). Springer Singapore. doi:10.1007/978-981-10-7953-5_1

Steger, C. (2016). A Comprehensive and Versatile Camera Model for Cameras with Tilt Lenses. *International Journal of Computer Vision 2016 123:2*, *123*(2), 121–159. doi:10.1007/S11263-016-0964-8

Sun, C., Liu, H., Jia, M., & Chen, S. (2018). Review of calibration methods for scheimpflug camera. *Journal of Sensors*, *2018*. doi:10.1155/2018/3901431

Sun, H., Benzie, P. W., Burns, N., Hendry, D. C., Player, M. A., & Watson, J. (2008). Underwater digital holography for studies of marine plankton. *Philosophical Transactions of the Royal Society A: Mathematical, Physical and Engineering Sciences*, *366*(1871), 1789–1806. doi:10.1098/rsta.2007.2187

Suthers, I., & Rissik, D. (2009). Sampling methods for plankton. In *Plankton: A Guide to Their Ecology and Monitoring for Water Quality* (pp. 73–114).

Vandromme, P., Lars, S., Garcìa-Comas, C., Berline, L., Sun, X., & Gorsky, G. (2012). Assessing biases in computing size spectra of automatically classified zooplankton from imaging systems: A case study with the ZooScan integrated system. *Methods in Oceanography*, *1–2*, 3–21. doi:10.1016/j.mio.2012.06.001

Videler, J. J., & Nolet, B. A. (1990, January 1). Costs of swimming measured at optimum speed: Scale effects, differences between swimming styles, taxonomic groups and submerged and surface swimming. *Comparative Biochemistry and Physiology -- Part A: Physiology*. doi:10.1016/0300-9629(90)90155-L

Visser, A. W. (2007). Motility of zooplankton: fitness, foraging and predation. *Journal of Plankton Research*, *29*(5), 447–461. doi:10.1093/PLANKT/FBM029

Wehkamp, M., & Fischer, P. (2014). A practical guide to the use of consumer-level digital still cameras for precise stereogrammetric in situ assessments in aquatic environments. *Underwater Technology*, *32*(2), 111–128. doi:10.3723/UT.32.111

Yu, J., Yang, X., Wang, N., Tilstone, G., Fileman, E., Zheng, H., … Zheng, B. (2019). Video-Based Real Time Analysis of Plankton Particle Size Spectrum. *IEEE Access*, *7*, 60020–60025. doi:10.1109/ACCESS.2019.2914727

Zhang, Z. (1999). Flexible camera calibration by viewing a plane from unknown orientations. In *Proceedings of the IEEE International Conference on Computer Vision* (Vol. 1, pp. 666–673). IEEE. doi:10.1109/iccv.1999.791289

Supplementary materials for
In situ size and motility measurement of aquatic invertebrates with an underwater stereoscopic camera system using tilted lenses

Pichaya Lertvilai*, Jules S. Jaffe

Scripps Institution of Oceanography, University of California San Diego, La Jolla, CA 92093

*plertvil@ucsd.edu

Supplementary Tables

Supplementary Table 3.1: Specifications of the underwater stereoscopic imaging system

Parameters	Values	Notes
Instrument weight in air	2.2 kg	Excluding battery pack
Total weight in air	3.3 kg	Including battery pack
Weight in seawater	~0.1 kg buoyant	Including battery pack
Size	380 mm length x 100 mm ø	
Computer	Raspberry Pi 4B (4GB RAM)	
Camera sensor	Sony IMX477 x2	Synchronized by Arducam stereo board
Camera lens	f = 12 mm, f/2, M12 mount	Edmund optics #89-752
Illumination	CREE XQE LEDs x 12	
Field of view	35 mm x 20 mm	
Internal battery	195.36 Wh	11.1V lithium battery Tenergy #31194
Data storage	256 GB	Micro SD card
Power consumption	7.5W during image acquisition 2.9W idling	
Depth rating	100m	Rating from Blueorobotics 4" series housing

Supplementary Figures
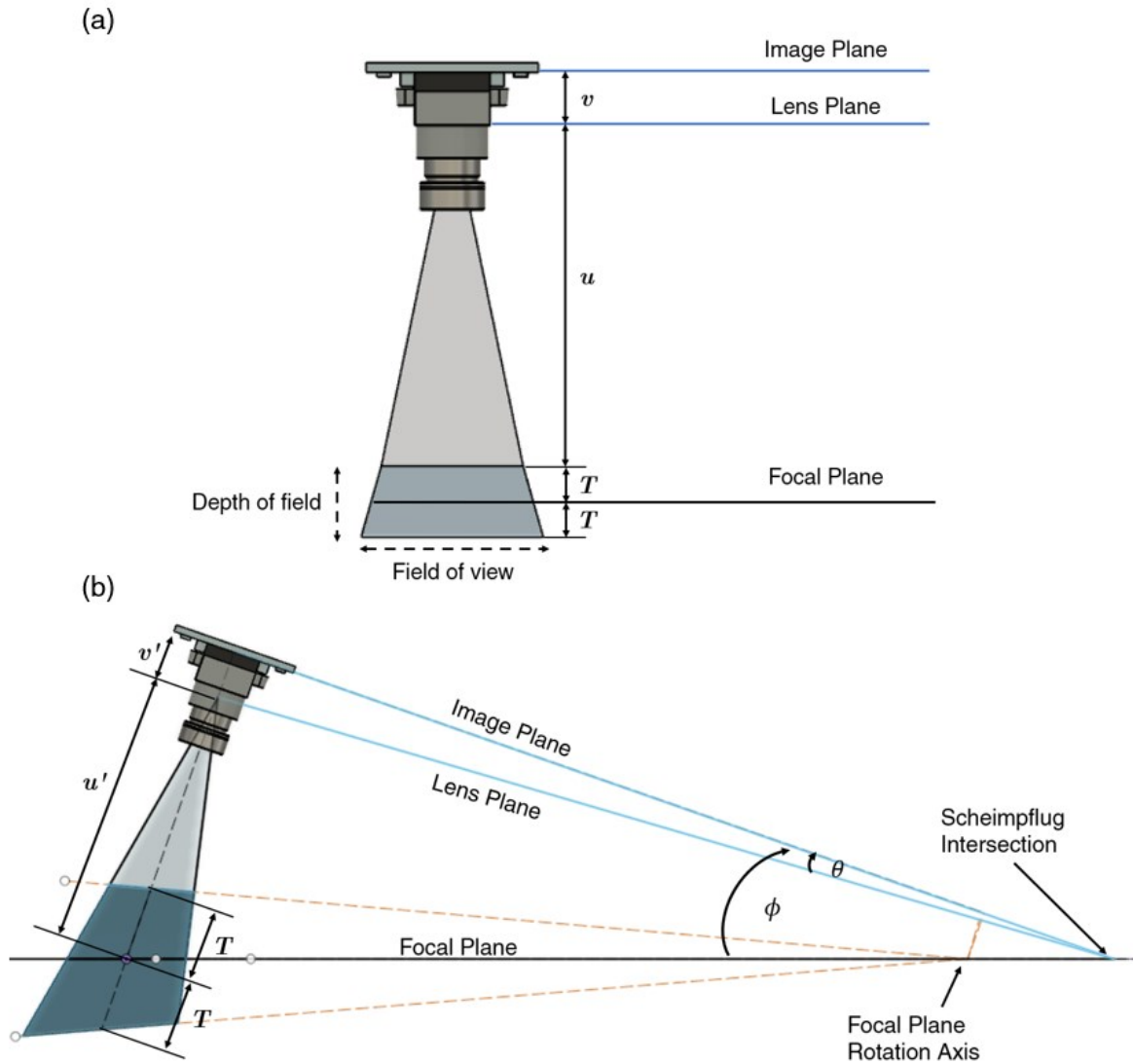
Supplementary Figure 3.1: (a) The geometry of a traditional camera setup with the lens plane parallel to the image plane. u and v are the object distance and the image distance, respectively. T is the depth of field on one side of the focal plane. (b) The geometry of a camera system with a tilted lens. u' and v' are the object distance and the image distance along the line of sight perpendicular to the image plane, respectively. θ is the lens tilt angle with respect to the image sensor, and ϕ is the focal plane tilt angle with respect to the image sensor. The schematics are drawn to scale based on the parameters of the camera used in the actual system.
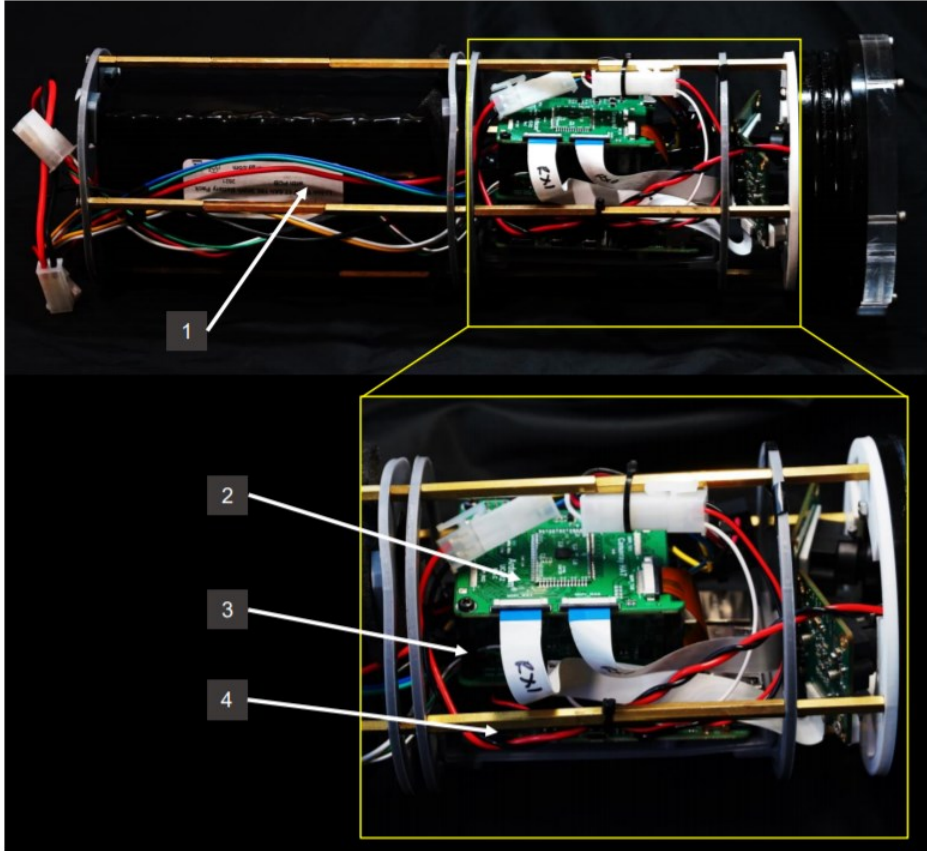
Supplementary Figure 3.2: The internal components of the system. (1) An internal 195Wh lithium-ion battery pack. (2) Arducam synchronized stereo camera board. (3) Control board. (4) Raspberry Pi 4 board.
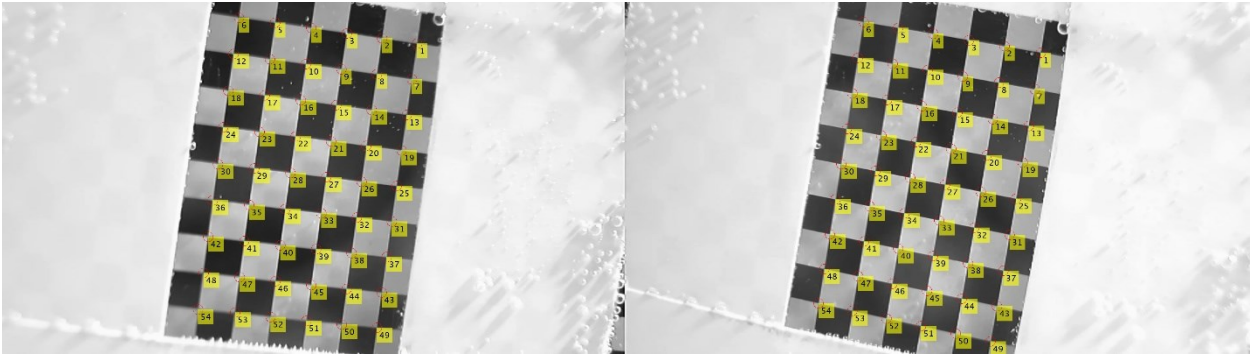
Supplementary Figure 3.3: The checkerboard pattern used to perform stereo calibration for the system. The pattern contains 6 x 9 internal corners, and each square is 2 mm x 2 mm.
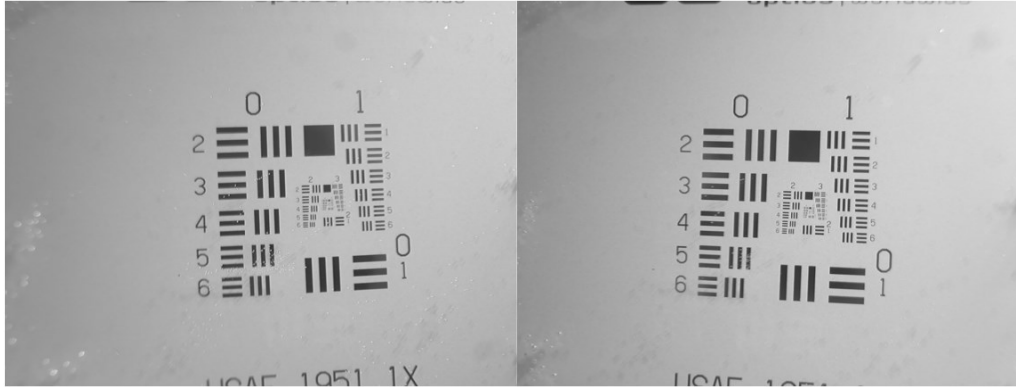
Supplementary Figure 3.4: An example image of a USAF1951 resolution target used to verify the length measurement using the system.

Supplementary Figure 3.5: The field deployment of the system in a water channel at the Kendall-Frost saltmarsh, San Diego, California. The instrument was mounted on an aluminum speed rail structure that lifted the system approximately 0.3 m above the bottom of the channel. The inset shows the converging light from the LEDs that was collimated by the Fresnel lens.
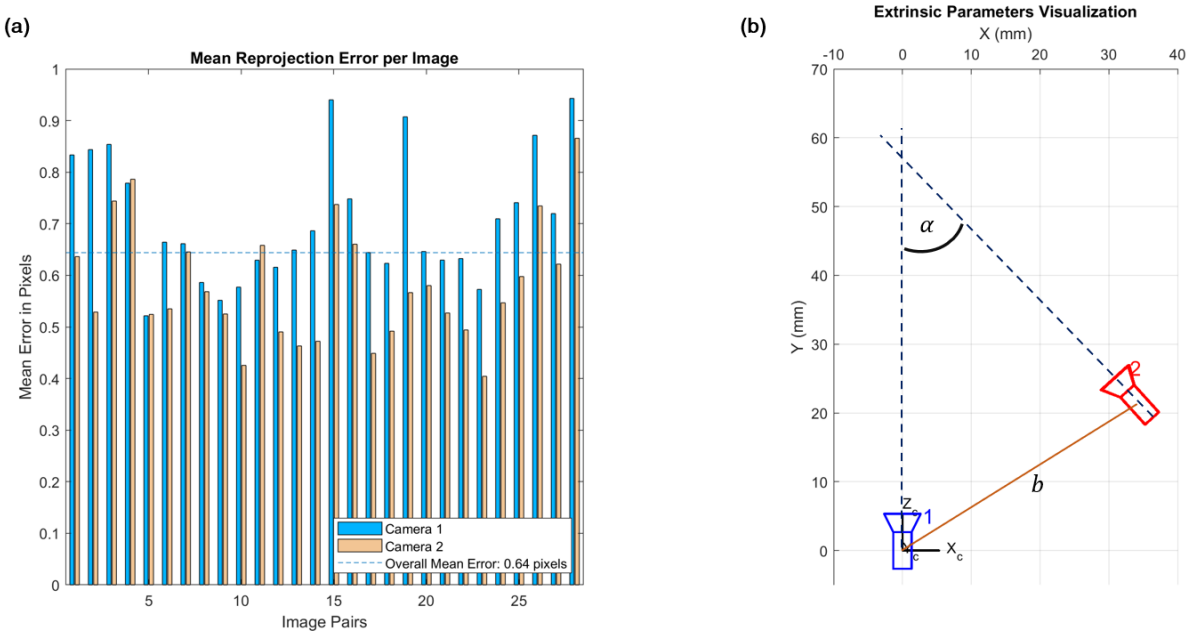
Supplementary Figure 3.6: The result of the stereo calibration. (a) The mean reprojection error of each stereo pair. (b) The visualization of the extrinsic parameters of the two cameras. The blue camera is associated with the left camera of the instrument, the red camera with the right camera. The view angle between the two cameras is $\alpha = 44°$, and the baseline distance is $b = 43.7$ mm.
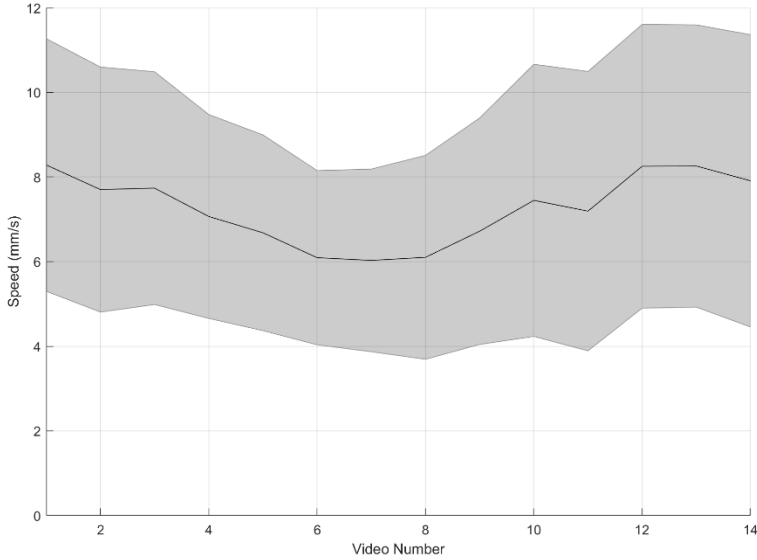
Supplementary Figure 3.7: The mean speed of all tracked particles in each video during the deployment. The solid line indicates that mean value, and the shaded errorbar indicates the standard deviation of the speed of all particles.
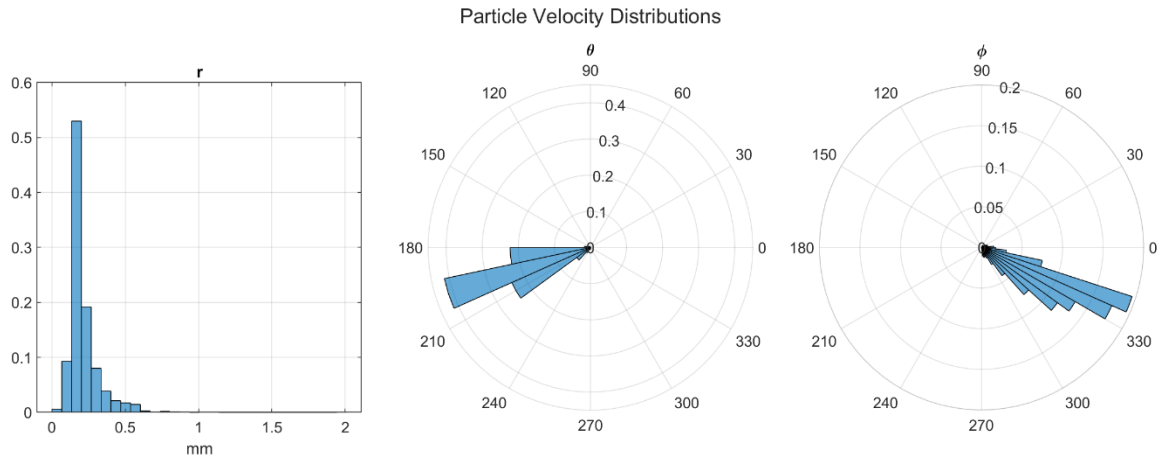
Supplementary Figure 3.8: An example of the probability density distribution of particle velocity from a 60-second video showing that the particles are moving at approximately the same velocity. The probability density distributions shown are in the polar coordinates with r represents the magnitude, θ the polar angle and ϕ the azimuthal angle.

Supplementary Videos

Video S1: The raw footage from the field deployment in Kendall-Frost saltmarsh. The playback speed is in real time.

Video S2: An excerpt of the video S1 showing the tracking algorithm of 20 individual insects that can be tracked for more than 5 consecutive frames. The playback speed is 1/3 of real time.

Supplementary Listings

Pseudo-code for image processing steps to segment organisms from raw images

Note that all programs used in this study are written in MATLAB 2020b. Equivalent OpenCV

functions are given as a reference for users who are interested in using Python instead of

MATLAB. N/A in the Python OpenCV column indicates that there is no direct function in

OpenCV and a custom function has to be written to perform an equivalent step.

STEP	PROCESS	MATLAB FUNCTION	PYTHON OPENCV
1	Load raw RGB image	imread	imread
2	Crop left and right views	imcrop	im[:]
3	Convert to grayscale	rgb2gray	cvtColor
4	Undistort image	undistortImage	undistort
5	Apply Sobel edge detector	Edge	Sobel
6	Morphological dilation	imdilate	dilate
7	Region filling	imfill	N/A
8	Morphological opening	imopen	morphologyEx
9	Blob size filtering	bwareaopen	N/A
10	Final binary mask		

Chapter 4: Label-free underwater single-cell and fluorescence imaging of aquatic microorganisms with laser-pulsed darkfield microscopy

Abstract

Marine microorganisms, including bacteria, protozoans and phytoplankton, constitute more than half of the biomass in the ocean and also play important ecological roles in aquatic ecosystems. However, most marine microbes, including ecologically important bacteria strains, cannot be cultured in laboratory, so the study of their ecology in the laboratory is therefore limited. To facilitate the research of microbial ecology, without depending on laboratory cultivation, there is a need for a system that can observe the microbial processes in the natural underwater environment with minimal disturbance. Here we reported the development of a novel underwater microscope that can perform *in situ* label-free imaging of aquatic microorganisms. The instrument utilizes a laser-pulsed darkfield microscopy technique to image individual cells of marine microorganisms and to detect fluorescence signals from natural pigments without the need for chemical labeling. We demonstrated the performance of the system with both a laboratory validation and an *in situ* observational study on biofilm formation on a man-made substrate. Our work provides a technological platform that helps facilitate future research in aquatic microbiology and to bridge the gaps between laboratory experiments and natural environments.

1.   Introduction

Marine microorganisms, including bacteria, protozoans and phytoplankton, constitute more than half of the biomass in the ocean (Bar-On, Phillips, & Milo, 2018) and also play many important ecological roles, such as substrate conditioning (Bhosle, Garg, Fernandes, & Citon, 2005) and nutrient cycling (Pedler, Aluwihare, & Azam, 2014). However, approximately 99% of marine bacteria are unculturable (Amann, Ludwig, & Schleifer, 1995; Hugenholtz, Goebel, & Pace, 1998), including ecologically important bacteria strains, such as the abundant Woeseiaceae/JTB255 strains (Mu, Ouyang, Chen, & Du, 2021), cannot be cultured in laboratory, so the study of their ecology in the laboratory is naturally limited.

Fortunately, the majority of these marine microbes live in communities that are associated with surfaces (Bar-On et al., 2018). In particular, bacteria often form high-density colonies on surfaces, known as biofilms (McDougald, Rice, Barraud, Steinberg, & Kjelleberg, 2012), which can house various interactions between diverse microorganisms that give rise to complex microbial ecology. These surface-associated communities can be studied with various microscopy techniques, and advances in analytical techniques and imaging technology are enabling scientists to study them in more realistic environments (Wessel, Hmelo, Parsek, & Whiteley, 2013; Dobretsov et al., 2014).

Traditional light microscopy is a relatively inexpensive and simple method to observe living biofilms; however, epifluorescent microscopy is more common because of enhanced contrast and higher specificity from fluorescent staining (Dobretsov et al., 2014). Fluorescence In Situ Hybridization (FISH) is a popular conditioning technique that is often used in conjunction with epifluorescent microscopy to allow phylogenetic identification of microorganisms in environmental samples. FISH is often considered "in situ" for biofilms study as it allows observation of biofilms without the need for cultivation or gene amplification (Dobretsov et al.,

2014). Since the structure of biofilms is often complex and three-dimensional, laser microscopy, mostly used as confocal laser scanning microscopy (CLSM), is a widely used imaging technique that yields 3D reconstruction of the biofilms (Neu & Lawrence, 2016). A multispectral CLSM utilizes multiple laser lines with different wavelength to differentiate between different types of stains and autofluorescence. Yet another method, Magnetic Resonance Imaging (MRI), based on the phenomenon of nuclear magnetic resonance, allows non-invasive measurements of chemical transports in biofilms (Neu et al., 2010). This method has been used to determine the fate of paramagnetic metals (Phoenix & Holmes, 2008) and to track pollutants and biocides in natural biofilms (Graf von der Schulenburg et al., 2008).

Even though these imaging techniques can provide insights into the ecology of live biofilms, all of them require the samples to be taken out of their natural habitat and to be imaged in laboratory setting, often with additional staining with fluorescence labels. Label-free underwater imaging, if available, would provide advantages in resolving uncertainties about whether the lab experiments fully replicate the underwater environment. Several attempts have been made to bridge the gap between the observations in laboratory to the natural environment by creating semi-natural habitats that aim to imitate natural environment in laboratory. A flow cell with ambient water from natural habitat is often used to grow biofilms, which are readily imaged by CLSM without disturbing the interactions inside the flow cell (Matz, Bergfeld, Rice, & Kjelleberg, 2004; Pamp, Sternberg, & Tolker-Nielsen, 2009; Scherwass, Erken, & Arndt, 2016). For more precise topology and complicated microscale features, a microfluidic device can be fabricated to meet experimental requirements and can be utilized the same way as a flow cell (Wessel et al., 2013).

Field studies of biofilms are infrequent and often involve Color-Infrared Imagery (CIR),

which measures reflectance of an area at multiple wavelengths. CIR can be used to determine the amount of chlorophyll-a in biofilms as an index of biomass (Thomason et al., 2014). For example, Murphy et al. (Murphy, Underwood, Tolhurst, & Chapman, 2008) used this technique to investigate the spatial scales of variability in chlorophyll of biofilms on intertidal rocks.

Despite all these advances in biofilm studies over the past few decades, there is currently no available instrument capable of resolving the microscopic interactions in biofilms in their natural underwater habitats. Semi-natural experiments in flow cells or microfluidic devices cannot replicate all intricacies of the natural environment, and field studies are limited to intertidal areas with chlorophyll measurements only. In this study, we developed a novel underwater microscope, the Moore Underwater Microscope (MUM), that is capable of performing label-free imaging of aquatic microorganisms in their natural habitat with minimal disturbance. This article presents the description of the instrument, laboratory validation of its performance and a field study that includes both temporal and spatial observation of development of biofilm on a substrate.

2. Materials and methods
2.1 Instrument description

2.1.1 Overview

The Moore Underwater Microscope (MUM) is an imaging system that provides *in situ* underwater observations of microorganisms at micrometer resolution. The system utilizes a darkfield microscopy technique to achieve the desirable resolution and contrast, which allows tracking of individual cells. The instrument consists of two separate housings: one for the illumination hardware, and the other that encloses an embedded computer, optics and two cameras (Fig. 4.1(a)). Both housings have optically clear acrylic ports and communicate with one

another through a Subconn underwater cable.

The instrument is equipped with an internal computer (Nvidia Jetson TX1), an on-board 2TB solid state drive for data storage and an internal lithium-ion battery. All components are housed inside a waterproof housing that is depth rated for 65m. The internal computer can be programmed to operate autonomously or can be tethered through an ethernet connection to an external controller. When the MUM is operated by a SCUBA diver, it can be controlled by an iPad housed in a waterproof housing (iDive Housing, California) through an underwater Wi-Fi cable (Camdo Solutions, Canada). The iPad can communicate with the internal computer through a remote desktop application, and the diver can then control the MUM using a custom program with a graphical user interface (Fig. 4.2). The software provides a real-time image stream to the diver and allows the diver to adjust necessary camera parameters, such as exposure, and also to manually adjust the focal plane of the imaging system.
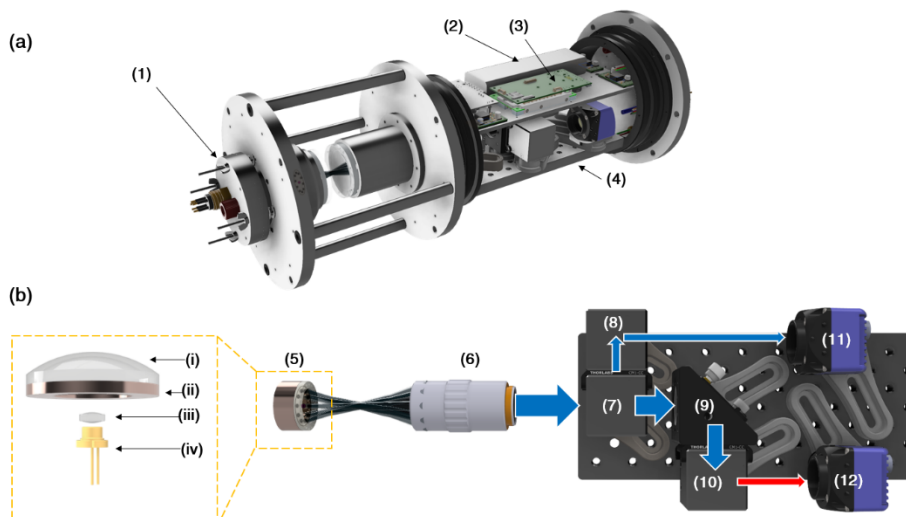
Figure 4.1: (a) The instrument fully assembled inside a waterproof housing. (1) The laser diode assembly. (2) An internal battery. (3) An Nvidea Jetson TX1 single-board computer. (4) Optical components. (b) The optical components and the optical path of the imaging system. (5) The laser diode assembly with the individual components shown in the inset: (i) a plano-convex collimating lens, (ii) a diffuser, (iii) an aspherical lens and (iv) a 450nm laser diode. (6) An objective lens. (7) A 90:10 beam splitter. (8) and (9) 90° mirrors. (10) A 90° mirror with 460nm long-pass filter. (11) the scattered light camera (12) the fluorescence camera.
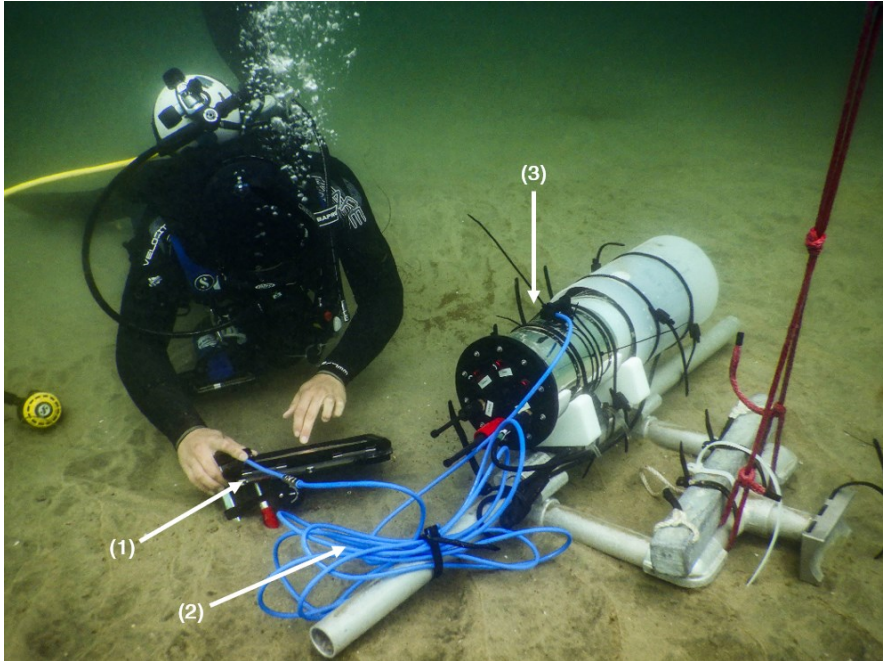
Figure 4.2: The Moore Underwater Microscope (MUM) during an in situ deployment at the seafloor near Scripps Pier, California. (1) An iPad inside a waterproof housing. (2) An underwater Wi-Fi cable. (3) The underwater microscope.

2.1.2 Illumination

A challenge in label-free imaging is to provide sufficient illumination intensity such that the intensity of light scattered from microorganisms can be detected by the imaging system while maintaining high contrast. To overcome this challenge, we implemented a darkfield illumination by using an array of ten 450-nm 1600mW multimode laser diode (Thorlabs #L450P1600MM). Each laser diode is collimated by an aspheric lens (f=2.8 mm, NA=0.6) and the ten diodes are arranged in a circular pattern with a radius of 20 mm. The illumination from each diode passes through a diffuser and is then focused by a plano-convex lens (f=50 mm) to the location of the sampling volume (Fig. 4.1(b)). All laser diodes are driven by a driver circuit (IC Haus #IC-HG) that allows for precise control of pulse width and intensity. For the purposes of this study, the pulse width is set to 50 µs, though the pulse width can be precisely controlled within the range of 10 – 100 µs.

Another challenge in illumination design is to balance the amount of light such that it does not damaging the cells of microorganisms. Intense laser pulse can cause cell damage, which interferes with development of natural processes, including biofilm formation, so the illumination has to be carefully designed to avoid this interference (Kanavillil Nandakumar et al., 2010a, 2010b). The damage threshold of a laser is determined by the laser fluence (F), which is the product of the irradiance (E) and the pulse width (t) (K. Nandakumar, Obika, Utsumi, Ooie, & Yano, 2006),

$$F = Et \tag{1}$$

To achieve this balance, we set the intensity of the laser diode array such that the total irradiance at the focal point is 1.7×10^5 W/m^2. For a laser pulse width of 50µs, this irradiance results in a laser fluence of 8.3×10^{-4}J/cm^2. According to previous studies (Kanavillil Nandakumar et al., 2003, 2010c; K. Nandakumar et al., 2006), the fluence of 5.0×10^{-2}J/cm2 for 30 s results in less than 5% mortality rate of marine bacteria and other marine fouling organisms, such as diatoms and barnacle larvae. As a result, the fluence of the MUM, which more than 100 times less potent than the threshold, is not expected to cause cell damage during our deployment.

2.1.3 Optical System

The MUM is equipped with two monochrome machine vision cameras (Matrix Vision BlueFox 3) that are set to record raw 8-bit images at a resolution of 2500 x 2500 pixels and a frame rate of 30 fps (Fig. 4.1(b)). The two cameras serve different purposes: one camera captures scattered light from all objects in the imaging volume and the other only captures fluorescence signal from pigmented organisms. The 450nm light from the laser diode assembly is scattered by objects in the imaging volume and then passed through a 5X infinity-corrected objective lens (Mitutoyo #378-802-6) and a tube lens. The light is then split by a 90:10 beamsplitter where 10%

of the optical power is passed to the scattered light camera, and 90% is passed through a 460nm long-pass filter into the fluorescence camera (Fig 1(b)). This long pass filter eliminates the stimulating light while preserving all light that is re-emitted, primarily by fluorescence. This ratio of beamsplitting is necessary to both preserve the weaker fluorescent signal while, at the same time, preventing oversaturation of the images of the scattered light camera.

With this optical setup, the imaging system performs darkfield microscopy so that objects in the sampling volume appear bright on a black background. The field of view of each camera is 1.2 mm x 1.2 mm, resulting in a pixel resolution of 0.48 μm/pixel. The expected resolving power according to the illumination wavelength of 450 nm and the numerical aperture of the objective lens of 0.14 is 1.6μm. The depth of field is approximately 10 μm for a feature of 10 μm in size, so the effective sampling volume is 0.014 μL.

2.2 Laboratory Validation

To determine the fluorescence camera response, the camera was used to image a solution of fluorescein. To accomplish this, solutions of fluorescein with concentrations between 1 and 10 μM in filtered seawater were injected into a 400 μm wide microfluidic channel (iBidi μ-Slide Chemotaxis), and the MUM was set to image with pulse widths varying from 10 to 60 μs. The calibration curve of the fluorescence camera was then calculated from the mean pixel intensity of 1000 images from each treatment.

To validate the capability of the MUM to image individual bacterial cell and to image fluorescence signal from natural pigments, we used the system to image a mixture of a bacteria isolate and a phytoplankton culture. The mixture contained a culture of TW7 bacteria (*Vibrio* sp.) with an approximate size of 1.6 μm (Bidle & Azam, 2001) and a culture of *Dunaliella salina* with approximate size 4-8 μm. The mixture was injected into the iBidi μ-Slide VI – Flat, and the

MUM was set to image in the middle of the channel.

In order to process these images, first, the raw image from the scattered light camera was contrast-stretched to enhance contrast and then median-subtracted to remove static background noise. Then, an adaptive thresholding algorithm (Wellner, 1993) was applied to segment individual cells from the remaining background. For the fluorescence camera, a simple global thresholding algorithm was applied to remove background noise and segment individual phytoplankton cell. The images from both cameras were then aligned to form a combined image that distinguish bacterial cells from phytoplankton cells. Additionally, ten in-focus bacterial cells from the scattered light camera and ten in-focus phytoplankton cells from the fluorescence camera were averaged to determine the point spread functions of both types of organisms.

2.3 Field Experiments

2.3.1 Overview

The utility of the MUM for in situ microscopy was demonstrated through an observational study on biofilm formation on a man-made substrate. The field study was conducted in a shallow lagoon on the Coconut Island in the Kaneohe Bay, Hawaii at a depth of approximately 1-2 m. An optically clear glass substrate was placed in the imaging area such that the focal plane of the imaging system lies on a surface of the substrate (Fig. 4.3). The system was submersed for 72 hours and was programmed to image the surface for 60 s every 30 mins. The illumination from the laser diode was only turned on during the imaging to ensure that the laser fluence did not damage microorganisms in the developing microfouling community.
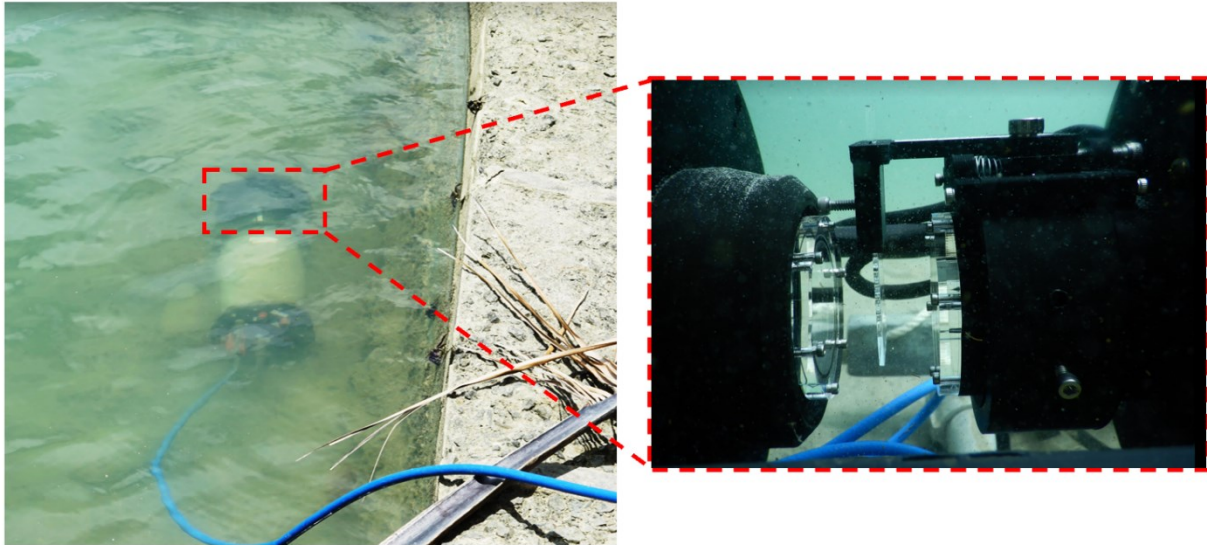
Figure 4.3: The field deployment of the MUM in a shallow lagoon on the Coconut Island in the Kaneohe Bay, Hawaii to perform an observational study on biofilm formation on an optically clear glass substrate. The inset shows the placement of the glass substrate at the focal plane of the imaging system.

2.3.2 Bacterial Motility Analysis

An analysis on the motility of bacterial cells on the glass substrate was performed on an image sequence that was recorded 2.5 hours after the initial submersion. The background subtraction and the adaptive thresholding processing were applied to the raw images from the scattered light camera as described in Section 2.2 to segment individual bacterial cells. A simple global nearest neighbor algorithm (Reid, 1979) was then applied to each detected cell to track it between two consecutive frames. A cell in the current frame was matched with the one in the next frame that was closest to it and not farther than a threshold of 20 pixels (9.6 μm). A track is considered ended when no matching cell can be found for more than 4 consecutive frames. The speed of each cell was then calculated by dividing the distance it traveled between two frames by the period between frames.

2.3.3 Autotroph Colonization Analysis

The images from the fluorescence camera were used to analyze the colonization rate and pattern of autotrophs with detected fluorescing pigments. For each sequence of 60 s recording,

the median image was calculated, and then an adaptive thresholding algorithm was applied to the median image to segment the area in the image with detectable fluorescence signal. The percentage of the image that contains fluorescence signal was calculated to determine the colonization rate over the period of submersion.

Additionally, the colonization pattern of the photosynthetic organisms was analyzed using the pair correlation function (PCF) statistics, which is a noncumulative neighborhood density function (Condit, 2000; Wiegand & Moloney, 2004). The segmented binary images were rasterized into grids with a cell size of 5 x 5 pixels (2.4 μm x 2.4 μm), which was the approximate size of microcolonies on the images. The PCF was then applied to the rasterized image using the grid-based approach (Wiegand & Moloney, 2004). The value of the PCF ($g(r)$) at a distance r is calculated as

$$g(r) = \frac{P(r)}{P_{rand}}, \tag{2}$$

$P(r)$ is the probability of finding an autotroph colony at radius r and is calculated by summing the number of cells on the radius r of a colony that contains another colony and divided by the total number of cells on the radius. P_{rand} is the probability of finding a colony randomly and is calculated by dividing the number of all cells with colony by the total number of cells.

3.   Results
3.1 Response of the fluorescence camera

The response of the fluorescence camera to the fluorescein tracer of concentrations between 1 to 10 μM shows a strong linear response ($R^2 = 0.99$) for the pulse duration of 50 μs, which was used throughout this study (Fig. 4.4(a)). When the pulse duration was also varied between 10 to 60 μs, the overall response of the fluorescence camera (I) shows a linear dependence ($R^2 = 0.99$) on the pulse width (d), the fluorescein concentration (c) and the product

of both parameters in the form (Fig 4(b))

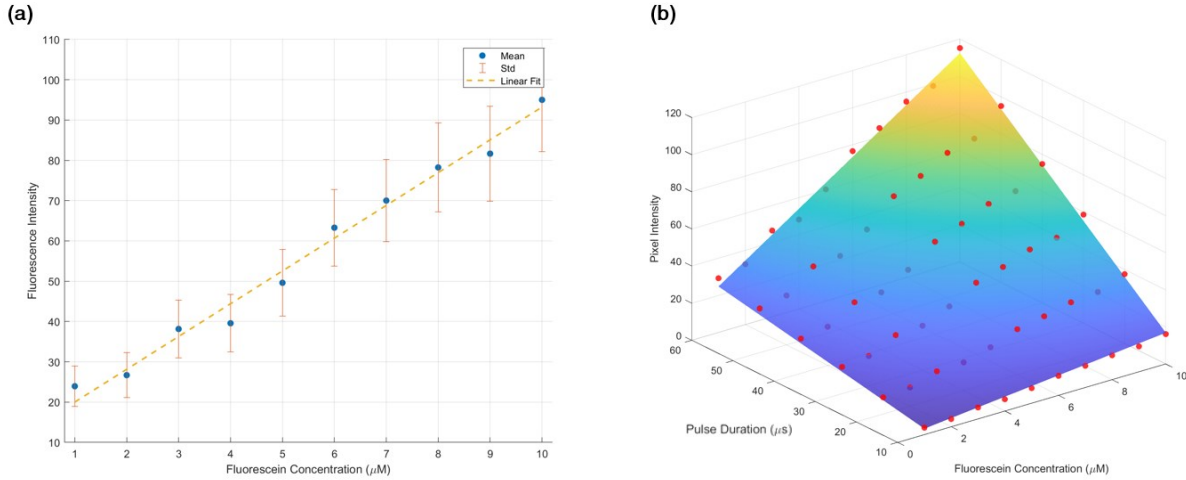$$I(c, d) = -120.1c + 0.3d + 164.5cd - 1.1 \qquad (3)$$

Figure 4.4: The response of the fluorescence camera to the fluorescein tracer. (a) The average intensity of images from the fluorescence camera with varying fluorescein concentrations from 1 to 10 µM and a laser pulse of 50 µs. (b) The average intensity of images from the fluorescence camera when both fluorescein concentrations and laser pulse lengths are varied.

3.2 Single cell imaging

When the MUM was used to image a mixture of TW7 bacteria and *Dunaliella salina* phytoplankton, the raw images from the scattered light camera (Fig 5(a)) provides image quality that is sufficient to distinguish individual bacterial and phytoplankton cells. After the image processing routine is applied, the point spread function of each bacterial cell that span a full width at half maximum (FWHM) of 8 pixels (Figs 4.6(a)-(b)), indicating that the bacterial cell can be clearly seen and easily distinguished from the background (Fig. 4.5(b)).

The fluorescing pigments on *Dunaliella salina* show up well on the fluorescence camera such that individual phytoplankton has a point spread function with a FWHM span of 16 pixels (Figs 4.5(c)-(d)). When the information from both the scatter light camera and the fluorescence camera is combined into a composite image, the phytoplankton cells and the bacterial cells can be differentiated based on the presence of fluorescence pigments (Fig. 4.5(d)).
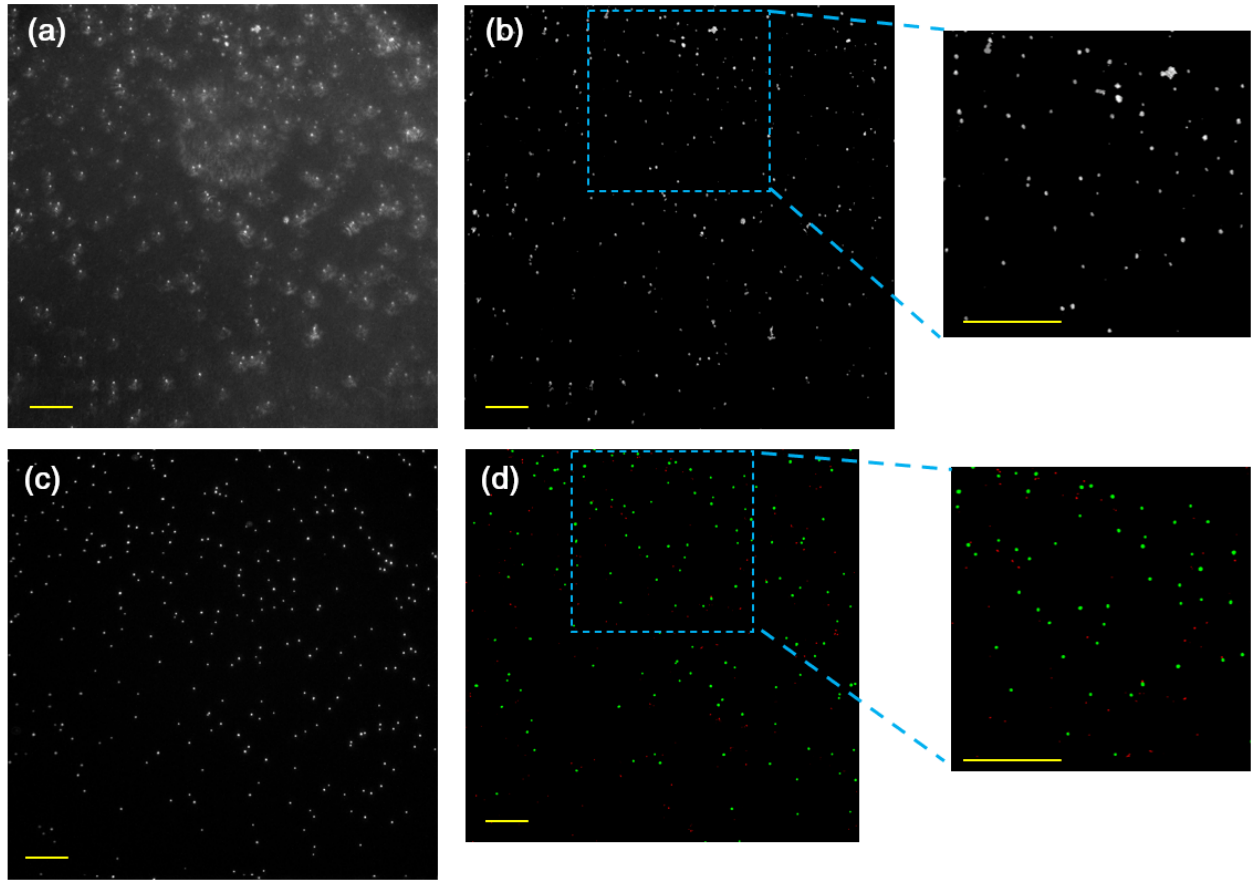
Figure 4.5: Images of a mixture of TW7 bacteria isolate and Dunaliella salina phytoplankton. (a) The raw image from the scattered light camera. (b) The same image after applying an image processing routine to remove background and to improve contrast. (c) The image from the fluorescence camera after applying a contrast enhancement routine. (d) The combination of (a) and (c) allows microorganisms with fluorescent pigments (green) to be distinguished from those without (red). Note that the size of (d) is slightly smaller than (a)-(c) because of the alignment between the two cameras. The scalebars indicate 100μm.
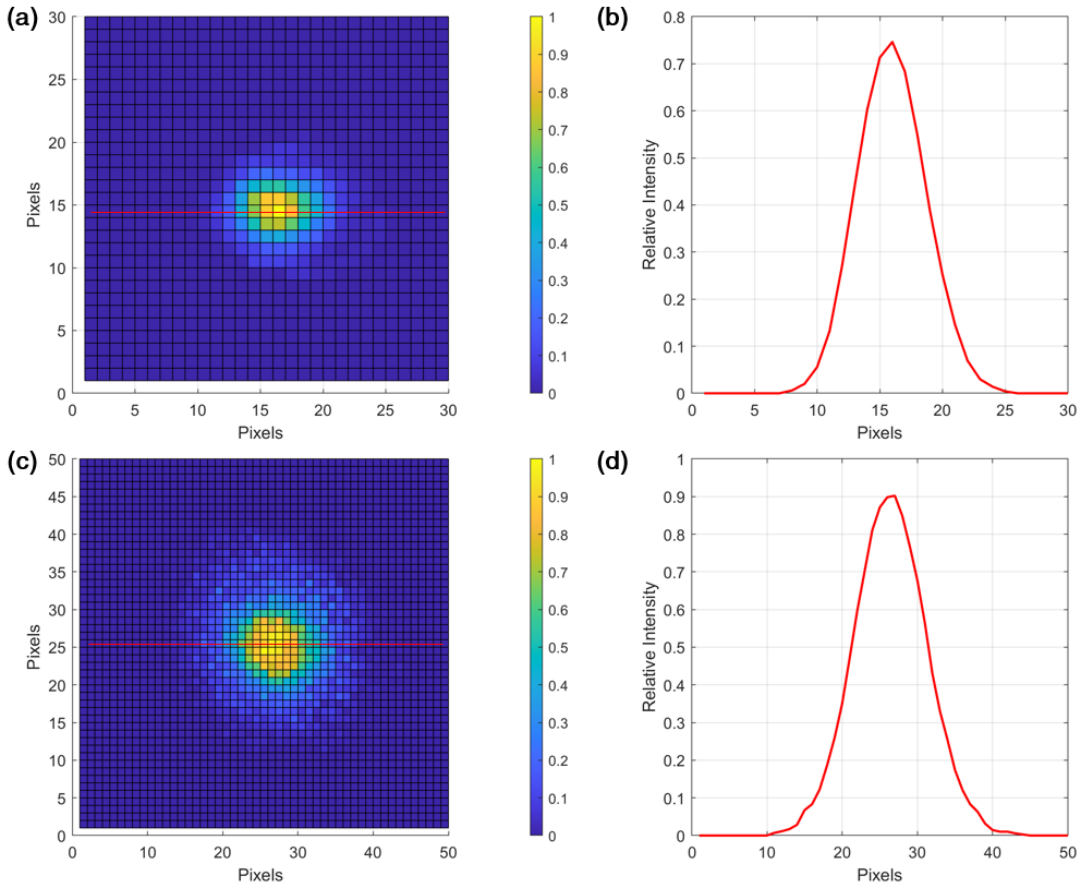
Figure 4.6: (a) The average point spread function of in-focused individual TW7 bacterial cells (*Vibrio* sp.) from the scattered light camera. (b) The corresponding relative intensity of the peak of the point spread function in (a) as denoted by the red line. (c) The average point spread function of in-focused individual *Dunaliella salina* cells from the fluorescence camera. (d) The corresponding relative intensity of the peak of the point spread function in (c) as denoted by the red line.

3.3 Field Experiments

3.3.1 Overview

The field experiment results in a temporal observation of fouling community on an optically clear glass substrate. Various microorganisms, ranging from motile bacteria, pennate diatoms to multicellular organisms, were present on the substrate throughout the 72 hours of submersion (Fig 7). The image sequence also shows different micro-scale processes that happened on the substrate, such as swarming behavior of protozoa (Video S1) and sloughing of microcolonies (Video S2).
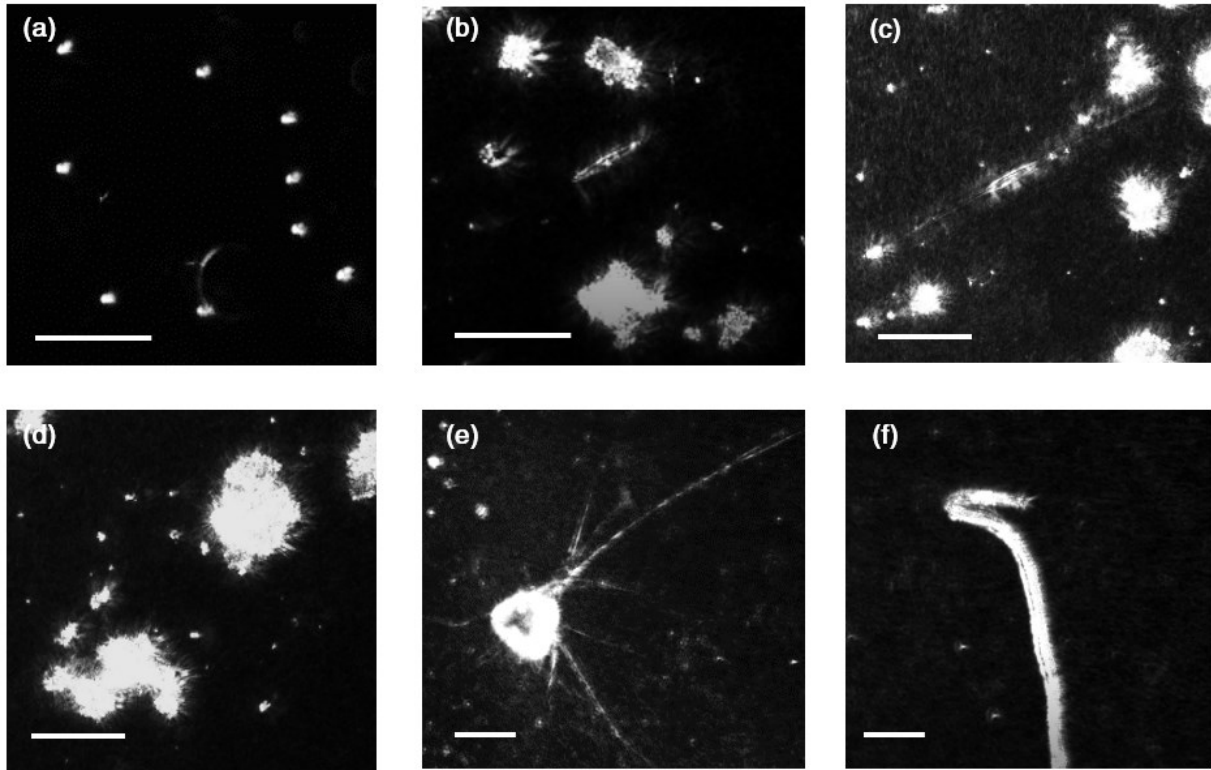
Figure 4.7: Sample images from an in situ deployment of the MUM. (a) A swarm of protozoa. (b)-(c) Pennate diatoms moving among microfouling colonies. (d) Microfouling colonies. (e)-(f) Large multicellular organisms.

3.3.2 Bacterial motility

The images from the field study provide sufficient contrast that is suitable for segmentation of individual cells. The detected motile cells from the image sequence have an average size of 1.5 μm and a density of 694 cells/μL. The global nearest neighbor successfully tracks a total of 40 individual cells with an average track length of 101.7 frames (3.39 seconds). The cells appear to move throughout the imaging volume in a random pattern (Fig. 4.6(a) and Video S3). The median speed of all cells is 125 μm/s, and the maximum instantaneous speed is 301 μm/s (Fig. 4.8(b)).

74
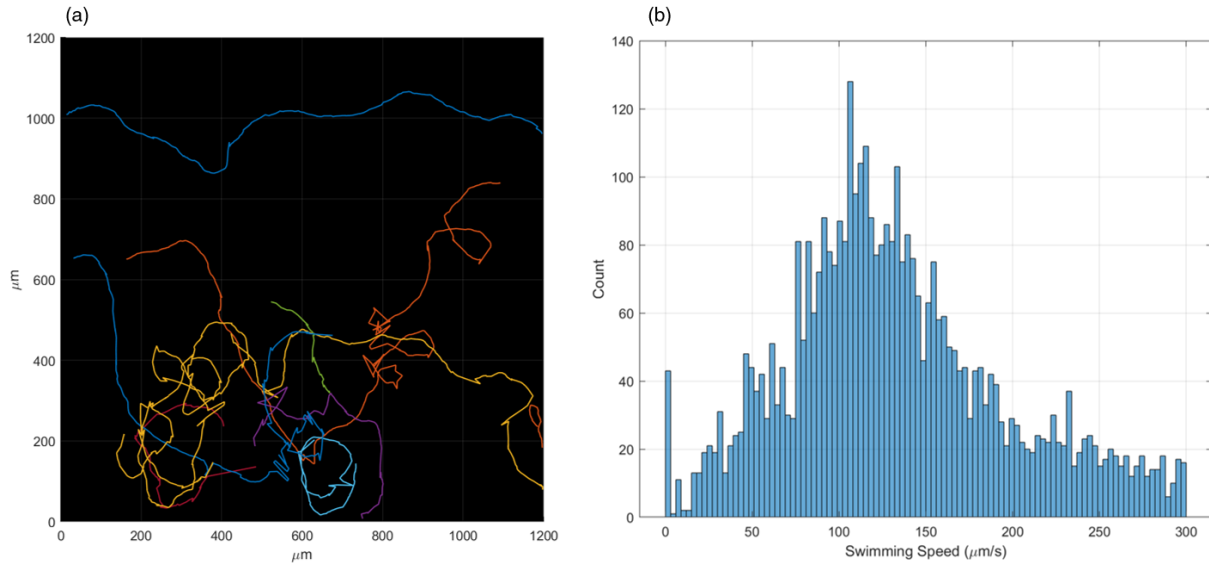
Figure 4.8: (a) A sample of 10 tracks from individual motile bacterial cells moving on a glass slide. (b) The histogram of measured instantaneous speed of bacterial cells.

3.3.3 Autotroph colonization

The images from the fluorescence camera shows an increasing trend of area coverage by autotroph with detectable fluorescing pigments (Fig. 4.9(a)). The increase rate is linear at the rate of 0.9% per day ($R^2 = 0.77$). The percent coverage fluctuates significantly more during daytime compared to nighttime because the presence of motile phytoplankton that did not colonize the substrate and was more active during the daytime.
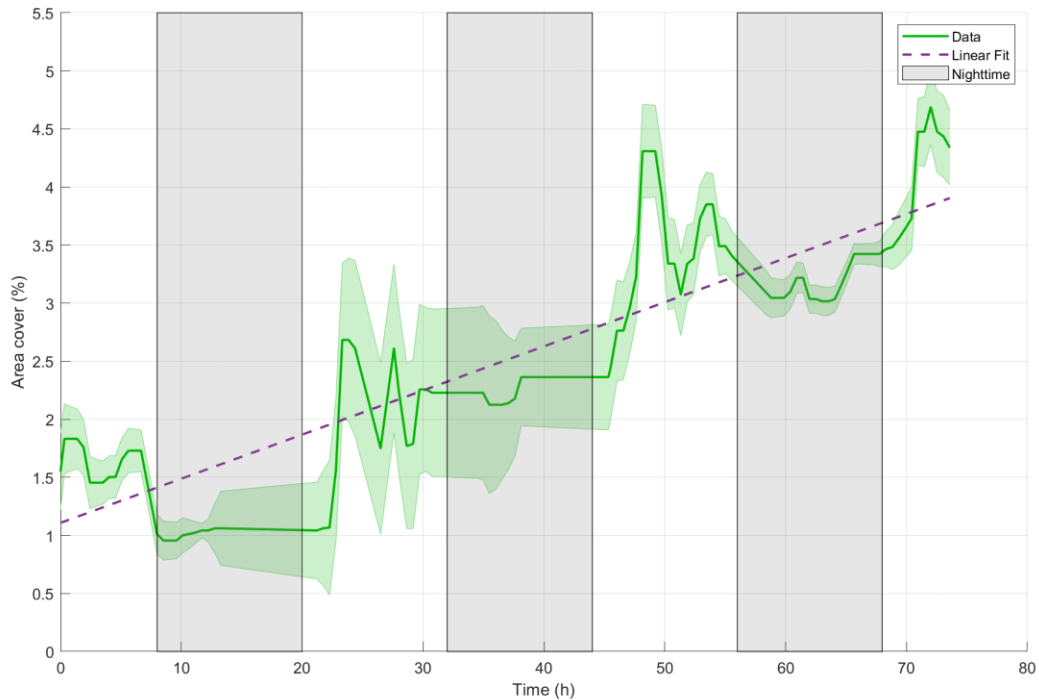
Figure 4.9: The autotroph colonization on a glass slide measured from the percent coverage of the imaging area by pigmented organisms on the fluorescence camera. The solid line shows the mean area coverage for a sequence of 1000 images, and the shaded error bar shows the standard deviation.

The spatial analysis of the colonization pattern shows that the PCF (g(r)) varied throughout the experiment. At 24 hours after the submersion, the PCF shows $g(r) > 1$ at distance $r < 300$ μm, and $g(r) < 1$ at other longer distance (Fig. 4.10(a)). As time progressed, the value of PCF at distance $r > 300$ μm increases and becomes closer to 1 (Fig. 4.10(b)). At the end of the experiment. The value of PCF becomes very close to 1 at all distances beyond 200 μm (Fig. 4.10(c)).
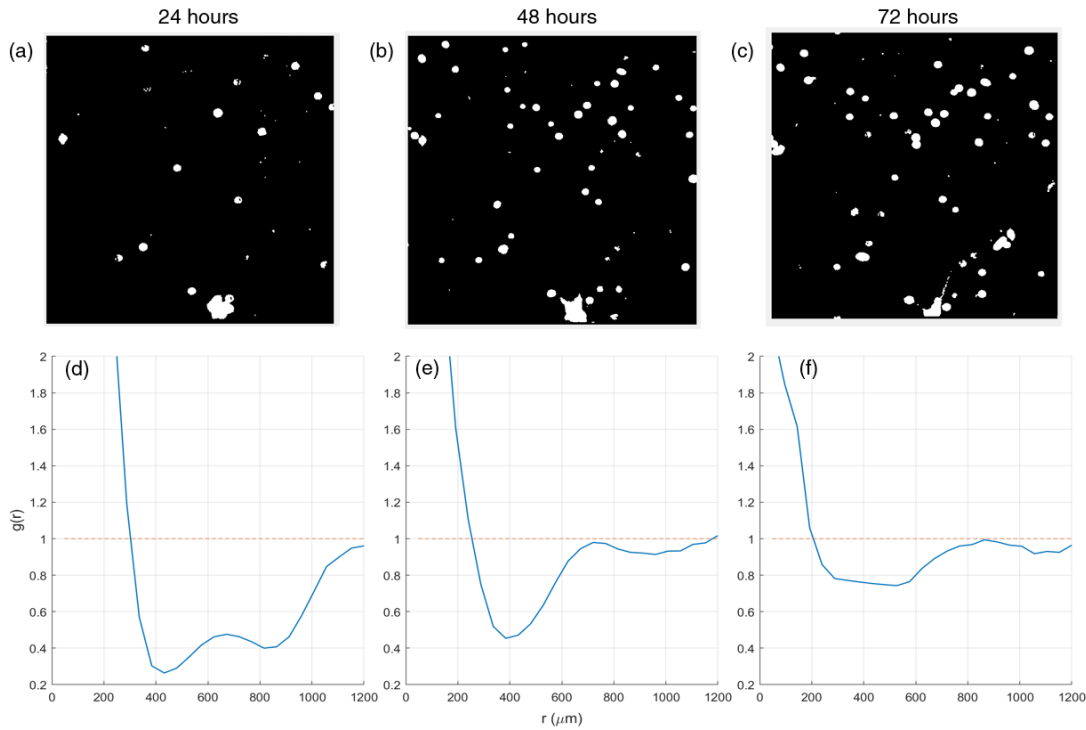
Figure 4.10: (a)-(c) The images from the fluorescence camera of the MUM at the end of each deployment day. (d)-(f) The corresponding pair-correlation-function plots showing the colonization pattern at the end of each day.

4.   Discussion

4.1 Instrument performance

The results from the laboratory experiments indicate that the Moore Underwater Microscope (MUM) is capable of performing label-free single-cell imaging of microorganisms. The array of ten 450nm laser diodes produces high intensity darkfield illumination that is sufficient to illuminate large motile bacterial cell (~1.6 µm in size) with high contrast such that each individual cell can be segmented with image processing algorithms. The intensity of the illumination is also sufficient to produce strong fluorescence signals in natural pigments of microorganisms such that they can be detected by the imaging system. The information from both the scattered light camera and the fluorescence camera allows the MUM to distinguish between types of microorganisms with fluorescing pigments and those without.

Additionally, the fluorescence camera shows a linear response to the concentration of

fluorescence chemical, allowing a direct calculation of fluorescence concentration from images with a calibration curve. As a result, in addition to detecting natural pigments in microorganisms, the fluorescence camera can also be used to track chemical gradients by using fluorescing dyes as a proxy. By combining the images from both cameras, this capability allows the MUM to perform other types of manipulation experiments, such as observation of chemotaxis in gradients of chemoattractant.

4.2 Bacterial motility

The field experiment demonstrates that the MUM can perform *in situ* imaging of microorganisms that allow for tracking of individual cells. We achieved good tracking results with a relatively simple global nearest neighbor because the density of large motile cells was relatively low. The tracking and the subsequent movement speed calculations reveal that the observed large motile bacteria could move at a median speed of 125 µm/s and at a maximum speed of 301 µm/s (Fig. 4.8). This observed speed is much faster than previously reported cultured marine bacteria that could be investigated in the lab where the mean speed was approximately 40 µm/s and the max speed was 80 µm/s (Johansen, Pinhassi, Blackburn, Zweifel, & Hagström, 2002). However, natural bacterial assemblage that could not be cultured could have the mean observed speed could be as high as 230 µm/s with a maximum speed of 400 µm/s (Mitchell, Pearson, Dillon, & Kantalis, 1995), which were relatively close to our observations. This discrepancy in the speed of cultured and natural bacterial assemblage emphasizes the need for *in situ* observations of these microorganisms. Since approximately 99% of bacteria are unculturable (Amann, Ludwig, & Schleifer, 1995; Hugenholtz, Goebel, & Pace, 1998), the MUM can facilitate further research into these unculturable organisms that can only be investigated in the field.

4.3 Autotroph colonization

The data from the fluorescence camera from the field study reveals that the MUM can perform *in situ* observation of fluorescence signals from natural pigments in microorganisms. The trend of autotroph colonization matches the expectation that these photosynthetic microorganisms would reproduce and expand their colonies rapidly during daytime with sunlight, and the growth would become stagnant at night without their energy source (Fig. 4.9). For large phytoplankton, such as diatoms (Fig. 4.7), the MUM can be used to resolve their morphology with the scattered light camera and also locate their fluorescence pigments in the cells with the fluorescence camera.

The spatial analysis on the pattern of colonization reveals the micro-scale dynamic of photosynthetic microorganisms. At 24 hours after submersion, these autotrophs aggregate on the glass substrate in small colonies within the size of approximately 300 µm (Fig. 4.10). However, these colonies avoid one another within the range of 300-1000 µm. As time progresses, this avoidance decreases as the number of colonies increases. At the late stage of biofilm formation, these autotrophs still live in colonies with nearly the same size as at the beginning, but the colonies become randomly distributed ($g(r) \approx 1$) throughout the substrate instead. This observation agrees with previous studies that show a similar pattern of algal colonization on other substrates (Mullen et al., 2016), although more complete studies with replications are needed to confirm this interpretation.

4.4 Instrument potential and limitation

Even though our study has demonstrated that the utility of the MUM, the instrument has some limitations that need to be considered when designing a study with the instrument. We designed the system as a darkfield microscope with a 5x objective in order to achieve relatively

large (1.2 mm x 1.2 mm) field of view and high contrast that is suitable for individual cell tracking. The drawback of this approach is that morphology of small organisms cannot be resolved well (Fig. 4.7), so the main method to distinguish between microorganisms and small particles is based on the motion. The system cannot differentiate between non-motile microorganisms and ambient particles of the similar size. As a result, the MUM is limited to study motile organisms for non-pigmented targets.

Additionally, the light intensity required to illuminate label-free microorganisms is high, so we designed the system with appropriate laser diodes. Even though the laser fluence of the illumination is relatively low compared to the amount required to damage cells (K. Nandakumar et al., 2006), a prolonged continuous exposure to the laser can result in disruption of natural processes. In this study, we only limited a constant exposure to 60 s maximum, which prevents damage from occurring. However, a study that needs a continuous observation will need to be cautioned about the effects of the laser on microorganisms.

Despite these limitations, our results have demonstrated that the MUM can perform *in situ* imaging of microorganisms. The instrument utilizes motility and fluorescence signal to detect living cells, so it can achieve label-free imaging, which is the least invasive for *in situ* studies. The MUM can be used in many applications in aquatic microbiology, such as direct observations of bacterial behaviors and interactions between different types of organisms as shown in our observational study in the field. When used in conjunction with other molecular and genetic techniques, the MUM can facilitate research in unculturable microorganisms that cannot be investigated in the laboratory (Hallam et al., 2006; Groisillier et al., 2010). Additionally, the capability of resolving micron-sized targets in situ can be used to observe particles as well. As a result, the MUM is suitable for determining density and size distribution

of ambient particles and studying flows in microfluidic devices in natural environments using various particle tracking and particle image velocimetry techniques.

Finally, the MUM serves as a platform for further technological development. It can be modified and enhanced in future designs that allow the instrument to facilitate other observations of micro-scale phenomena. For instance, laser diodes with other wavelengths and appropriate optical filters can be added such that the fluorescence camera can detect fluorescing pigments in other wavelengths, which allows the MUM to distinguish between different types of photosynthetic pigments, such as phycocyanin in cyanobacteria from chlorophyll *a* in diatoms (Seppälä et al., 2007; McQuaid, Zamyadi, Prévost, Bird, & Dorner, 2011). Additionally, a linear stage can be added to the system such that the focal plane can be programmatically adjusted. This capability will allow the MUM to scan through different depths and observe 3D structure in complex microbial communities, such as biofilms.

5.   Conclusion

The instrument description and the results reported here highlight the application of a novel underwater microscope that is capable of performing label-free single-cell imaging of microorganisms and detecting fluorescence natural pigments in photosynthetic organisms. Our results demonstrate that the instrument can be used to track individual bacterial cells and observe spatial and temporal pattern of autotroph colonization on a microfouling community *in situ*. This work provides a technological platform that helps facilitate future research in aquatic microbiology and helps bridge the gaps between laboratory experiments and the natural environments.

Chapter 4, in part, is currently being prepared for submission for publication of the material. Lertvilai, Pichaya; Jaffe, Jules. The dissertation author was the primary investigator and author of this paper.

Reference

Amann, R. I., Ludwig, W., & Schleifer, K. H. (1995). Phylogenetic identification and in situ detection of individual microbial cells without cultivation. *Microbiological Reviews*, *59*(1), 143–169. doi:10.1128/MR.59.1.143-169.1995

Bar-On, Y. M., Phillips, R., & Milo, R. (2018). The biomass distribution on Earth. *Proceedings of the National Academy of Sciences of the United States of America*, *115*(25), 6506–6511. doi:10.1073/pnas.1711842115

Bhosle, N. B., Garg, A., Fernandes, L., & Citon, P. (2005). Dynamics of amino acids in the conditioning film developed on glass panels immersed in the surface seawaters of Dona Paula Bay. *Biofouling*, *21*(2), 99–107. doi:10.1080/08927010500097821

Bidle, K. D., & Azam, F. (2001). Bacterial control of silicon regeneration from diatom detritus: Significance of bacterial ectohydrolases and species identity. *Limnology and Oceanography*, *46*(7), 1606–1623. doi:10.4319/lo.2001.46.7.1606

Condit, R. (2000). Spatial patterns in the distribution of tropical tree species. *Science*, *288*(5470), 1414–1418. doi:10.1126/SCIENCE.288.5470.1414/SUPPL_FILE/1048222S2.PDF

Dobretsov, S., Abed, R. M. M., Sharp, K., Skalli, O., Boykins, L. G., & Coons, L. (2014). Microscopy of biofilms. In *Biofouling Methods* (pp. 1–43). Oxford, UK: John Wiley & Sons, Ltd. doi:10.1002/9781118336144.ch1

Graf von der Schulenburg, D. A., Holland, D. J., Paterson-Beedle, M., Macaskie, L. E., Gladden, L. F., & Johns, M. L. (2008). Spatially resolved quantification of metal ion concentration in a biofilm-mediated ion exchanger. *Biotechnology and Bioengineering*, *99*(4), 821–829. doi:10.1002/bit.21647

Groisillier, A., Hervé, C., Jeudy, A., Rebuffet, E., Pluchon, P. F., Chevolot, Y., … Czjzek, M. (2010). MARINE-EXPRESS: Taking advantage of high throughput cloning and expression strategies for the post-genomic analysis of marine organisms. *Microbial Cell Factories*, *9*(1), 1–11. doi:10.1186/1475-2859-9-45/TABLES/3

Hallam, S. J., Konstantinidis, K. T., Putnam, N., Schleper, C., Watanabe, Y. I., Sugahara, J., … DeLong, E. F. (2006). Genomic analysis of the uncultivated marine crenarchaeote Cenarchaeum symbiosum. *Proceedings of the National Academy of Sciences*, *103*(48), 18296–18301. doi:10.1073/PNAS.0608549103

Hugenholtz, P., Goebel, B. M., & Pace, N. R. (1998). Impact of culture-independent studies on the emerging phylogenetic view of bacterial diversity. *Journal of Bacteriology*, *180*(18), 4765–4774. doi:10.1128/JB.180.18.4765-4774.1998/ASSET/9AFBA691-C57B-49EF-8FFC-B6DB6BD67E3B/ASSETS/GRAPHIC/JB1880493006.JPEG

Johansen, J., Pinhassi, J., Blackburn, N., Zweifel, U., & Hagström, Å. (2002). Variability in motility characteristics among marine bacteria. *Aquatic Microbial Ecology*, *28*(3), 229–237. doi:10.3354/ame028229

Matz, C., Bergfeld, T., Rice, S. A., & Kjelleberg, S. (2004). Microcolonies, quorum sensing and cytotoxicity determine the survival of Pseudomonas aeruginosa biofilms exposed to protozoan grazing. *Environmental Microbiology*, *6*(3), 218–226. doi:10.1111/j.1462-2920.2004.00556.x

McDougald, D., Rice, S. A., Barraud, N., Steinberg, P. D., & Kjelleberg, S. (2012). Should we stay or should we go: mechanisms and ecological consequences for biofilm dispersal. *Nature Reviews Microbiology*, *10*(1), 39–50. doi:10.1038/nrmicro2695

McQuaid, N., Zamyadi, A., Prévost, M., Bird, D. F., & Dorner, S. (2011). Use of in vivo phycocyanin fluorescence to monitor potential microcystin-producing cyanobacterial biovolume in a drinking water source. *Journal of Environmental Monitoring*, *13*(2), 455–463. doi:10.1039/C0EM00163E

Mitchell, J. G., Pearson, L., Dillon, S., & Kantalis, K. (1995). Natural assemblages of marine bacteria exhibiting high-speed motility and large accelerations. *Applied and Environmental Microbiology*, *61*(12), 4436–4440. doi:10.1128/aem.61.12.4436-4440.1995

Mu, D. S., Ouyang, Y., Chen, G. J., & Du, Z. J. (2021). Strategies for culturing active/dormant marine microbes. *Marine Life Science and Technology*, *3*(2), 121–131. doi:10.1007/S42995-020-00053-Z/TABLES/2

Mullen, A. D., Treibitz, T., Roberts, P. L. D., Kelly, E. L. A., Horwitz, R., Smith, J. E., & Jaffe, J. S. (2016). Underwater microscopy for in situ studies of benthic ecosystems. *Nature Communications*, *7*(1), 12093. doi:10.1038/ncomms12093

Murphy, R. J., Underwood, A. J., Tolhurst, T. J., & Chapman, M. G. (2008). Field-based remote-sensing for experimental intertidal ecology: Case studies using hyperspatial and hyperspectral data for New South Wales (Australia). *Remote Sensing of Environment*, *112*(8), 3353–3365. doi:10.1016/J.RSE.2007.09.016

Nandakumar, K., Obika, H., Utsumi, A., Ooie, T., & Yano, T. (2006). Molecular level damages of low power pulsed laser radiation in a marine bacterium Pseudoalteromonas carrageenovora. *Letters in Applied Microbiology*, *42*(5), 521–526. doi:10.1111/J.1472-765X.2006.01897.X

Nandakumar, Kanavillil, Obika, H., Shinozaki, T., Ooie, T., Utsumi, A., & Yano, T. (2003). Pulsed laser irradiation impact on two marine diatoms Skeletonema costatum and Chaetoceros gracilis. *Water Research*, *37*(10), 2311–2316. doi:10.1016/S0043-

1354(03)00007-1

Nandakumar, Kanavillil, Obika, H., Shinozaki, T., Ooie, T., Utsumi, A., & Yano, T. (2010a). Impact of Pulsed Nd:YAG Laser Irradiation on the Growth and Mortality of the Biofilm Forming Marine Bacterium Pseudoalteromonas carrageenovora. *Http://Dx.Doi.Org/10.1080/08927010290032377*, *18*(2), 123–127. doi:10.1080/08927010290032377

Nandakumar, Kanavillil, Obika, H., Shinozaki, T., Ooie, T., Utsumi, A., & Yano, T. (2010b). Laser Impact on Bacterial ATP: Insights into the Mechanism of Laser-Bacteria Interactions. *Http://Dx.Doi.Org/10.1080/0892701021000028488*, *19*(2), 109–114. doi:10.1080/0892701021000028488

Nandakumar, Kanavillil, Obika, H., Shinozaki, T., Ooie, T., Utsumi, A., & Yano, T. (2010c). Lethal and sub-lethal impacts of pulsed laser irradiations on the larvae of the fouling barnacle Balanus amphitrite. *Http://Dx.Doi.Org/10.1080/08927014.2003.10382979*, *19*(3), 169–176. doi:10.1080/08927014.2003.10382979

Neu, T. R., & Lawrence, J. R. (2016). Laser Microscopy for the Study of Biofilms: Issues and Options. In *Aquatic Biofilms: Ecology, Water Quality and Wastewater Treatment* (pp. 29–46). Caister Academic Press. doi:10.21775/9781910190173.02

Neu, T. R., Manz, B., Volke, F., Dynes, J. J., Hitchcock, A. P., & Lawrence, J. R. (2010). Advanced imaging techniques for assessment of structure, composition and function in biofilm systems. *FEMS Microbiology Ecology*, *72*(1), 1–21. doi:10.1111/j.1574-6941.2010.00837.x

Pamp, S. J., Sternberg, C., & Tolker-Nielsen, T. (2009). Insight into the microbial multicellular lifestyle via flow-cell technology and confocal microscopy. *Cytometry Part A*, *75A*(2), 90–103. doi:10.1002/cyto.a.20685

Pedler, B. E., Aluwihare, L. I., & Azam, F. (2014). Single bacterial strain capable of significant contribution to carbon cycling in the surface ocean. *Proceedings of the National Academy of Sciences of the United States of America*, *111*(20), 7202–7. doi:10.1073/pnas.1401887111

Phoenix, V. R., & Holmes, W. M. (2008). Magnetic resonance imaging of structure, diffusivity, and copper immobilization in a phototrophic biofilm. *Applied and Environmental Microbiology*, *74*(15), 4934–43. doi:10.1128/AEM.02783-07

Reid, D. B. (1979). An Algorithm for Tracking Multiple Targets. *IEEE Transactions on Automatic Control*, *24*(6), 843–854. doi:10.1109/TAC.1979.1102177

Scherwass, A., Erken, M., & Arndt, H. (2016). Grazing Effects of Ciliates on Microcolony Formation in Bacterial Biofilms. In *Microbial Biofilms - Importance and Applications*. InTech. doi:10.5772/63516

Seppälä, J., Ylöstalo, P., Kaitala, S., Hällfors, S., Raateoja, M., & Maunula, P. (2007). Ship-of-opportunity based phycocyanin fluorescence monitoring of the filamentous cyanobacteria

bloom dynamics in the Baltic Sea. *Estuarine, Coastal and Shelf Science*, *73*(3–4), 489–500. doi:10.1016/J.ECSS.2007.02.015

Thomason, J. C., Forsberg, R. L., Meyer, A. E., Baier, R. E., Kellogg, C. A., & Murphy, R. J. (2014). Sampling and experiments with biofilms in the environment. In *Biofouling Methods* (pp. 168–203). Oxford, UK: John Wiley & Sons, Ltd. doi:10.1002/9781118336144.ch6

Wellner, P. D. (1993). Adaptive Thresholding for the DigitalDesk :read, seems not very efficient, *9*. Retrieved from http://citeseerx.ist.psu.edu/viewdoc/summary?doi=10.1.1.70.8856

Wessel, A. K., Hmelo, L., Parsek, M. R., & Whiteley, M. (2013). Going local: technologies for exploring bacterial microenvironments. *Nature Reviews Microbiology*, *11*(5), 337–348. doi:10.1038/nrmicro3010

Wiegand, T., & Moloney, K. A. (2004, February 1). Rings, circles, and null-models for point pattern analysis in ecology. *Oikos*. John Wiley & Sons, Ltd. doi:10.1111/j.0030-1299.2004.12497.x